A DENSITY FUNCTIONAL THEORY STUDY OF COPPER OXIDES NANOWIRES AND CLUSTERS ON ANATASE TiO_2 (101) SURFACE FOR PHOTOCATALYTIC WATER SPLITTING

BY

MENG'WA KIRUI VICTOR

THESIS SUBMITTED IN PARTIAL FULFILMENT OF THE REQUIREMENTS FOR THE DEGREE OF DOCTOR OF PHILOSOPHY IN PHYSICS OF UNIVERSITY OF ELDORET, KENYA

NOVEMBER, 2018

DECLARATION

This thesis is my own original work and has not been presented for degree to any other University. No part of this thesis may be reproduced without prior permission of the author and/or University of Eldoret.

Meng'wa K. Victor

Signature: ..... Date: .....

SC/PHD/007/16

Approval by Supervisors

This thesis has been submitted for examination with our approval as University of Eldoret supervisors.

Dr. Nicholas Makau,

Department of Physics, University of Eldoret, Eldoret, Kenya.

Signature: ..... Date: .....

Professor George Amolo,

Department of Physics, The Technical University of Kenya, Nairobi, Kenya.

Signature: ..... Date: .....

DEDICATION

It is my pleasure to dedicate this work to mum (R. Meng'wa), dad (W. Meng'wa), wife (M. Chesoy) and children (Cheruto, Chebet, Kibet, Siena) for their moral support that enabled me fulfil this dream.

ABSTRACT

Copper oxides deposited at titania surfaces have a beneficial effect on the photocatalytic activity of TiO_2, particularly water splitting. However, the role of copper oxides and mechanisms of enhancement remains to be elucidated. In this work, possible nanostructures of copper oxide on $TiO_2(101)$ surface have been investigated by simulations based on density functional theory. Various stoichiometries, from Cu_2O to CuO, and morphologies, from clusters to nanowires, have been considered. Nanowire structures were found to be consistently more stable than isolated clusters. In these structures, a Cu_2O stoichiometry was found to be thermodynamically more stable than CuO at room temperature conditions, in contrast to what happens in bulk copper. Occupied Cu 3d and O 2p states were found to extend well into the band gap of titania, whereas the nature of the lowest-lying empty states depended on the stoichiometry: for Cu_2O they consist mostly of Ti 3d orbitals, while in CuO unoccupied Cu 3d orbital at $\sim$0.8 eV above the Fermi level are present. Thus, both oxides reduce the band gap of the system with respect to pure titania, but only Cu_2O is effective in separating photogenerated electrons and holes. This work also investigated oxidation of water on the most stable nanostructured Cu_2O/TiO_2 and CuO/TiO_2 systems by density functional theory. Under photoelectrochemical conditions, the most stable structure has a CuO stoichiometry, and yields an overpotential of 0.66 V for water oxidation, with the active site being at the interface between copper oxide and titanium dioxide. A lower overpotential of 0.48 V is found on a metastable Cu_2O nanostructure. These values are lower than the values for pure titania (1.39 V) and for copper oxides (0.77 V and 0.96 V). Moreover, in the case of the most stable structure, the active site is directly at the interface between CuO and TiO_2. We therefore argue that a cooperative catalytic effect between cupric oxide and titania is at play in this system, beside the known increased photoabsorption coming from the reduced band gap. The nanostructures display a stronger adsorption of OH with respect to pristine titania, which is essential in lowering the overpotential, and switching the overpotential-determining step from hydroxyl formation to dehydrogenation of the adsorbed hydroxyl. These results provide insight into the role of copper oxides in the photocatalytic process. Moreover, the insight into the water oxidation reaction provides some guiding principles for the design of improved photocatalysts for solar water splitting.

TABLE OF CONTENTS

LIST OF FIGURES

LIST OF TABLES

LIST OF SYMBOLS AND ABBREVIATIONS OF ACRONYMS

The following are the symbols and acronyms used in this thesis.

a and c	Lattice constants
$\mathring{A}$	Angstrom unit
ψ	Many electron wave function
$\langle \hat{T} \rangle$	Electron expectation value of kinetic energy operator
σ	spin operator
ε_i^σ	eigen values
CB	Conduction band
CBM	Conduction Band Minimum
DOS	Density of states
DFT	Density Functional Theory
eV	electron volt unit
$\mathrm{E}_{Hartree}$	Classical Coulomb Interaction Energy
E_{XC}	Exchange and Correlation Energy
E_{11}	Potential nuclei-nuclear interactions
ET	Electron transfer
E_{xc}	Exchange and correlation energy of interacting system
F[n(r)]	Functional of density
FPMD	first principle molecular dynamics
GGA	Generalized gradient approximation

HER	hydrogen evolution reaction
HOMO	Highest Occupied Molecular Orbitals
H^{σ}_{KS}	Kohn-Sham effective Hamiltonian
$\hat{H}$	Hamiltonian operator
ICTP	International Centre for Theoretical Physics
K	Kelvin
LUMO	Lowest Unoccupied Molecular Orbitals
LDA	Local density approximation
LDA+U	Local density approximation with Hubbard term
NW	Nanowire
NPs	Nanoparticles
nc	nano crystalline
nm	nanometre
OFID	Opec Fund for International Development
PCET	Proton coupled electron transfer
PEC	Photoelectrochemical
PC	Photocatalytic
PBE	Perdew Burke Ernzerhof
PW	Plane Wave
PDOS	Projected Density of States
PWSCF	Plane Wave Self Consistent Field
PAW	Project Augumented Wave

Q.E	Quantum ESPRESSO
OER	oxygen evolution reaction
RHE	Reversible Hydrogen Electrode
STM	Scanning Tunnelling Microscopy
TMRC	Time-resolved microwave conductivity
TDDFT	Time Dependent Density Functional Theory
T_s	Independent particle kinetic energy
TCO's	Transparent conducting oxides
UHV	Ultra High vacuum
V_{ext}	External potential
VBM	Valence Band Maximum
V_O	Oxygen vacancy
V_{eff}^{σ}	effective potential
$V_{eff}(r)$	external potential
X_{4C}	four-fold-coordinated
X_{5C}	five-fold-coordinated
X_{6C}	six-fold-coordinated

ACKNOWLEDGMENTS

First, I thank the almighty God for having brought me this far. I express my deepest gratitude to my University of Eldoret and the International Centre for Theoretical Physics (ICTP), Trieste supervisors; Dr. Nicholas Makau, Prof. George Amolo, Dr. Nicola Seriani and Prof. Sandro Scandolo for valuable guidance and discussions throughout this work.

I am highly indebted to CHPC (Centre for High Perfomance Computing) in South Africa and the ICTP argo cluster for provision of computational resources.

I wish to acknowledge the financial support from Opec Fund for International Development (OFID) for the OFID/ICTP Postgraduate Fellowship Programme provided under Sandwich Training Educational Programme (STEP). This partnership greatly contributed to the success of this work. It offered opportunities to attend seminars at Condensed Matter and Statistical Physics (CMSP) section, workshops, schools and other ICTP scientific activities. I benefited from interaction and collaboration with ICTP scientists and other members of CMSP section.

I thank National Research Fund (NRF)-Kenya for the post graduate research grant that facilitated acquisition of research materials and activities.

The University of Eldoret Computational Materials Science Group introduced me to computational research techniques, in particular Dr. K. K. Korir, for useful discussions in modelling metal oxide surfaces. This ignited by interest in surface science.

I thank Prof. Paolo Giannozzi and co-developers for the open source Quantum Espresso suite for quantum simulation of materials.

I thank Alupe University College for the study leave with pay despite my recent employment. In particular Drs. Korir and Magero, who performed my duties, while on leave.

Lastly, moral support and encouragement provided by the family unit, generated confidence and inspiration to forge ahead, to mention them: Monica Chesoy (wife), Cheruto, Chebet, Kibet and Siena (Children), Rose Meng'wa (mum), Meng'wa Wandiema (dad) and siblings (Chepkwemoi, Chemtai, Ngeywo and Kawon).

CHAPTER ONE

INTRODUCTION

1.1 Titanium dioxide (TiO_2)

TiO_2 exists in the rutile, anatase and brookite crystal phases (Diebold, 2003) . Out of the three natural phases of TiO_2, rutile and anatase are the most widely used phases. Rutile is the thermodynamically most stable bulk phase, while anatase is very common and stable in nanomaterials (Banfield et al., 1998). Besides being stable in nanoparticles, the anatase phase shows also the highest photocatalytic activity, (Kavan et al., 1996) making it the most interesting phase for use in photocatalytic and photovoltaic devices. A key role in these applications is played by the electronic properties. For instance, the positions of the conduction and valence band edges relative to the potentials of relevant reduction-oxidation reaction determine whether a photocatalytic reaction can occur or not; the band gap determines the optical absorption, which has an essential role in the performance of photocatalytic devices while the states near the valence and conduction band edges have a major influence on the electrical conductivity and chemical reactivity (De Angelis et al., 2014). This study is centred on anatase phase of TiO_2 and specifically its (101) surface plane.

Anatase has a tetragonal lattice (D_{4h}^{19}-$I4_1/amd$, a=b=3.782 Å, c= 9.502 Å) with four TiO_2 units per unit cell forming chains of slightly elongated TiO_6 octahedra (Diebold, 2003). The unit cell is shown in Fig. 1.1 and the basic building block consists of a titanium atom surrounded by six oxygen atoms in a more or less distorted octahedral configuration.

In the structure, the two bonds between the titanium and the oxygen atoms at the apices of the octahedron are slightly longer. The corner-sharing octahedron forms (001) planes, that are connected with their edges to the plane of the adjacent octahedron located below it. The stacking of the octahedra results in threefold coordinated oxygen atoms (O_{3C}). The Ti−O bonding is largely ionic with some covalent contribution (Asahi et al., 2000). The fundamental band gap in anatase is indirect, with the bottom of the conduction band (CB) at Γ and the top of the valence band (VB) close to the X point, along the Δ (or Γ-X) direction. The experimental band gap of bulk anatase is 3.2 eV, while the optical band gap has a value

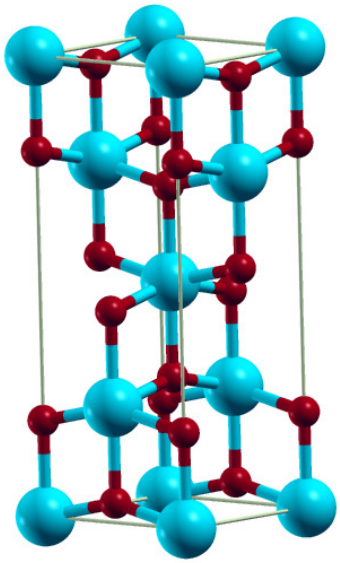

Figure 1.1: Bulk anatase TiO_2 ; Blue spheres are titanium atoms and small red spheres are oxygen atoms.

of $\sim$ 3.4 eV (Kavan et al., 1996). Peter, et al. (Peter et al., 1997) studied the structure and equilibrium shapes of anatase and rutile TiO_2 crystal and found out that for TiO_2 anatase crystal shown in Fig. 1.2, the surface morphology is mainly dominated by (101) and (001) planes. Zhang and Banfield (Banfield et al., 1998) performed a thermodynamic analysis of the phase stability of nanocrystalline anatase and rutile TiO_2. Their study predicts that anatase becomes more stable than rutile when the particle size is smaller than $\sim$ 14 nm, consistent with the observation that nanomaterials grow preferentially in the anatase phase and transform to rutile when the particle size increases (De Angelis et al., 2014).

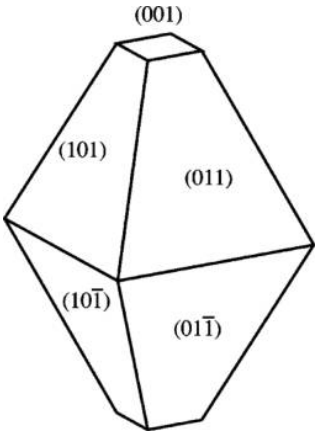

Figure 1.2: Equilibrium shape of a TiO_2 crystal in the anatase phase (Peter et al., 1997).

Most photovoltaic cells are based on granular thin films with an anatase structure (O'regan and Grätzel, 1991). In order to gain a better understanding of TiO_2-based de-

vices, it is clearly important to obtain atomic-scale information on well-characterized anatase surfaces. Several theoretical studies have predicted the stability of the different low-index anatase surfaces (Bredow and Jug, 1995b). The (101) face is the thermodynamically most stable surface with the lowest surface energy compared to other surface planes (100), (010), and (001). Bulk truncated anatase 101 surface is shown in Fig. 1.3A; it makes both 5-fold (Ti_{5c}) and 2-fold (O_{2c}) atoms to be under-coordinated, while 6-fold (Ti_{6c}) Ti atoms and 3-fold (O_{3c}) oxygens retain the bulk coordination (Ma et al., 2014).

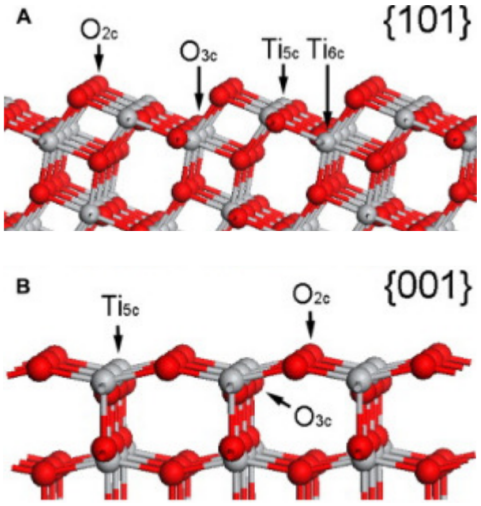

Figure 1.3: TiO_2 anatase 101 and 001 surfaces. Five-fold and six-fold Ti atoms are denoted as Ti_{5C} and Ti_{6C} , respectively; O_{2C} indicates a bridging, two-fold coordinated O atom, O_{3c} is a three-fold coordinated oxygen atom.

TiO_2 is biologically and chemically inert; it is also stable with respect to photo-chemical corrosion and it is cheap compared to other metal oxides. Due to its photostability, non-toxicity, and low cost, titanium dioxide (TiO_2) has found widespread applications in dye-sensitized solar cells (DSSCs), environmental protection such as air and water purification, decomposition of organic pollutants, sensors and in photoinduced hydrophilicity (Hashimoto et al., 2005; Thompson and Yates, 2006), among many other uses.

1.2 Titanium dioxide (TiO_2) photocatalysis

The study of semiconductor photocatalysis with main focus on TiO_2 as a photocatalyst has exponentially grown over the last three decades and generated considerable amount of interest. The extensive research efforts are mainly focused in understanding the fundamental processes and in enhancing the photocatalytic efficiency of TiO_2. This is inspired by the

potential applications of TiO_2-based photocatalysts in renewable energy and destruction of organic pollutants in air and water (Linsebigler et al., 1995).

Several semiconductors have band-gap energies sufficient to promote photocatalysis. Some of these semiconductors include; TiO_2, SnO_2, $SrTiO_3$, ZnO and ZnS (Fang et al., 2015). However, amongst these semiconductors TiO_2 has been exclusively considered to be an ideal candidate for photocatalytic processes due to its powerful oxidation ability, superior charge transfer characteristics, long-term stability against photochemical corrosion, nontoxicity, high availability, and low production cost (Pan et al., 2013). The metal sulfide semiconductors are unsuitable based on stability requirements in that they readily undergo photoadonic corrosion. ZnO appears to be an alternative to TiO_2 but it is unstable and easily leads to catalytic inactivation over time (Hoffmann et al., 1995).

TiO_2 shows relatively high reactivity and chemical stability under ultraviolet light (UV) (λ is less than 387 nm) (Zaleska, 2008). As mentioned earlier, TiO_2 anatase has a wide band-gap of 3.2 eV, hence a very small fraction of solar light (about 3-5%) in UV range can be utilized. The development of visible light responsive-TiO_2 photocatalyst to exhibit high reactivity under visible light ($\lambda > 400$ nm) has been of great concern since it allows solar light which represents a clean and renewable source of energy, even under poor illumination, to be effectively utilized. There are several approaches that have been proposed to shift TiO_2 absorption to visible range such as use of transition metal-ion implanted TiO_2 (Cu, Co, Ni, Cr, Mn, Mo, Nb, V, Fe, Ru, Au, Ag, Pt) (Yamashita et al., 2001), reduced TiO_2 photocatalysts (Takeuchi et al., 2000), anion-doped TiO_2 (nitrogen, sulphur, carbon, boron, phosphorus, iodine, fluorene) (Serpone, 2006), cations-doped TiO_2 (Fe^{3+}, Mo^{5+}, Ru^{3+}, etc. (Serpone, 2006), composites of TiO_2 with semiconductor having lower band gap energy (e.g. CdS, CdSe particles (Hirai et al., 2001), sensitizing of TiO_2 with dyes (e.g. catechol, squarine) (Hartmann Douma and Gebauer, 2011; Meng'wa et al., 2016) and TiO_2 doped with upconversion luminescence agent (Wang et al., 2006). The composites thus obtained allows for the formation of a doping energy level between the conduction band and the valence band of TiO_2, subsequently extending the adsorption capacity to the visible region. Moreover, the electrons from the conduction band are transferred on the metal particle, thus increasing the lifetime of the charge carriers and thereby reducing the recombination rate. However, until now, their performance activity has roughly increased by a factor of 2-3

relative to a benchmark such as Degussa P-25 (Tachikawa et al., 2007). In addition, there are a number of problems associated with their durability and reaction selectivity.

TiO_2 photocatalytic activity is also hampered by the recombination of the photogenerated electron-hole pairs. Titania exhibits weak energy gap emission upon the recombination of conduction band electrons with valence band holes, and the non-radiative recombination, which involves trapped states is also optically feasible (Emeline et al., 2005). Recombination is caused by impurities, defects or other factors, which create bulk or surface imperfections into the titania crystal. The introduction of species either in bulk or surface to enhance charge separation may reduce this effect, and enhance photocatalytic efficiency. Modification of TiO_2 to extent absorption to the visible range and suppress recombination is highly designable. This process should however be treated with care, since some dopants/modifiers could also work as recombination centres for electrons and holes.

Incorporating transition metals and metal oxides has proven to be an effective strategy to tailor the structure, phase, and band gap of TiO_2 based photocatalysts. Among them, copper is considered to be one of the most suitable elements due to the narrower band gap of cupric oxide and cuprous oxide (Ma et al., 2010b). Xin, et al. (Xin et al., 2008) have demonstrated that a Cu–TiO_2 system with the appropriate content of Cu becomes a strong trap for electrons, thus inhibiting the recombination of photoinduced charge carriers and improving the photocatalytic performance of TiO_2. Additionally, cupric and cuprous oxides and metallic copper are almost nontoxic. TiO_2 coupled with copper oxides enhances absorption of visible light and ensures separation of electron-hole pairs.

1.3 Copper Oxides

Transition metal oxides (TMOs) are a class of materials, whose conducting properties range from metallic to semiconducting and which have been developed for a variety of novel advanced functional material applications. Copper oxides belong to this class of materials and they have attracted increasing interest in numerous fields in recent years, including photocatalysis, as energy materials, supercapacitors, batteries, gas sensors, and other applications (Mishra et al., 2016). Copper oxide is a p-type semiconductor and its three binary phases are cuprous oxide (Cu_2O), cupric oxide (CuO), and paramelaconite (Cu_4O_3) (Meyer et al.,

2012). Cu_2O is one of the stable phases and well studied of the three well-established copper-oxide compounds. Cu_2O is a visible-light-responsive semiconductor that has been used as inorganic sensitizer to extend the light response range of wide-band-gap semiconductors such as TiO_2 to visible range. Cu_2O nanoparticles extend the visible light response of TiO_2 and inject electrons to the CB of TiO_2 that effectively participate in the hydrogen evolution reaction (Gawande et al., 2016). The application of Cu_2O itself as a photocatalsyt is limited due to its fast recombination of charge carriers, easiness to be oxidized and photo-corrosion (Jiang et al., 2015).

Cupric oxide (CuO) oxide is the most thermodynamically stable phase at ambient conditions (Schmidt-Whitley et al., 1974). Bulk CuO does not have the ability to split water to generate hydrogen because the CB edge of CuO is lower than the H^+/H_2 potential. However, the CB edge of CuO clusters is higher than that of bulk CuO and the H^+/H_2 potential due to the quantum confinement effect making them more effective at improving TiO_2 catalytic activity (Gawande et al., 2016). Paramelaconite, Cu_4O_3 has a tetragonal crystal structure, its a meta-stable phase of copper oxide and to date, it has only been synthesized as thin films, never as a bulk material (Meyer et al., 2012).

A variety of outstanding properties make copper oxide to be one of the most intensively studied inorganic materials. It's most relevant feature is probably a favorable band gap that varies from 2.17 to 1.35 eV when going from cuprous (Cu_2O) to cupric oxide (CuO) (Meyer et al., 2012). Within these limits, the gap can be tuned continuously by changing the oxide stoichiometry or substituting lattice oxygen with traces of sulfur or nitrogen (Meyer et al., 2013). The adjustable gap size largely overlaps with the solar spectrum, a fact that makes copper oxide a promising absorber material for thin-film solar cells (Minami et al., 2014). Its potential to fabricate photovoltaic and microelectronic elements had already been realized in the 1920's, and the material has been a focus of research ever since (Grondahl, 1933).

Carbon dioxide is the primary greenhouse gas responsible for global warming and recent climate changes (Tachikawa et al., 2007). In the past few years, copper oxides have been investigated extensively as catalysts in photochemical and electrochemical CO_2 reduction (Mishra et al., 2016) and photocatlytic water splitting for hydrogen production (Xu et al., 2011). However, almost all catalysts, including copper oxides, still suffer from low selectivity and activity. Consequently, there is need to understand the mechanisms responsible for

photocatalytic activity so as to be able to design better photocatalysts and improve their performance.

1.3.1 Cuprous Oxide (Cu_2O)

Cu_2O is a Bloch semiconductor which crystallizes in a simple cubic Bravais lattice (Heinemann et al., 2013). Its space group is ($Pn\bar{3}m$) or O_h^4 with a lattice parameter of 4.270 Å(Heinemann et al., 2013). Its unit cell contains six atoms, with the four copper atoms being positioned in a face-centred cubic lattice (reddish brown spheres as shown in Fig. 1.4), while the two oxygen atoms are located at tetrahedral sites forming a body-centred cubic sub-lattice (red spheres), see Fig. 1.4. As a consequence, oxygen atoms are four-fold coordinated with copper atoms as nearest neighbours, and copper atoms are linearly coordinated with two oxygen atoms as nearest neighbours.

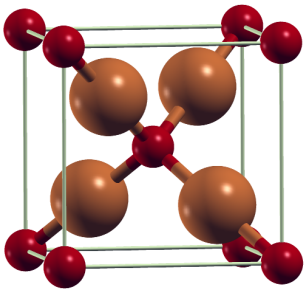

Figure 1.4: Crystal structure of cubic Cu_2O. Reddish brown spheres: copper atoms; red spheres: oxygen atoms.

Cu_2O is naturally a p-type semiconductor and has a direct band gap of 2.17 eV and an optical gap of 2.62 eV (Heinemann et al., 2013). Cu_2O is of great interest in catalysis (Poizot et al., 2000) and semiconductor fields due to its material abundance, preparation simplicity, nontoxicity, and suitable band gap. Its p-type conduction property and broad response to visible light (VL) suggest that one of the most important applications of Cu_2O is its function as a component in a photovoltaic solar cell. It was found that by combining Cu_2O with an n-type semiconductor, such as TiO_2, the new composite materials show good energy conversion efficiency, implying that it is an economical candidate to replace the traditional high-cost crystalline silicon solar cell. In addition, it is also a promising material in developing transparent conducting electronic devices by alloying with alkaline-earth oxides (Nolan and Elliott, 2008). As a catalyst, Cu_2O has been found to degrade organic pollutants in wastewater under visible light (Ma et al., 2010a).

1.3.2 Cupric Oxide (CuO)

CuO has a monoclinic crystal structure with C2/c symmetry, (Åsbrink and Norrby, 1970) as shown in Figure 1.5. Experimentally, it is known that CuO has a local magnetic moment per formula unit of 0.65− 0.69 μB (Forsyth et al., 1988).

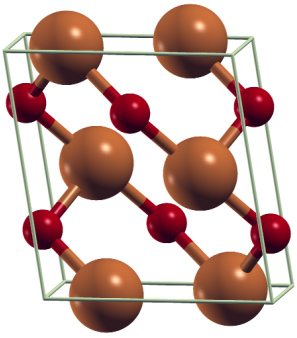

Figure 1.5: Crystal structure of monoclinic CuO. Reddish brown spheres; copper atoms, red spheres; oxygen atoms.

CuO is a material of special interest since it is one of the few intrinsic p-type semiconductors with a narrow band gap (1.2-1.9 eV)(Heinemann et al., 2013) and hence it can be used for fabrication of p-n heterojunctions with other n-type metal oxides such as TiO_2 for solar technology applications. Furthermore, CuO may find applications in lithium ion batteries and field emission devices. Fundamentally, cupric oxide is a Mott insulator and is believed to share a lot of common ground in physics with high-TC superconductors and spintronics oxides (Vukojević et al., 2005). Bulk CuO has an antiferromagnetic (AFM) ground state, with a Neel temperature in the range of 213-230 K.

1.4 Copper oxide clusters

The attractiveness of studying atomic clusters arises from the fact that they offer the opportunity to examine how atomic or molecular properties evolve into that of the condensed phases, and represent interesting molecular species that often exhibit remarkable physical and chemical properties (Jena et al., 2013). Their finite sizes make more accurate *ab initio* calculations possible, and provide ideal models to study local effects taking place on surfaces and in the bulk (Rayner et al., 1995). Despite considerable experimental advances in the last decade, there is yet no direct experimental method to determine the structures of free clusters. On the other hand, theoretical approaches have proven to be highly accurate in

determining molecular structures that can be used to obtain definitive cluster structural information.

Metal oxide clusters, at which little efforts have been directed, are interesting due to the scientific and technological importance of oxide materials (Henrich and Cox, 1996). Combined modelling and experimental evidence has reported that modification with sub-nanometre surface-bound metal oxide clusters can extend the valence band of TiO_2 by formation of interfacial bonds which induce new electronic states in the energy gap (Tada et al., 2014). This was demonstrated for the examples of NiO (Iwaszuk et al., 2013) and SnO (Iwaszuk and Nolan, 2013) modified rutile and anatase TiO_2 by the upshift of the valence band edge due to new oxide cluster derived states. Modelling has been successfully used to predict the nature and oxidation states of the oxide cluster modifier (Tada et al., 2014; Nolan et al., 2016; Fronzi et al., 2016b), the red shift (Tada et al., 2014; Nolan et al., 2016; Fronzi et al., 2016b) and the reactivity of the composite material (Iwaszuk and Nolan, 2011; Fronzi et al., 2016a).

The presence of surface species on a substrate material, modulates band edge potentials, through disruption of the lattice order and can act as trapping sites for photogenerated charges (Kamat, 2012; Reynal et al., 2013). Localisation of photogenerated electrons into these surface clusters allows the chemical nature of the surface cluster to then influence electrochemical reduction and hence product distributions. By considering photocatalyst modification with molecular clusters and charge localisation at a co-catalyst site, (Nolan et al., 2014; Iwaszuk et al., 2014) these surface modifiers can be considered to behave like electrocatalysts.

Copper oxide clusters are very important because they provide better model systems to understand the electronic structure of copper oxide materials relevant to the copper oxide applications. Metallic copper clusters can scavenge VB holes and provide an alternative charge separation pathway (Linic et al., 2011). Cu(0) can also inject charges into the CB of TiO_2 via localized surface plasmon resonance (Yasomanee and Bandara, 2008). Cluster studies can also provide relevant information regarding the understanding of the bulk properties of copper oxide materials.

The structures of small clusters containing a few to hundreds of atoms are different from bulk materials. In an atomic cluster, most of the atoms are located at the surface and hence

its structural crossover phenomena and electronic confinement effects (Yang et al., 2010) determine physical and chemical properties of materials. The copper clusters under investigation here are truncated from bulk Cu_2O and CuO, as well as from tetrahedron copper cluster with adsorbed molecular O_2. The study of Cu_2O and CuO clusters is expected to shed light on our present knowledge of Cu_2O and CuO photocatalysis and other applications of cuprous and cupric oxide-based materials.

1.5 Water Splitting

Water electrolysis combined with renewable energy sources such as solar or wind provides a promising path for sustainable hydrogen production for fuel cell electric vehicles (Yoshida and Kojima, 2015) and energy-to-gas storage of variable energy sources (Elliott, 2016). One of the greatest challenges towards large-scale utilization of these clean energy technologies is reducing the hydrogen production cost. This may be achieved using photoelectrochemical (PEC) water splitting cells that directly convert water and sunlight to hydrogen and oxygen. The water splitting reaction ($2H_2O \rightarrow O_2 + 2H_2$) is endothermic; reactants and products are at equilibrium at an applied bias of 1.23 V with respect to the reversible hydrogen electrode (RHE) (Prévot and Sivula, 2013). In a photoelectrochemical cell, two half-reactions take place at different electrodes, the oxygen evolution reaction (OER) at the photoanode and the hydrogen evolution reaction (HER) at the cathode. The two reactions can be written as $2H_2O \rightarrow O_2 + 4H^+ + 4e^-$ and $4H^+ + 4e^- \rightarrow 2H_2$, respectively. The OER is a major obstacle as it generally requires a large overpotential (Dau et al., 2010), and this is the motivation driving the current research.

TiO_2 is one of the most suitable photoanode semiconductor materials. However, it still suffers from low OER activity due to high overpotential. Nozik (Nozik, 1975) determined an overpotential of about 1 V at a TiO_2 rutile anode. First-principles calculations based on Nørskov's approach confirmed this, with an overpotential of 0.78 V on the (110) surface of rutile (Valdes et al., 2008), and of 1.39 V on the (101) surface of anatase (Li et al., 2010). Previous works (Chen and Mao, 2007; Liu et al., 2013a) have explored doping TiO_2 with various elements to reduce the overpotential and shift absorption range from ultraviolet to visible range. Despite these efforts, it is still unclear how to design a photocatalyst with

high OER activity, largely because the mechanisms, chemical processes and kinetics of the OER are not fully understood.

Copper oxides are active on their own. Cu_2O has been reported as photocatalyst for water splitting under visible light irradiation (Michikazu et al., 1998), while CuO is an active catalyst for OER. In an experimental study of different morphologies of CuO as water oxidation catalysts, CuO nanowire exhibited the lowest overpotential for water oxidation with an onset potential of $\sim$ 0.90 V at pH 9.2 (Liu et al., 2015b). Further reduction of the onset potential to $\sim$ 0.8 V (vs. RHE) at pH 13.6 towards OER was also established in annealed CuO on fluorine doped tin oxide (Liu et al., 2016). Moreover, copper oxides enhance absorption of visible light with respect to pure titania. Finally, the presence of titania and copper oxides might be favourable for separation of electron-hole pairs.

1.6 Statement of the problem

Sustainable energy demand and environmental protection have heightened research and development of clean renewable sources. Water splitting process for hydrogen (H_2) and oxygen (O_2) production, which in-turn serve as efficient fuels and CO_2 reduction to hydrocarbon fuels that could reduce dependence on fossil fuels and the levels of CO_2 in the atmosphere are the most viable options. These are energy intensive processes that require an efficient and cost effective photocatalyst to make them possible. Cu_2O and CuO have been found to be effective cocatalysts to TiO_2 for photocatalytic water spitting and CO_2 photoreduction. However, the increased photocatalytic efficiency for water splitting and CO_2 reduction by TiO_2 based catalysts under visible light is still limited for practical applications due to the recombination of photogenerated charge carriers and absorption in the UV region of the solar spectrum.

In order to improve the photocatalytic performance of Cu oxides sensitized TiO_2, there are fundamental questions that need to be resolved about the mechanisms of photoabsorption, charge separation and transfer, and reaction. In particular, the role of copper oxides in each of these steps remains to be elucidated, and such understanding could lead to a more systematic improvement of the catalyst's properties. Regarding the effect of supported copper clusters on photoabsorption, the theoretical evidence of Cu_{1-4} clusters modified TiO_2

anatase surface (Seriani et al., 2015) has shown that formation of copper-induced Ti^{3+} states might be the main contribution of copper to the enhancement of the photocatalytic activity of titania. To date, literature reports of copper oxide clusters on TiO_2 anatase surface substrate are still scarce and those available present inconsistent ideas. These coupled semiconductor systems could shed light on how different variables such as shape, oxidation state and size of the catalyst as well as photocatalytic subprocesses enhance photocatalytic activity .

In this work, an intensive structural search of Cu_2O and CuO clusters mounted on TiO_2 (101) surface has been performed to determine the most stable configurations. The electronic structure characterization of Cu_2O/TiO_2 and CuO/TiO_2 were carried out to establish the specific role of copper oxide clusters to the mechanism of the photocatalytic process. The thermodynamic stability of the most stable copper oxide clusters on TiO_2 anatase surface in an oxygen atmosphere at finite temperature and pressure has been examined to determine the best operating conditions of the catalyst. This study also investigated the behaviour of water adsorption on Cu_2O/TiO_2 and CuO/TiO_2 system, so as to determine the most favourable water adsorption sites. Furthermore, the energetics of the full water cycle on the most stable water terminations on Cu_2O/TiO_2 and CuO/TiO_2, hence the water photo-oxidation reaction has been explored to deepen the understanding of water splitting processes.

1.7 Justification of the study

Hydrogen (H_2) is considered to be an important future source of energy because it is clean, abundant, flexible (optimal carrier for many applications such as transportation) and highly efficient (Chen et al., 2016). The direct production of hydrogen from photocatalytic water splitting is one of the most desired routes to generate hydrogen since it is based on solar energy, which is abundant, renewable and environmentally safe. Several approaches have been proposed to increase the hydrogen production rate of the photocatalytic process and one of them is to incorporate transition metal oxides and noble metal nanoparticles to the semiconductor as cocatalyst. However, their are high costs incurred by the use of noble metals. Hence, increasing attention has been dedicated to $Cu/Cu_2O/CuO$ nanoparticles

dispersed on TiO_2 (Xu and Sun, 2009) to attain a cost-effective photocatalyst. Copper species with smaller bandgap and higher work function than bare TiO_2 facilitates light harvesting and charge carrier separation in Cu_2O/TiO_2 and CuO/TiO_2. Accumulation of electrons enables the Cu species to act as proton reduction sites and enhance the production of hydrogen (Xu et al., 2010). Nevertheless, the performance of different Cu species (CuO vs. Cu_2O vs. metallic Cu) is not clear.

Although, Cu is cheaper than noble metals, limited studies on the photocatalytic performance of Cu nanoparticles have been reported due to the fact that Cu nanoparticles are easily oxidized to Cu_2O or CuO upon exposure to air or traces of oxygen molecules (Zhang et al., 2015). Upto date, few works have been conducted on the preparation and photocatalytic performance of copper oxide clusters anchored on TiO_2, but it is speculated that such structured systems, could enhance the perfomance of TiO_2 photocatalysts. The present work deepens the understanding of the effects of metallic Cu, CuO and Cu_2O on anatase TiO_2 photocatalytic applications.

Available literature shows that Cu_2O/TiO_2 and CuO/TiO_2 interfaces have not been studied sufficiently, particularly, regarding relative band positions, and the most active Cu species for CO_2 photoreduction and photocatalytic splitting of water. For example, disagreements exist with respect to which Cu species from the oxides is mainly responsible for photo-catalytic reactions. Mori et al. (Mori et al., 2012) reported that Cu^+ species is the most active compared to Cu^{2+} and Cu^0. However, Slamet et al. (Slamet et al., 2005) suggested that Cu^{2+} was more active than Cu^+ and Cu^0. Hirano et al. (Hirano et al., 1992) indicated that metallic Cu deposited on anatase TiO_2 will enhance the photoefficiency of CO_2 reduction, where the Cu metal plays the roles of being both as effective co-catalyst for the reduction of CO_2 and as a reducing species to react with the positive holes simultaneously. On the contrary, Tseng et al. (Tseng et al., 2004) pointed out that the presence of CuO on Cu/TiO_2 decreased the production of methanol from CO_2. Clearly, it is disputable in the literature what the most active Cu species is as the co-catalyst of TiO_2 for CO_2 photoreduction with H_2O. Furthermore, the existing uncertainties make it difficult to determine, which between CuO/TiO_2 and Cu_2O/TiO_2 interfaces might be better for solar spectrum absorption.

TiO_2 is one of the most important photoanode materials for the oxygen evolution reaction

(OER). However, water splitting on TiO_2 still displays a large overpotential ($\approx$ 1.39 V (Li et al., 2010) as mentioned before) for the oxygen evolution reaction. Intense research efforts have been devoted to reducing the OER overpotential on TiO_2. Liu et al. (Liu et al., 2013a) established in their experiments that TiO_2 doped with different transition metals (TM) considerably suppressed the overpotential for oxygen evolution reaction (OER). Nevertheless, doping can lead to defects that can act as recombination centres, thus reducing the efficiency of the photocatalyst regardless of the visible light absorption (Fronzi and Nolan, 2017). Besides doping, another effective strategy to enhance TiO_2 photocatalytic activity is to couple with Cu_2O and CuO nanoparticles/clusters. Gawande et al. (Gawande et al., 2016) reported that Cu_2O and CuO nanoparticles/clusters coupled to TiO_2 significantly enhanced HER. It is however unclear what is the main mechanism leading to an improved activity in copper-modified titania. In order to clarify the effect of copper modification on the functional behaviour of titania towards water splitting, it is necessary to investigate the processes contributing to the reaction. An atomic-level understanding of the OER chemical processes on Cu_2O/TiO_2 and CuO/TiO_2 not only would be of great scientific interest, but could also be helpful for the design of photoelectrochemical water splitting cells with improved efficiencies.

1.8 Objectives

The General objective:

To theoretically synthesize copper-modified titania photocatalysts and carry out photocatalytic water splitting processes on the most stable systems.

The specific objectives are:

Use quantum ESPRESSO code and first principle atomistic thermodynamics;

1. To obtain the structural, thermodynamic and electronic properties of bulk cuprous (Cu_2O) and cupric (CuO) oxides .

2. To determine the most stable configurations of Cu_2O and CuO clusters mounted on TiO_2 (101) anatase surface using QE code.

3. To determine electronic properties and thermodynamic stability of the most stable Cu_2O/TiO_2 and CuO/TiO_2 systems.

4. To determine the most preferred water adsorption sites on the Cu_2O/TiO_2 and CuO/TiO_2 systems.

5. To determine water photo-oxidation reaction on Cu_2O/TiO_2 and CuO/TiO_2 coupled semiconductor systems.

CHAPTER TWO

LITERATURE REVIEW

2.1 Titanium dioxide for photocatalysis

Titanium dioxide (TiO_2) has long been regarded as one of the most promising photocatalytic material to generate hydrogen from water under solar light irradiation. TiO_2 is environmentally friendly and thus is considered a 'green' catalyst. As mentioned before, TiO_2 has three common crystalline phases: anatase, rutile and brookite; all these phases consist of TiO_6 octahedra and are characterized by distortion of their octahedral units and the manner in which edges and corners are shared (Hwang et al., 2015). The focus in this review is on the anatase phase. The energy gap of anatase is 3.2 eV (corresponding to $\sim$ 384 nm). As for the electronic structure, the top of the valence band maximum (VBM) has the non bonding O 2p orbital from the Ti_3O cluster plane, whereas the conduction band minimum (CBM) has Ti 3d orbitals. No electronic states exist within the band gap. The electronic band structure influences the photon absorption process and redox reaction ability for photocatalysis. Upon exposure to the required photon energy (excited electrons with energy greater than the energy gap), electrons in the valence band will be excited to the conduction band while leaving positively charged holes in the valence band. This is shown by the following expression (Gao et al., 2015):

$$TiO_2 + hv \rightarrow TiO_2(e^-) + TiO_2(h^+). \tag{2.1}$$

The photogenerated electron-hole pairs have three possible fates: (i) be captured and trapped by defect sites within or on the surface of the material, (ii) recombine and release energy in the form of heat or light, or iii) migrate to the surface and generate radical species. Outcomes from (i) and (ii) are known as 'deactivation processes' since these electron–hole pairs do not play any part in photocatalysis. Therefore, the photocatalytic efficiency is determined by suppressing process (i) and (ii), while enhancing process (iii) at optimized conditions. Two strategies are commonly adopted to improve the photocatalytic property of TiO_2: we can either increase the amount of charge carriers produced upon irradiation by lowering the bandgap, or engineer the surface to prevent the recombination of the photo-

generated electron-hole pairs.

2.1.1 Generation and Fate of the Photoinduced Charge Carriers

When TiO_2 is exposed to ultrabandgap illumination, electron-hole pairs are generated in the outer surface region of the material because of the short penetration depth ≈ 160 nm (Eagles, 1964) of the UV light. Recombination is retarded in the space charge region since electrons and holes move in different directions due to the near surface electric field. Continuous irradiation will result in the annihilation of this electric field, that is, band flattening.

The efficiency of photocatalytic processes can be evaluated by the measurement of the photonic efficiency ζ, that is, the rate of the formation of reaction products divided by the incident photon flow (Hoffmann et al., 1995), and is, unfortunately, usually found to be rather small. In fact, time-resolved spectroscopic studies reveal that most of the photogenerated e^-/h^+ pairs ($\sim$ 90 %) recombine rapidly after excitation. This is assumed to be one reason for the relatively low ζ-values ($\sim$ 10 %) of most semiconductor-based photocatalytic reactions (Hoffmann et al., 1995).

2.1.1.1 Electron/hole Recombination

The photocatalytic activities of TiO_2 photocatalysts are usually limited by the fast recombination of the photogenerated electron-hole pairs. The recombination of the charge carriers can occur upon heat evolution by non-radiative pathways or be accompanied by light emission via irradiative routes (Serpone et al., 1995). This can proceed through different pathways due to the presence of trap states. TiO_2 has an indirect bandgap, hence exhibits only very weak energy gap emission upon the recombination of conduction band electrons with valence band holes, while the irradiative recombination involving trap states is optically allowed (Emeline et al., 2005). The surface trapped electrons in anatase are found to be located about 0.7-1.6 eV below the conduction band edge referring to oxygen vacancies, while the trapped holes are located about 1.8-2.5 eV below the conduction band edge (Schneider et al., 2014). Yamada et al. (Yamada and Kanemitsu, 2012) found longer lifetime for electons in anatase (> few ms) in comparison to rutile (24 ns), while the decay for the holes in both crystal phases occurs on the nanosecond time scale. Generally, it is assumed that in TiO_2 the photogenerated electron-hole pairs predominantly recombine via

non radiative pathways. The non radiative recombination in photoexcited systems leads to the rapid dissipation of energy. Leytnar and Hupp found that approximately 60 % of all trapped electron-hole pairs recombine on the time scale of about 25 ns, releasing 154 kJ/mol of energy as heat (Leytner and Hupp, 2000). It was also demonstrated that if the heat is released non adiabatically, this recombination energy is sufficient to provoke the deaggregation of TiO_2 nanoparticle aggregates (Stopper and Dohrmann, 2000; Pagel and Dohrmann, 2007; Mendive et al., 2011). This photodeaggregation process increases the adsorption capacity of the photocatalyst, for example, for water molecules, without increasing its mass. Studies of recombination kinetics (Katoh and Furube, 2011) show that electron-hole recombination can be affected by many factors such as the sample preparation, the reaction temperature, the charge trapping, the interfacial charge transfer, and the excitation light intensity. Consequently, the lifetime of the charge carrier recombination in TiO_2 extends from the picosecond to the millisecond time scale.

2.1.1.2 Hole trapping

Photogenerated charge carriers do not recombine directly because the electron-hole pairs can explore other possibilities such as hole trapping at the semiconductor's surface. Many studies have been performed to establish the nature of the trapping sites for photogenerated holes in titanium dioxide (Henderson, 2011). It's believed that holes can be trapped either at a bridging O^{2-} or they can be transferred to surface-bound OH^- anions resulting in the formation of O^- or/and OH centers, respectively. Analysis of some EPR spectra illustrates that the oxidation of water on the TiO_2 surface through valence band holes leads to the formation of the OH radicals. Bredow et al. (Bredow and Jug, 1995a) found in their model calculations that the potential barriers for the desorption of free OH radicals are too high; that is, the formation of free hydroxyl radicals in TiO_2 photocatalysis is considered to be highly unlikely. Following the initial generation of surface-bound hydroxyl radicals, the formation of hydrogen peroxide and of peroxide radicals bound to the surface is rather favored (Bredow and Jug, 1995a; Diesen and Jonsson, 2014). Imanischi et al (Imanishi et al., 2007) found effective O 2p levels to be far below the valence band of TiO_2, hence the oxidation of adsorbed water molecules to OH aqueous radicals through the photogenerated holes was excluded. This conclusion was supported by reported results (Berger et al., 2005), which

clearly showed that the primary products of the hole trapping are not superficially bound or free OH aqueous radicals but rather O_s^- radical ions in the TiO_2 lattice. Nevertheless, formation of OH radicals during the photocatalytic process cannot be completely excluded, because OH radical species can be formed either through the electroreduction of dissolved oxygen by photogenerated electrons or acidic solution (Schneider et al., 2014).

2.1.1.3 Electron trapping

Due to upward band bending in hydroxylated n-type TiO_2, the photogenerated electrons are forced to move from their surface into the bulk, where they can be delocalized over different Ti sites. Both theoretical and experimental studies are predicting bulk (subsurface) trapping rather than surface trapping of these electrons (Bredow and Jug, 1995a). However, alternative studies also exist demonstrating that Ti^{4+} OH groups located at the TiO_2 surface can act as trapping centers for the electrons, resulting in the formation of Ti^{3+} OH species. Such species can attract holes, thus behaving as recombination centers (Di Valentin et al., 2006). Di Valentin et al. (Di Valentin and Selloni, 2011) reported that holes and electrons populate surface sites due to the following reasons: (1) The lattice relaxation associated with the trapping is more feasible at the surface than in the bulk because of the possibility for the surface structure to relax with fewer constrains. (2) At the surface the energy levels calculated for the self-trapped charge carriers are deeper in the gap with respect to the bulk levels, confirming that there is a driving force for electrons and holes to migrate to the surface. When debating whether the electrons are rather trapped at the surface or in the bulk of a TiO_2 particle, the particle size effect should also be considered, because the upward band bending will decrease with the particle size. Peiro et al. (Peiró et al., 2006) studied the lifetime of trapped electrons in nc (nanocrystalline) TiO_2 films employing transient absorption spectroscopy and reported in the absence of ethanol (electron donor) and O_2 (electron acceptor) a half-life of its absorption signal of ~ 25 μs.

Carneiro et al. (Carneiro et al., 2011) investigated dependence of the lifetime of free bulk electrons on the anatase TiO_2 particle size and reported that a faster decay of the mobile charge carriers in smaller particles. Assuming that the decay is predominantly caused by the trapping of the conduction band electrons, the Time-resolved microwave conductivity (TMRC) data indicate that the samples with an average particle diameter below 15 nm are

likely to contain a larger concentration of trapping sites as compared to the larger particles (Carneiro et al., 2009). This suggests that electron-trapping process is more efficient for smaller TiO_2 particles exhibiting a larger surface area (Murakami et al., 2011).

2.1.2 Photoexcited Electron Transfer at the TiO_2 Surface

Photogenerated electrons and holes can easily be transferred to electron and hole acceptors, respectively, provided that the respective energetic requirements are satisfied. The quantum efficiency (Serpone and Emeline, 2002) of these reactions depends on the charge-transfer rate at the interface, on the recombination rate within the particle, and on the transit time of the photogenerated charge carriers to the surface. According to Tamaki et al. , both the photogenerated electrons and holes in nanocrystalline TiO_2 films reach the surface in 170 fs and 220 fs, respectively (Tamaki et al., 2007). The calculated hole trapping times correlate very well with the experimentally observed values. In contrast, a considerable discrepancy exists for the electron trapping time. The probable reason for this discrepancy is that free electrons generated upon 355 nm excitation still contain part of the excess energy and may therefore have a larger diffusion coefficient than the reported value (Tamaki et al., 2007). However, Warman et al. have found by means of TRMC measurements that the electron mobility of the photogenerated free electrons increases remarkably from 0.05×10^{-4} to 1.5×10^{-4} $m^2/V{\cdot}s$ with increasing particle size from 5 to 50 nm; thus the bulk-to-surface transit time is calculated to increase from 19 to 65 ps (Warman et al., 1991). These values are in agreement with the dependency of the lifetime of the photogenerated charge carriers on the particle size (Carneiro et al., 2009).

Tamaki et al. have also shown that after reaching the surface (within 170 fs) the photogenerated electrons migrate between surface and shallow bulk trap sites that are in equilibrium (Tamaki et al., 2007). These shallowly trapped electrons relax into deeper sites within 500 ps through hopping processes involving energetically distributed trapping sites as shown in Figure 2.1.

2.1.2.1 Photogenerated Reduction Reactions at the TiO_2 Surface

As mentioned before, photogenerated electrons are not directly available at the surface for the desired reactions, but that TiO_2 should rather be modified to activate the photogen-

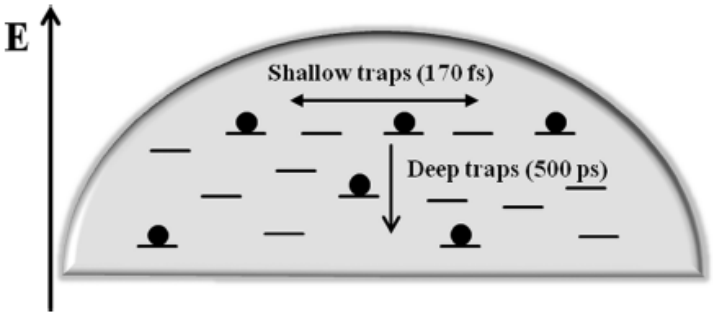

Figure 2.1: Spatial and energetic distribution of electron traps in a TiO_2 particle (Tamaki et al., 2007).

erated electrons for reduction reactions. Noble metal-modified TiO_2 nanoparticles usually exhibit enhanced photocatalytic activity resulting from an improved charge separation. According to the Schottky barrier model, this enhanced charge separation can be attributed to the transfer of the photogenerated holes to the surface and the simultaneous migration of the electrons into the bulk induced by the electric field in the space charge layer as platinum-modified TiO_2. However, results from diffuse reflectance spectroscopy experiments, contradict the Schottky barrier model, indicating that both trapped electrons and free bulk electrons migrate to the Pt contact and thus to the TiO_2 surface within a time interval of 1.4 and 2.3 ps, respectively (Furube et al., 2001; Iwata et al., 2004).

Upon illumination of metal loaded TiO_2, the influence of the excitation of the metal particle on the reaction dynamics of the photogenerated charge carriers needs to be taken into account. The metal nanoparticles can be characterized by their surface plasmon resonance (SPR), which is readily explained by the photoinduced collective oscillations of electrons at the surface of these nanoparticles (Daniel and Astruc, 2004; Tian and Tatsuma, 2005). Thus, an increased local electromagnetic field is generated upon illumination of the metal particles. The interaction of this localized electric field with the semiconductor induces the formation of charge carriers near the surface of the semiconductor; hence, these charge carriers can reach the respective surface sites on the semiconductor readily. This enhances the electron-hole separation and can, for example, lead to an increased visible light-induced photocatalytic H_2 evolution (Ingram and Linic, 2011).

2.1.2.2 Photogenerated Oxidation Reactions at the TiO_2 Surface

Photocatalytic systems, have efficient electron donors such as different alcohols. Tamaki et al. investigated the reaction dynamics of the trapped holes and found that in the presence of alcohols the transient absorption of the trapped holes decayed more rapidly, clearly indicating that trapped holes can react with these alcohols (Tamaki et al., 2006). The lifetime of the trapped holes in methanol, ethanol, and 2-propanol was found to be 300, 1000, and 3000 ps, respectively. The charge-transfer rate was also reported to be affected by the adsorption behavior of the adsorbates at the TiO_2 surface. Generally, it is assumed that the hole or OH-induced alcohol oxidation proceeds via two reaction steps: the first step includes the cleavage of the C-H bond resulting in the formation of the respective α-hydroxyalkyl radicals, while the formation of the respective aldehyde occurs in the second step under injection of an electron into the conduction band of TiO_2 (Schneider et al., 2014).

The photo-oxidation of methanol leads to the relocation of the trapped holes and to the accumulation of the electrons on the TiO_2 surface causing a downward band bending in the semiconductor. In the absence of molecular oxygen as effective electron scavenger, TiO_2 changes its color from white to blue, indicating the formation of Ti^{3+} centers. The photogenerated electrons are located in the respective traps at the photocatalyst surface and are now available for different reduction reactions (Mohamed et al., 2011; Mohamed et al., 2012). Montoya et al. (Montoya et al., 2014) derived the TOIET (terminal-oxygen indirect electron transfer) mechanism involving three reaction steps: (1) hole trapping at surface lattice oxygen atoms resulting in the formation of terminal oxygen radicals, which are able to react with dissolved substrate species; (2) the incorporation of terminal oxygen radicals into photooxidation products with the simultaneous generation of TiO_2 surface oxygen vacancies; and (3) the dissociative adsorption of O_2 or H_2O molecules into terminal oxygen vacancies resulting in the "healing" of the catalyst surface. The proposed TOIET mechanism doesn't consider the participation of free and also of surface-bound hydroxyl radicals in photocatalytic oxidation reactions, contrary to commonly assumed mechanisms involving hydroxyl radicals as major oxidative species. It is worthy to note that Hoffmann and co-workers have actually suggested that surficially adsorbed hydroxyl groups act as electron trapping sites (Szczepankiewicz et al., 2000).

The photocatalytic alcohol oxidation via trapped hole states clearly showed that the charge transfer depends on the difference between the oxidation potential of the substrate molecules and the oxidation potential of the trapped holes. However, one of the most interesting predictions of the electron transfer theory has been developed by Hush and Marcus. According to their theory, the rate of electron transfer increases with an increasing electrochemical driving force in the so-called normal region, while in the so-called inverted region the reactivity decreases again with a further rise of the electrochemical driving force (Hush, 1961; Marcus, 1964). During the reactions of the trapped electrons at the TiO_2 surface, the oxidation state of the lattice bound Ti atoms changes from 3 to 4, resulting in a higher reorganization energy and consequently a lower electron transfer rate constant (Moser et al., 1991). Moreover, electrons localized at trap states exhibit lower reactivity as compared to free charge carriers.

However, these electron transfer processes compete with the surface trapping of the conduction band electrons. Because the trapping processes proceed within a time span of less than 1 ps, the electron transfer times should attain 10-15 s to dominate within this competition (Tamaki et al., 2007; Moser et al., 1991). Because most interfacial charge-transfer processes are, however, found to be much slower, interfacial electron transfer processes usually involve trapped charged carriers, that is, electrons.

2.1.3 Photocatalytic Water Splitting

In 1972, K. Honda and A. Fujishima discovered the photosensitization effect of a TiO_2 electrode for the electrolysis of H_2O into H_2 and O_2 using a Pt metal electrode as cathode and a TiO_2 photoanode irradiated with UV light. They found that, under UV light irradiation of the TiO_2 electrode, electrolysis of water proceeded at a much lower bias voltage as compared to normal electrolysis (Fujishima and Honda, 1972). In 1977, G. N. Schrauzer and T. D. Guth reported the photocatalytic decomposition of H_2O on powdered TiO_2 photocatalysts loaded with small amounts of Pt or Rh metal particles (Schrauzer and Guth, 1977). This led to the development of the mechanistic picture that, on such Pt/TiO_2 catalysts, the photogenerated electrons in TiO_2 move to the Pt metal site where they induce reduction reactions, while photogenerated holes remain in the TiO_2 particle and migrate to its surface where they induce oxidation reactions (Frank and Bard, 1977; Halmann, 1978). Thus, the

charge separation of electrons and holes is the most important process in photocatalysis employing semiconducting materials (Anpo et al., 1991). Since then, photocatalysis employing various semiconductors has been the focus of intense investigations by a number of researchers (Schneider et al., 2014).

The reduction reactions are the basis of photocatalytic H_2 production. For water splitting, the CB level should be more negative than the redox potential of H^+/H_2, while the VB level should be more positive than the redox potential of O_2/H_2O (see Fig. 2.2) (Gao et al., 2015). However, this is only the thermodynamic requirement of the band structure. Its water-splitting performance is also influenced by more complicated factors such as crystallinity, surface area, surface functioning groups, and number of active sites. Furthermore, the water-splitting reaction also affects the material surface chemistry and local pH environment on a TiO_2 electrode.

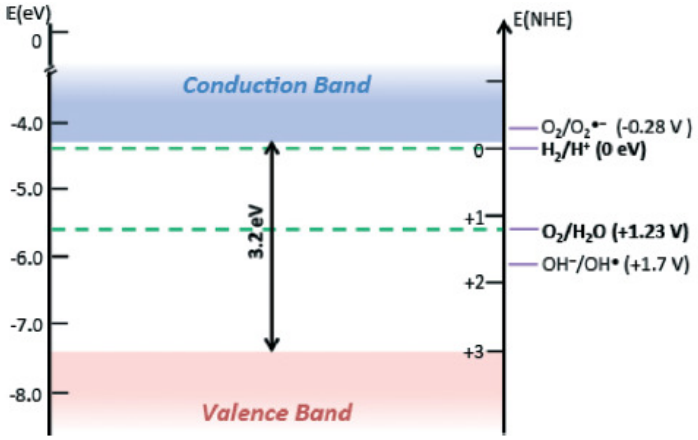

Figure 2.2: Position of CB and VB of TiO_2 and the redox potentials vs. NHE at pH 0 (Gao et al., 2015).

A PEC water splitting cell is shown in Figure 2.3 (Maeda, 2011). When the TiO_2 photoanode is irradiated, electrons excited to the conduction band will transfer to the counter electrode (Pt photocathode) where protons are reduced to molecular hydrogen (Schneider et al., 2014). Meanwhile, the holes left on the photoanode surface oxidize water and produce molecular oxygen. A proton exchange membrane is placed in the middle to separate each half-reaction and to balance the local pH environment. The half-reaction equations are written as equations (2.2) and (2.3) (Fujishima et al., 2000).

$$4e^- + 4H+ \rightarrow 2H_2 \tag{2.2}$$

$$4h^+ + 2H_2O \rightarrow O_2 + 4H^+ \tag{2.3}$$

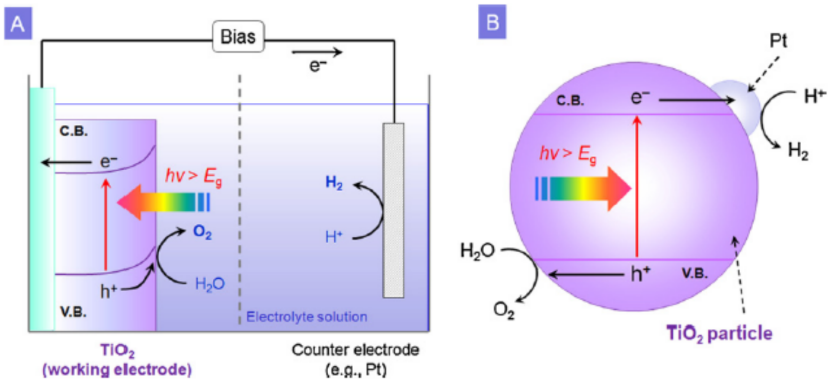

Figure 2.3: (A) PEC water splitting using a TiO_2 photoanode, and (B) a short-circuit model of a PEC cell (Maeda, 2011).

Several studies have shown that it is difficult to split water into H_2 and O_2 by pure TiO_2 photocatalysis in a simple aqueous system, due to the rapid electron– hole recombination process. To limit this drawback, sacrificial agents, such as reducing agents, are added to the aqueous solution. Sacrificial agents are reduced by the photogenerated holes instead of water, thereby enhancing the H_2 evolution reaction. Methanol, ethanol, EDTA, S^{2-}, I^-, IO_3^-, CN^-, Ag^+, and Fe^{3+} have all been applied as sacrificial agents (Liu et al., 2017) (ref. therein).

2.2 Copper oxide photocatalysis

Cuprous oxide (Cu_2O) is a p-type oxide semiconductor with a band gap energy of between 2.0-2.2 eV, hence photoresponsive in the visible region. In 1998, the Domen group reported for the first time that Cu_2O nanomaterials display visible light photocatalytic activity for water splitting (Michikazu et al., 1998) and catalyzed the splitting reaction without any noticeable decrease in activity for 1900 hours under visible light irradiation $\lambda \geqslant 460$ nm). The system's quantum efficiency in the spectral range between 550 and 600 nm was ~ 0.3 %, and this pioneering work prompted additional reports on newer methods for synthesizing nanostructured Cu_2O materials with enhanced catalytic activity. Zhao et al. (Zhao et al., 2014) reported the facile synthesis of hierarchically branched Cu_2O nanowires, in which thin nanowires (NWs) and nanosheets (NSs) served as the backbone and the branches, respectively.

These hierarchically nanostructured Cu_2O species exhibited remarkable catalytic activity for HER, far greater than that of Cu_2O NPs and nanowires. In another similar work, Zhang et al. reported the photochemical synthesis of Cu_2O microcubes derived from $CuWO_4$, (Zhang et al., 2014) which exhibited both high activity and good stability for hydrogen production from a glucose solution under visible light irradiation. The catalytic activity of the Cu_2O material was further improved by Zn doping (0.1 wt %), leading to an apparent quantum yield of $\sim$ 39 %. In addition, the construction of Cu_2O-noble-metal hybrid nanostructures has proven to be a viable way of improving the catalytic activity of Cu_2O toward HER (Bai et al., 2014; Wang et al., 2014a).

Hou et al. (Hou et al., 2016a) fabricated crystalline Cu-based nanowire arrays (NWs) including $Cu(OH)_2$, CuO, Cu_2O, and CuO_x on Cu foil (CF) according to the procedure shown in Fig. 2.4. After oxidation treatment (step 1, see Fig. 2.4), the CF surface was converted into dark blue $Cu(OH)_2$. Thereafter, calcination treatment of the $Cu(OH)_2$ film under different conditions led to the formation of self-supported copper oxide NWs. The oxygen evolution reaction (OER) activity of Cu-based nanowires on CF having an active area of 0.25 cm^2 in strongly alkaline electrolyte (0.1 M NaOH pH 12.8) was evaluated. Hou et al. reported that $Cu(OH)_2$ and CuO films exhibited excellent OER activity.

The onset potential of $Cu(OH)_2$ nanowire arrays for water oxidation appears at about 1.625 V, an overpotential of about 395 mV (the theoretical potential for water oxidation is 1.23 V vs. RHE) with a greatly enhanced catalytic current density. This is comparable to onset potential of 1.627 V, an overpotential of 397 mV for CuO thin film. The activities follow the order of $Cu(OH)_2 \approx CuO > CuO_x > Cu_2O$ under experimental conditions. Note that bare CF can also function as an OER catalyst, but shows a very low OER catalytic activity before onset potential of 1.8 V. It was proposed that surface Cu_2O is first oxidized to CuO, which could be further oxidized to highly valent Cu-oxo active component for OER. After oxygen liberation, the Cu-oxo species is restored to CuO. From this perspective, Cu_2O is the precursor rather than the exact active. Similar situation was found in the case of CuO_x. Therefore, CuO layer is the real catalyst responsible for the OER. On account of the much larger active electrochemical surface area, $Cu(OH)_2$ shows the best extrinsic catalytic activity. The low cost, easy accessibility, high activity at relatively low overpotential enable the self-supported Cu-based nanomaterials to be promising for practical applications.

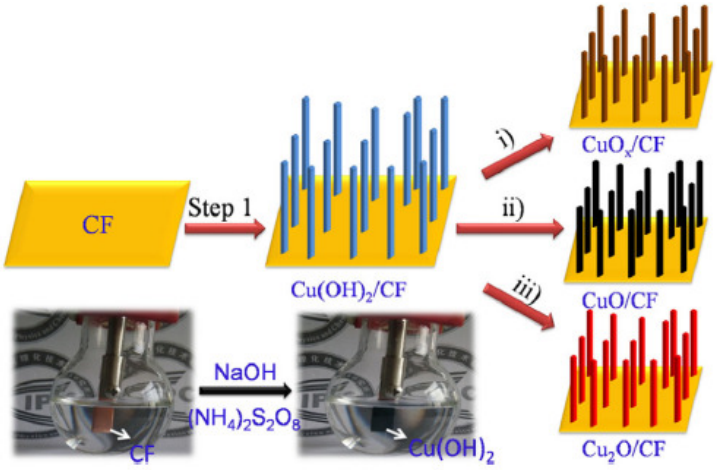

Figure 2.4: Cu-based nanowires (Hou et al., 2016a).

2.3 Semiconductor-titania Heterojunction system

TiO_2 coupled with other semiconductors with appropriate redox energy levels can lead to an increase in photocatalytic efficiency by improved charge carrier separation, hence an increase in the lifetime of the electrons-holes pairs. Therefore, proper choice of coupled semiconductors can generate heterojunction system towards visible light response. The merits of such a system are more efficient charge carrier processes, characterized by an increase in the lifetime of the charge carriers and an enhancement of the interfacial charge transfer efficiency to adsorbed substrate (Janczarek and Kowalska, 2017).

In the case of an efficient electron transfer between the semiconductor (SC) and TiO_2, the CB of TiO_2 must be more anodic than the corresponding band of the SC. Under visible light irradiation, only photoexcited electrons from the SC (sensitizer) conduction band are injected into the TiO_2 conduction band. If the valence band of the sensitizer is more cathodic than valence band of TiO_2, the holes generated in the semiconductor are retained. This phenomenon is shown in Figure 2.5a.

When the system of coupled semiconductors works under UV-VIS irradiation, both semiconductors are excited. Therefore, electrons in the CB of titania are injected from coupled semiconductor and, also photoexcited electrons from titania valence band under UV irradiation. This cumulatively raises concentration of electrons in CB of TiO_2. Meanwhile, holes left in the VB of TiO_2 may migrate to the VB of coupled semiconductor and increase concentration of holes in the coupled semiconductor/electrolyte interface as shown in Figure 2.5b (Bessekhouad et al., 2005).

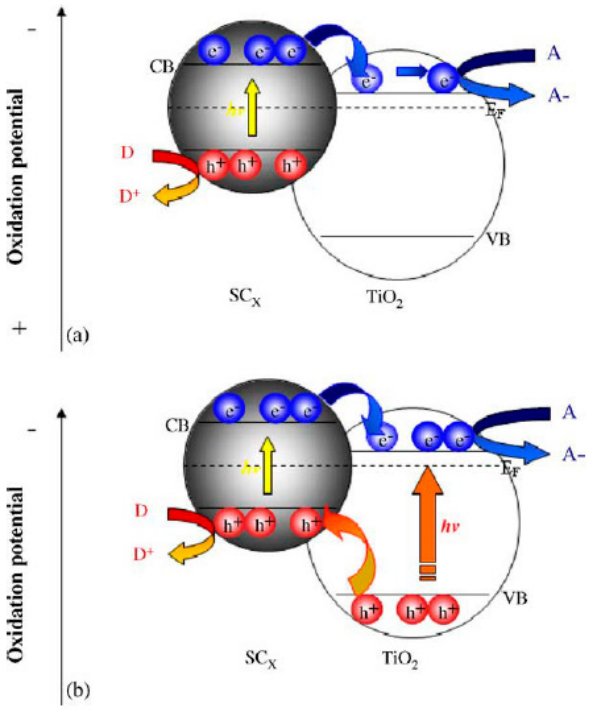

Figure 2.5: (a) Energy level diagram illustrating coupling of two semiconductors (SC_X) in which electron transfer occurs from light activated SC_X to non activated TiO_2. (b) Diagram showing coupling of SC_X in which movement of both electrons and holes is possible (Bessekhouad et al., 2005).

2.4 Photocatalytic activity of copper-modified titania

2.4.1 Introduction

Copper is a very promising metallic candidate for TiO_2 modification. Cu-based catalysts have significant nanotechnological applications in organic transformations, electrocatalysis and photocatalysis (Allen et al., 2013; Bhanushali et al., 2015; Clarizia et al., 2014). Copper is cheap compared to other noble metals, in fact its 100 times and 6000 times cheaper than silver and gold, respectively (Bhanushali et al., 2015). Moreover, copper, gold and silver belong to the same group in the periodic table, hence they share similar structural and electronic properties. Therefore, one expects a comparable potential in enhancement of TiO_2 photocatalytic activity and even better possibilities in application. As mentioned earlier, Cu^{2+}, Cu^{+} and Cu^{0} are the most active copper species in photocatalytic systems, this work will therefore shed more light on the nature of this copper species in TiO_2 photocatalysis.

Copper modified titania has very promising applications in photocatalytic oxidation both under ultraviolet (UV) and visible/solar irradiation. Therefore, in the following subsections an overview of different resulting mechanisms from various forms of copper combined with

titania in relation to efficiencies of photocatalytic systems is discussed.

2.4.2 Cu/TiO_2 photocatalytic system

Copper modified titania has received considerable attention, as this system is able to produce hydrocarbons from carbon dioxide and water vapor under solar illumination (Varghese et al., 2009; Roy et al., 2010; Shankar et al., 2009). Already, previous works involving TiO_2 nanotubes with copper particles have led to the production of carbon monoxide, hydrogen, and hydrocarbons (Varghese et al., 2009; Roy et al., 2010; Shankar et al., 2009). Hydrogen production was also observed when copper particles were embedded in nanostructured TiO_2 (Montini et al., 2011; Cargnello et al., 2011; Barreca et al., 2011; Gombac et al., 2009) . The electrocatalytic conversion of CO_2 to hydrocarbons seems to be dependent on the particle shape and surface morphology of copper catalysts (Tang et al., 2012). Such a dependence of catalytic activities on particle shape is typically linked to the surface chemistry of the catalyst. The oxidation state of copper plays a role in the activity of the catalyst as well, with nanocrystalline metallic copper being particularly active for the electroreduction of CO (Liu et al., 2013b). Liu et al. investigated the effect of different treatments during catalyst preparation for a Cu/TiO_2 photocatalyst for CO_2 reduction, and found that a reducing treatment gives the best activity (Liu et al., 2013b). Moreover, a high dispersion of the copper catalyst is important to achieve high conversion rates (Liu et al., 2012). Regarding the mechanistic aspects of surface chemistry of the Cu/TiO_2 system, it is known that CO_2 dissociates spontaneously on defective Cu(I)/TiO_2 in the dark (Liu and Li, 2014). It was proposed that electrons, trapped at Ti^{3+}-V_O sites, can migrate to CO_2 resulting in a dissociative electron attachment and in CO adsorbed to Cu^+ (Liu and Li, 2014). The reduced phase of pure titania (TiO_{2-x}), shows a Ti^{3+} state within the band gap. It is generally accepted that Ti^{3+} has an essential role in enhancing the photocatalytic performance of this material (Bennett, 2000; Pang et al., 2008; Zuo et al., 2010).

Seriani et al. (Seriani et al., 2015) investigated small copper clusters (Cu_{1-4}) atoms on the (101) and (100) surfaces of anatase TiO_2 by density functional theory (DFT+U), to shed light on the interaction between copper and titania and its effect on the electronic structure of the system. Its reported that the effect of the Cu clusters on the electronic structure of titania is 2-fold. First, Cu atoms with $< Cu_{3C}$ contribute to the extension of the VB edge

into the energy gap by ~ 0.7 eV through their Cu 3d states. On the contrary, Cu atoms with coordination number $> Cu_{3C}$, have Cu 3d and 4s states with lower energy. Secondly, Cu clusters induce the appearance of midgap states of two kinds: one state is due to the presence of a Cu-Ti bond, while the other is a Ti^{3+} polaron state generated by the localization of the charge coming from the copper on a Ti_{6C} atom right below the cluster. Besides, the Ti^{3+} ions observed in correspondence of oxygen vacancies (V_O-Ti^{3+} sites) (Berger et al., 2005), the copper-induced Ti^{3+} contributes to increased photoabsorption, hence enhanced photocatalytic activity. Indeed, it is well known that polarons easily migrate to the surface in titania, and that electrons from Ti^{3+} sites are involved in dissociative electron attachment of CO_2 even in the dark (Liu and Li, 2014).

Its further noted that the electronic structure of the system with a Cu_4 cluster is different from those with smaller (Cu_{1-3}) clusters. The Cu_4 cluster has an empty state at the bottom of the conduction band (CB) and this state becomes full when an additional electron is added to the system. This behaviour is in agreement with the expectation that photoexcited electrons are transferred from titania to metal clusters at the surface. On the contrary, in clusters with less than four atoms, the empty states are well above the bottom of the CB, and therefore, it seems probable that photoexcited electrons will not be transferred to the cluster. Based on this result, oxidized copper clusters were built from Cu_4 cluster. This is further supported by another DFT calculation, which found Cu_4 clusters to posses a low activation barrier for conversion of CO_2 to methane (Liu et al., 2015a).

As mentioned earlier, Cu NPs are suitable alternatives to noble metals for catalytic HER. The Cu-TiO_2 system is shown in Figure 2.6 (Gawande et al., 2016). The Fermi level of metallic Cu lies well below the conduction band of TiO_2, hence photogenerated electrons in TiO_2 can be easily transferred to the Cu NPs. The interfacial electron transfer provides an increase in the separation of photogenerated electron-hole pairs, thereby resulting in an enhanced photocatalytic activity.

In 2004, Wu et al. showed that Cu NPs prepared by wet impregnation followed by low-temperature H_2 reduction could improve the catalytic activity of TiO_2 (Wu and Lee, 2004). The HER catalytic activity of Cu-TiO_2 is about 10 times higher than that of pristine TiO_2 at the optimum loading amount of 1.2 wt % Cu. Another study by Foo et al. reported the spontaneous oxidation of Cu NPs by O_2 under an atmosphere of air, providing credible

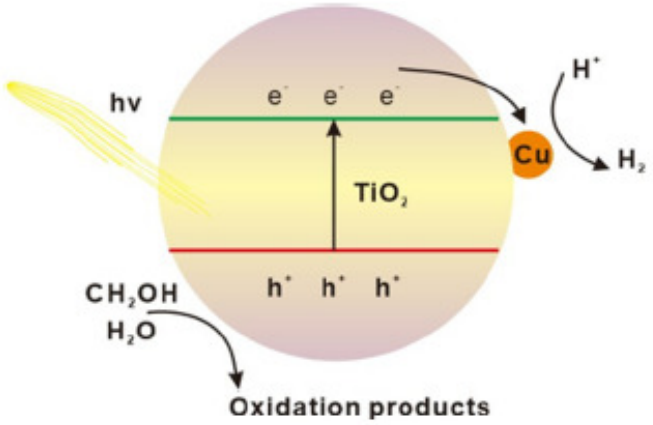

Figure 2.6: Mechanism of HER photocatalysis by Cu NPs supported on TiO_2 NPs (Gawande et al., 2016).

evidence for the formation of thin Cu_2O shells surrounding the Cu NPs (Foo et al., 2013). Recently, ion-exchange (Tian et al., 2014) and electroless plating (Wang et al., 2014b) methods have been developed by two different groups to prepare highly active Cu NP-modified TiO_2 photocatalysts for HER; the resulting materials exhibited greater catalytic activity than a Cu-TiO_2 sample prepared via the wet impregnation method. This finding was attributed to the ability of the ion-exchange and electroless plating methods to produce highly catalytically active Cu NPs with smaller particle sizes and greater dispersion over the TiO_2 surface.

2.4.3 Cu_2O/TiO_2 photocatalytic system

Cu_2O NPs have been used as sensitizers to extend the light response range of wide-band-gap semiconductors such as TiO_2 and provide the latter with visible light catalytic activity. The potential applications of such materials (e.g., Cu_2O-modified TiO_2 NPs and nanotubes) as catalysts for hydrogen evolution from water under sacrificial conditions have been successfully demonstrated (Li et al., 2012; Lalitha et al., 2010; Senevirathna et al., 2005). The sensitization mechanism of Cu_2O (Wang et al., 2013) involves the generation of electron-hole pairs on Cu_2O upon visible light irradiation. Because the conduction band of TiO_2 is positioned below that of Cu_2O, photoexcited electrons in the conduction band of Cu_2O will transfer to the conduction band of TiO_2 through the Cu_2O-TiO_2 interface. Once in the conduction band of TiO_2 , these electrons can efficiently participate in the hydrogen evolution reaction. For example, the proposed reaction mechanism for more efficient H_2 production

under solar irradiation using ethylene glycol as hole scavenger and $Cu_{1.5}$ TNT photocatalyst is shown in Fig. 2.7 (Kumar et al., 2016). Excitation of narrow band gap semiconductor Cu_2O in $Cu_{1.5}/TiO_2$ photocatalyst under the visible light generates electron–hole pairs at conduction band (CB) and valence band (VB), respectively. These electrons are scavenged by Cu^0 metal which is surface-interacted with TiO_2 nanostructures, followed by reduction reaction with protons to produce molecular hydrogen gas. This mechanism is in good agreement with earlier reported works (Yu and Ran, 2011). Sacrificial agents (water/ethylene glycol or its intermediates) are consumed by photogenerated holes in the VB of Cu_2O and TiO_2 which results in generation of oxygen and carbon dioxide.

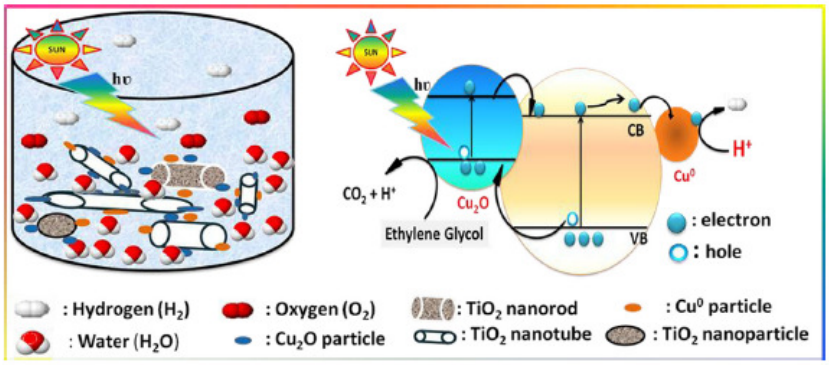

Figure 2.7: H_2 production using $Cu_{1.5}/TiO_2$ catalyst under solar irradiation (Kumar et al., 2016).

Kumar et al. investigated materials comprised of nanotubes, nanorods and particles whose surfaces are modified by a fine dispersion of Cu_xO clusters (Cu^0 and Cu_2O) (Kumar et al., 2016). The presence of Cu_xO at the surface extends the absorption from the UV to the visible light range. The Cu_xO/TiO_2 nanostructures exhibit a prolonged life-time of photogenerated charge carriers compared to pure and calcinated TiO_2, hence a higher rate of H_2 production, about 33 and 18 fold as compared to the pristine and calcinated TiO_2 nanoparticles (Kumar et al., 2016). The unprecedented H_2 production is attributed to synergistic effects of nanocrystalline structures, morphology and copper oxide species (Cu^0 and Cu^{2+}) present in the photocatalyst. Moreover, Cu_xO/TiO_2 demonstrated reproducibility and recyclability of the catalyst for at least 3 cycles without any significant loss in its activity.

Lalitha and co-workers also reported (Lalitha et al., 2010) that finely dispersed Cu_2O on commercial TiO_2 (P-25) showed an enhanced photocatalytic H_2 production under solar

light irradiation. Size-dependent photocatalytic activity of Cu_2O nanocrystals on TiO_2 (P-25) catalysts under the simulated solar irradiation was also reported by Li et al. (Li and Li, 2001). The amount of copper and the temperature of calcination greatly influenced the nature of copper species in the nanostructured catalyst (Cu_xO/TiO_2), which showed an improved activity for the H_2 production as described by Jung et al. (Jung et al., 2014).

Li et al. prepared Cu_2O/TiO_2 photocatalysts with different molar fraction of Cu_2O by a facile modified ethanol-induced approach followed by a calcination process (Li et al., 2015b). The results indicated that the photocatalytic activity of n-type TiO_2 was significantly enhanced, when combined with p-type Cu_2O, due to the efficient p-n heterojunction. The p-n heterojunction between Cu_2O and TiO_2 can enhance visible-light adsorption, efficiently suppress charge recombination, improve interfacial charge transfer, and especially provide plentiful reaction active sites on the surface of the photocatalyst. As a consequence, the prepared 2.5-Cu_2O/TiO_2 photocatalyst by Li et al. exhibited the highest photocatalytic activity for H_2 evolution rate and was $\sim$ 15 times larger than that of pure TiO_2.

Huang et al. synthesized Cu_2O/TiO_2 nano-heterostructures with different concentrations of Cu_2O by an alcohol-aqueous based chemical precipitation method (Huang et al., 2009). The prepared Cu_2O/TiO_2 heterostructures with the Cu_2O concentrations of 30 % and 70 % recorded the best photocatalytic efficiencies, which are 6 times and 27 times higher than that of pure titania (P25) under UV-vis light and visible light irradiation.

Xiong et al. performed photocatalytic experiment under visible light to shed more light on how photogenerated electrons are transferred and trapped in Cu_2O/TiO_2 (Xiong et al., 2011). It was reported that Cu_2O/TiO_2 was more efficient in HER than TiO_2 and Cu_2O alone. It was proposed that photogenerated electrons from CB of Cu_2O are captured by Ti^{4+} ions in TiO_2 and Ti^{4+} ions are further reduced to Ti^{3+} ions. The electrons are then stored in Ti^{3+} ions as a form of energy. These electrons trapped in Ti^{3+} can be released if a suitable electron acceptor is available and can be transferred to the interface between Cu_2O/TiO_2 and the solution to participate in photocatalytic reaction (see Fig. 2.8).

Liu et al. prepared Cu_2O nanospheres decorated with TiO_2 nanoislands by a facile hydrolyzation reaction followed by a solvent-thermal process (Liu et al., 2014). In Cu_2O/TiO_2 photocatalyst, Cu_2O served as the main visible light absorber, while TiO_2 nanoislands formed heterojunctions of good contact with Cu_2O for an efficient charge carrier separa-

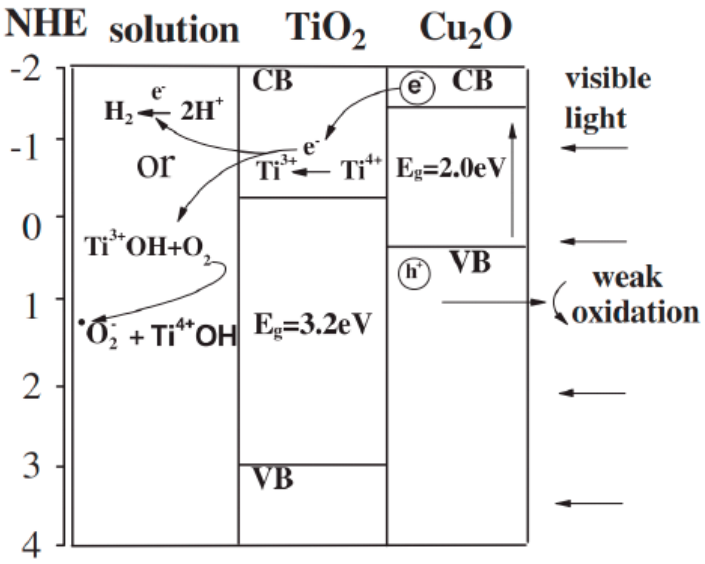

Figure 2.8: Mechanism of electron transfer in Cu_2O/TiO_2 in the presence of Ti^{3+} ions (Xiong et al., 2011).

tion and a subsequent increase of the lifetime of the charge carriers. The composite catalyst possessed a better stability during the photocatalytic process compared to pure Cu_2O nanosphere. Some photoexcited electrons transferred from Cu_2O to TiO_2 were trapped by TiO_2 nanoislands under visible light illumination and then released in the dark, which could give a catalytic memory to this photocatalyst for producing radicals without light illumination.

Sinatra et al. studied photo-catalytic hydrogen production from water over colloidally fabricated catalysts composed of Au/Cu_2O deposited on TiO_2 (anatase) (Sinatra et al., 2015). The Au-Cu_2O composite is in the form of $\sim$ 10 nm Au nanoparticles grown on $\sim$ 475 nm Cu_2O octahedral nanocrystals with (1 1 1) facets by partial galvanic replacement. The rate for hydrogen production over Au-Cu_2O(2 wt.%)-TiO_2 is found to be slightly better than Cu_2O(2 wt.%)-TiO_2, 10 times faster than Au(2 wt.%)-TiO_2 and almost 30 times faster compared to TiO_2 alone. Characterization of the catalyst before and after photoreaction rate suggests in situ reduction from Cu^+ to Cu^0 occurs upon photo-excitation (see Figure 2.9 for proposed reduction mechanism). The stable rate despite reduction to Cu^0 indicates that the latter takes part in the reaction by providing additional sites for the reaction, most likely as recombination centers for hydrogen atoms to form molecular hydrogen. Moreover, the absorption spectrum is extended to visible range. This system exploits both the plasmon resonance effect (Au nanoparticles) and the pn-junction at the Cu_2O-TiO_2 interface. Al-

though, the cost of noble metal Au is prohibitive, this synergistic effect provides alternative route for enhancing the efficiency and lifetime of Cu_2O-TiO_2 photocatalytic systems.

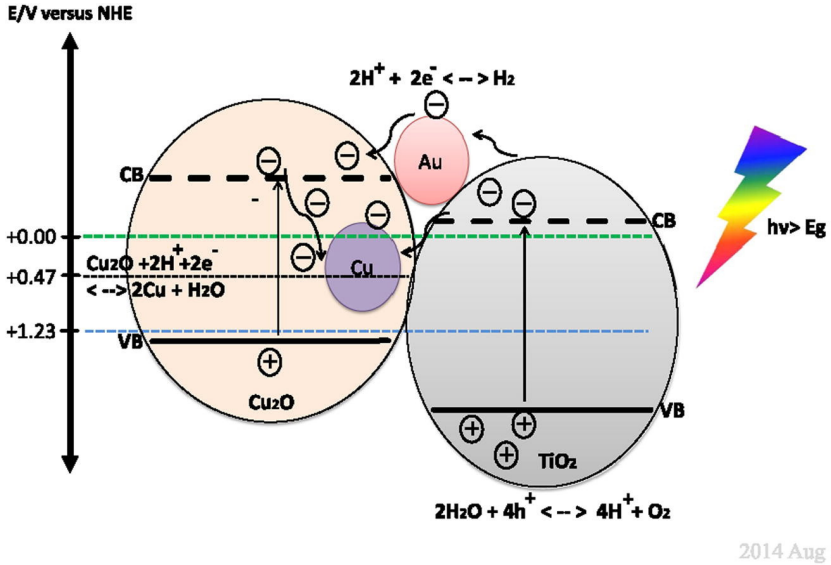

Figure 2.9: Energy band position of Cu_2O and TiO_2 aligned with redox potential of water (Sinatra et al., 2015).

Wang et al. have shown that Cu_2O is the active species for TiO_2 surface modification for H_2 production (Wang et al., 2013). In a similar study, electrodeposited Cu_2O on TiO_2 has been shown to split water (Yasomanee and Bandara, 2008). Predominantly, Cu_2O has been reported as the active species in reducing electron-hole pair recombination and as an active site for multi-electron transfers. Wang et al. have shown that Cu-TiO_2 nanomaterials, produced by the reaction of Cu(I) salts, photoreduced to Cu(0) and re-oxidised in ambient conditions, can work as stable photocatalysts if the formation of the CuO is avoided (Wang et al., 2016). Theoretical investigations have shown that the presence of low co-ordinated Cu on the surface can induce a shift in the valence band edge mainly via the sub-band gap states of Cu 3d (Jin et al., 2013). Additionally, the formation of Cu-Ti bonds and Ti^{3+} can influence the electrical properties of the material through these mid-gap states inducing alternative conduction paths. These mid bandgap states might enhance the photocatalytic activity of TiO_2 by absorbing photons and/or enhancing electron-hole pair separation (Seriani et al., 2015).

2.4.4 CuO/TiO_2 photocatalytic system

TiO_2 is one of the most widely studied semiconductor materials and its activity can be greatly enhanced by coupling with CuO NPs/clusters. This effect is partly attributable to the formation of favourable reaction sites for catalysis at the interfaces of the two semiconductor materials. In the case of CuO-TiO_2 composite semiconductor materials, there is a contact electric field at the heterojunction interface, which facilitates the water splitting process. Since the conduction band (CB) of CuO is situated below that of TiO_2, photogenerated electrons in the CB of TiO_2 can be driven by the contact electric field to the CB of CuO, thus leading to efficient separation of photogenerated electron-hole pairs and improvement of catalytic activity (see Fig. 2.10a) (Yu et al., 2011).

It is worthy noting that bulk CuO itself does not have the ability to catalyze the splitting of water to generate hydrogen because the CB edge of CuO is lower than the H^+/H_2 potential. In contrast, the CB edge of CuO clusters is higher than that of bulk CuO and the H^+/H_2 potential due to the quantum confinement effect (see Figure 2.10b). This explains why nanostructured CuO clusters are generally more effective at improving TiO_2's catalytic activity. Once the photogenerated electrons are transferred to CuO from TiO_2, the Fermi level of CuO will be raised and its CB potential will become more negative due to the accumulation of excess electrons (Bandara et al., 2005). This negative movement of CuO's CB potential is also beneficial for the reaction of photogenerated electrons with protons to produce H_2. For example, Xu et al. prepared CuO-modified TiO_2 NPs by the wet impregnation method, that yielded a substantial hydrogen evolution rate of 18.5 mmol/h/$g_{catalyst}$ from a methanol/water solution (Xu and Sun, 2009). This group also demonstrated that CuO-modified TiO_2 nanotubes exhibited enhanced HER catalytic activity, with a hydrogen evolution rate of 64.2-71.6 mmol/h/$g_{catalyst}$ (Xu et al., 2011). This was mainly ascribed to the unique one dimensional tubular structure and large surface area of the TiO_2 nanotubes relative to TiO_2 NPs. Jin et al. reported an eosin-sensitized CuO-TiO_2 photocatalytic system that is efficient for HER under visible light (> 420 nm) irradiation with an apparent quantum yield of 5.1 %.

Irie et al. investigated the role of Cu(II) ions in the Cu(II)-grafted TiO_2 photocatalyst (Irie et al., 2009). Their results indicated that distorted CuO formed clusters and attached

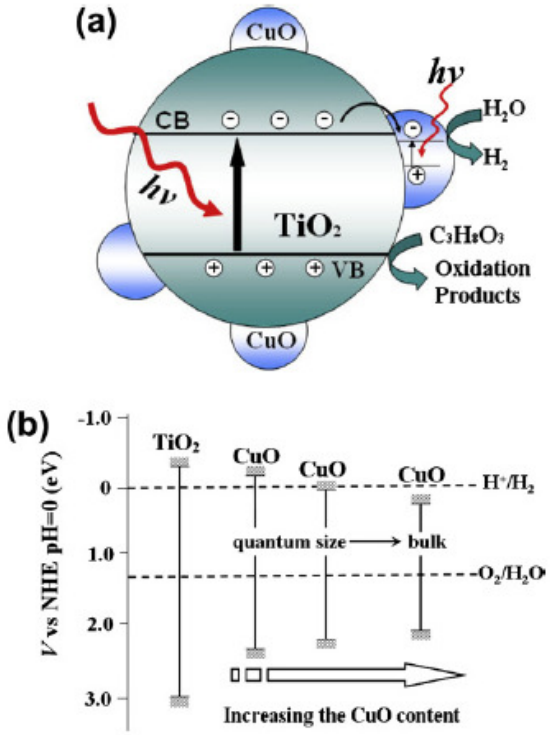

Figure 2.10: (a) Charge transfer and separation in CuO-TiO_2 under UV light. (b) Energy levels of the conduction and valence band edges vs normal hydrogen electrode (NHE at pH 0) for TiO_2 and CuO with various size (the quantum size effect is reflected by the band gap increase) (Yu et al., 2011).

to the TiO_2, the Cu (II) ions were unchanged after photocatalytic oxidation, hence the photocatalyst was stable. Li et al. (Li et al., 2008) studied coupled CuO-TiO_2 photocatalyst prepared by a deposition precipitation method and were characterized with a variety of techniques. It was noted that highly dispersed CuO clusters and substitutional Cu^{2+} (Ti-O-Cu linkages) sites at 0.1 wt % copper loading were present in the catalyst with enhanced activity. Besides, TiO_2 should be doped with small quantities of CuO, since higher loading creates recombination centres that lowers photoactivity.

Slamet et al. investigated photocatalytic reduction of CO_2 by copper-doped titania catalysts with various copper species (Cu^0 , Cu^+, Cu^{2+}) prepared by an improved-impregnation method (Slamet et al., 2005). It is reported that CuO is the dopant species that played the greatest role in enhanced CO_2 photoreduction over TiO_2 matrix, hence Cu^{2+} was the most active species. Bandara et al. (Bandara et al., 2005) studied and found a CuO incorporated TiO_2 catalyst to be an active photocatalyst for the reduction of H_2O under sacrificial conditions. The TiO_2 act as the primary catalyst and CuO acts as the co-catalyst. Pure CuO was found to be an inactive catalyst for water reduction process. However, in CuO/TiO_2

catalyst, CuO acts as the water reduction site. Higher catalytic activity and stability of CuO/TiO_2 arise from efficient interparticle charge transfer process.

Some recent studies of CuO-photocatalyst for hydrogen production from water with methanol as sacrificial agent have been reported (Teng et al., 2014; Xu et al., 2011; Hou et al., 2016b; Yu et al., 2015). It should be commented that, the p-n heterojunction formed at the interface between CuO-TiO_2 enhances charge separation, hence decreases recombination of photogenerated charge carriers. In addition, enhanced catalytic activity of CuO-deposited TiO_2 rod (Yu et al., 2015) is attributed to effects of high surface area, engineered band energy structure, and enhanced light harvesting at the interface of CuO and porous TiO_2 rods.

de Brito et. al investigated the role of CuO nanoparticles decorating TiO_2 nanotubes (TNT) thin film photoanodes in compact photo-electrocatalytic solar cell for water splitting reaction (de Brito et al., 2018). This cell is characterized by the photoanode and the cathode separated by a Nafion thin proton membrane (see Fig. 2.11). In this type of cell, the photogenerated electron and hole pairs at the photoanode, are transported in the thin film to the bottom of the TNT film supported over microholed Ti thin layer acting as an electron collector. The protons pass through the Nafion membrane and reach the cathode (Pt NPs supported on GDL), where they react with electrons transported through the external wire to generate H_2. The electrolytes in the anode and cathode compartments are 1.0 mol L^{-1} NaOH and 0.5 mol L^{-1} H_2SO_4, respectively.

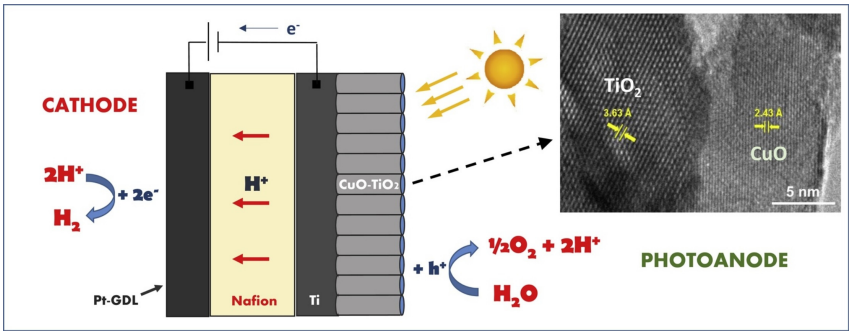

Figure 2.11: CuO NPs-TNT Photoelectrochemical cell (de Brito et al., 2018).

de Brito et al. noted that presence of CuO NPs in the internal walls of TNT improved: photocurrent behaviour, hydrogen generation rate by water splitting in a full PEC device (without external bias) and the solar-to-hydrogen efficiency with enhanced performances of about 20 % and 50 % in open spectrum and AM 1.5G filtered light from solar light, respectively. The increase in performance is mainly attributed to generation of a p-n junction

between Cu_xO nanoparticles and TNT upon illumination, which enhances photocurrent density by promoting charge separation.

Sharma et al. (Sharma et al., 2017) used DFT modelling and experiment to examine surface modification of TiO_2 with Cu oxide clusters. In their recent work, published later than our previous work (Meng'wa et al., 2017), Cu_4O_4 and $Cu_{10}O_{10}$ clusters were considered on anatase (101) and rutile (110) surfaces. DFT modelling predicts that small CuOx nanoclusters, regardless of Cu oxidation state bind strongly to rutile and anatase surfaces and can produce states within the band gap of TiO_2 potentially narrowing the effective band gap and inducing a red shift in the photoaction spectrum. It is also reported that sub-nanometre clusters of copper maintained their size and morphology upon attachment to the TiO_2 surface. The copper clusters were determined to be a mixture of Cu(0) and Cu(I), and no significant change in the oxidation state was observed following surface modification or photoelectrochemical measurements.

2.5 Copper- plasmonic photocatalysis

Cu NPs can activate TiO_2 towards visible light absorption due to localized plasmon surface resonance (LPSR) of Cu, thus plasmonic photocatalyst. The LSPR is excited when light interacts with free electrons of metallic nanostructure, which results in the collective oscillations that lead to improvement of the local electromagnetic fields around the nanoparticles (Chan et al., 2007). Metallic nanoparticles, such as gold, silver and copper, are very small (in comparison with the wavelength of the light) to be resonant with the light coming from all directions and indicate coloration as well as a local electromagnetic field enhancement on the particle surface even without the condition of total internal reflection (Ueno and Misawa, 2013). The existence of surface plasmon resonance band absorbing light in the visible region results in visible-light activity of noble metal-modified titania, maybe due to an efficient transfer of the photoexcited electrons from metal particles to the conduction band of TiO_2. Other proposed mechanisms of improved visible light response are energy transfer and plasmonic heating. This would result in electron depletion in metal and electron-richness in TiO_2 and hence, photocatalytic oxidation occurs on the metal surface rather than on TiO_2 surface.

Several LSPR studies are focused mainly on Au and Ag as plasmonic metals, which improve photocatalytic properties of TiO_2 (Hou and Cronin, 2013). However, very few investigations are available on photocatalytic performance of Cu NPs/titania (Yamaguchi et al., 2012; Zhang et al., 2015; DeSario et al., 2017). The main issue concerning Cu NPs as a LSPR sensitizer is the known fact that Cu^0 is easily oxidized to CuO/TiO_2 or $Cu/Cu_2O/TiO_2$ and loose plasmon resonance properties gradually under ambient conditions (Kanninen et al., 2008; Pastoriza-Santos et al., 2009; Singh et al., 2010). Furthermore, Cu NPs immersed in water are easily oxidized by dissolved oxygen (Muniz-Miranda et al., 2013). The solution to this problem lies in preventing oxidation of copper.

Many studies on Cu NPs-TiO_2 are connected with unprotected Cu under reductive, oxygen free conditions. Zhang et al. prepared TiO_2 nanotube embedded with copper NPs by pulsed electrochemical deposition method (Zhang et al., 2015). The authors reported visible light activity of this material for hydrogen evolution. Similarly, Kum et al. studied the properties of the visible light active Cu/TiO_2 photocatalyst for hydrogen production (Kum et al., 2015). This material showed high stability and photocatalytic activity in the vacuum. However, it is difficult to determine whether the photocatalyst was activated by excitation of Cu LSPR or band gap heterojunction with copper oxides since photocatalysis experiments were driven by visible light irradiation.

In order to apply copper-TiO_2 system in oxidative environment, retention of zero-valent nature of metallic copper is paramount. Yamaguchi et al. prepared plasmonic Cu NPs on TiO_2 electrode and coated with polyvinyl alcohol, which resulted to improved photocurrent due to LSPR (Yamaguchi et al., 2012). De Sario et al. found that plasmonic properties of Cu nanoparticles are preserved by an extended interfacial contact with reduced TiO_2 support (DeSario et al., 2017).

2.6 Water Adsorption on Titanium and Copper oxide surfaces

In heterogeneous catalysis, adsorption of water is usually the first step. There are extensive experimental and theoretical studies dedicated to understanding the adsorption of water on anatase TiO_2 (101) surface (Vittadini et al., 1998; Herman et al., 2003; Sun et al., 2010; Zhao et al., 2011). It has been widely reported that molecular adsorption of water

on TiO_2 anatase (101) surface is the most favourable. However, recent experimental and DFT investigations (Walle et al., 2011; Patrick and Giustino, 2014) at monolayer coverage, have reported co-existence of mixed molecular and dissociated water adsorbed groups. The energetics of water dissociation are made possible when two H_2O molecules are adsorbed nearer each other.

DFT theoretical works of water adsorption on the most stable copper oxide surfaces have been reported. On stoichiometric Cu_2O (111) surface, H_2O molecular adsorption is more preferred at Cu_{CUS} (coordinately unsaturated Cu site) (Zhang et al., 2013) with E_{ads} for the most stable adsorption configuration being equal to 0.82 eV. Similarly, for Cu_2O(110):CuO, which is the most stable surface under O-rich conditions, molecular water adsorption has been found to be more favourable due to anticipated high activation barriers of water dissociation on this surface (Saraireh and Altarawneh, 2013). For perfect CuO (111) surface, the adsorption strength of molecular water is substantially weaker than that of dissociated water species. The preferred molecular adsorption site on this surface is Cu_{SUB} (subsurface copper site) with an adsorption energy of about 0.9 eV (Zhang et al., 2016).

Andersson, Klas, et al. (Andersson et al., 2005) performed experiments to answer the question whether H_2O adsorption on Cu (110) surface (thermodynamically most stable Cu surface) is intact (molecular) or dissociated into OH and H species. The authors observed intact adsorption of water on clean Cu (110) at low temperatures (< 150 K) and partial dissociation at higher temperatures (> 150 K). Therefore, at room temperature conditions partial dissociative adsorption is more favorable with an activation barrier of between 0.53-0.9 eV, which is dependent on the coverage (Chen et al., 2010a). Chen et al. (Chen et al., 2010a) used DFT to calculate a value of 0.42 eV for molecular adsorption energy of water on small copper clusters. This value is much smaller compared to the adsorption energies of water on stable Cu_2O and CuO surfaces and different from other transition metal systems which was attributed to the fact that copper is less reactive than other transition metals because the d-orbitals are fully filled.

2.7 Photoelectrochemical Water Splitting

Hydrogen, H_2, has the potential to meet the requirements as a clean non-fossil fuel , if it can be produced using the world's most abundant energy source, the sun, and stored and transported safely (Currao, 2007). The search for an efficient system for solar energy conversion and storage is one of the challenging subjects to solve the global energy problem.

The world primary energy consumption in 2013 was 17 TW. By contrast, the consumable solar energy is approximately 120,000 TW. These values indicate that only 1 h of solar irradiation is sufficient to cover the world's annual energy consumption. Currently, solar energy accounts for less than 2 % world's energy demand.

In order to match energy consumption and rapid increase in population, it is necessary to develop novel technologies for photochemical conversion and storage of solar energy. The attainment of a solar hydrogen economy requires solutions to key scientific and technical challenges. One major issue is the need to develop highly efficient photoactive materials capable of harvesting and converting solar energy into storable chemical energy, i.e. a clean non-fossil fuel like hydrogen. One possible route to achieve this, is photoelectrochemical (PEC) water splitting, which directly converts water to hydrogen and oxygen (Lipiński et al., 2013). Hydrogen could then be used directly in fuel cells, e.g. in vehicles, (Yoshida and Kojima, 2015) or could be used to produce hydrocarbons from carbon dioxide. In the overall reaction of photosynthesis:

$$6CO_2 + 6H_2O \rightarrow C_6H_{12}O_6 + 6O_2, \tag{2.4}$$

plants transform water and carbon dioxide in the presence of light into oxygen and carbohydrates. In effect then H_2O is split into O_2 and H_2, where the hydrogen is not in the gaseous form but bound by carbon. The aim of *artificial photosynthesis* is the light-driven splitting of water into H_2 and O_2:

$$2H_2O \rightarrow O_2 + 2H_2. \tag{2.5}$$

Water represents a plentiful energy resource, which, in a thermodynamically uphill reaction ($\Delta G \approx 237.2$ kJ/mol), is converted into a clean and storable fuel (H_2) with sunlight. The photoelectrochemical (PEC) path to water splitting involves separating the oxidation

(equation 2.6) and reduction (equation 2.7) processes into half-cell reactions.

$$\text{Oxidation} : 2H_2O \rightarrow O_2 + 4H^+ + 4e^-,$$
$$E^o = 1.23\ V\ vs.\ SHE. \tag{2.6}$$

$$\text{Reduction} : 2H^+ + 2e^- \rightarrow H_2,$$
$$E^o = 0.00\ V\ vs.\ SHE. \tag{2.7}$$

$$\text{Overall} : 2H_2O \rightarrow O_2 + 2H_2,$$
$$\Delta E^o = -1.23\ V\ vs.\ SHE. \tag{2.8}$$

The overall reaction (equation 2.8) and the corresponding negative ΔE^o with respect to SHE (standard hydrogen electrode) indicates that water splitting is not a thermodynamically spontaneous process. For the reaction to proceed an overpotential of 1.23 V must be overcome. For that purpose, materials are necessary which upon light absorption can drive the water splitting reaction. Semiconductor-based PEC water splitting into H_2 and O_2 using sunlight as the energy input has gained prominence. For efficient water splitting, the semiconductor photocatalyst must have an energy gap, that is < 3 eV to absorb visible light, which constitutes 42 % of the whole solar spectrum. Furthermore, the band edge potentials have to be suitable for water splitting and the semiconductor photocatalyst needs to be stable in the photocatalytic reactions. A semiconductor band-gap energy of atleast 1.23 eV is required to drive the water-splitting reaction according to equation 2.8.

Metal oxides are generally stable in aqueous solutions and are less expensive than non-oxide semiconductors. Unfortunately, the VB edges of most oxide semiconductors are determined by O 2p orbitals, which are located at ca. +3.0 eV or higher vs the normal hydrogen electrode (NHE) (Chen et al., 2010b). In order to reduce water to produce hydrogen, the CB edge of the semiconductor must be more negative than the water reduction potential, that

is 0 eV vs NHE. As a result, the bandgap of the metal oxide semiconductor will inevitably become larger than 3.0 eV (equivalent to a wavelength of 413.57 nm), rendering the material inactive in the visible light region. The band gap energies of different semiconductors with respect to redox potentials for water splitting are summarised in Figure 2.12 (Ong et al., 2016).

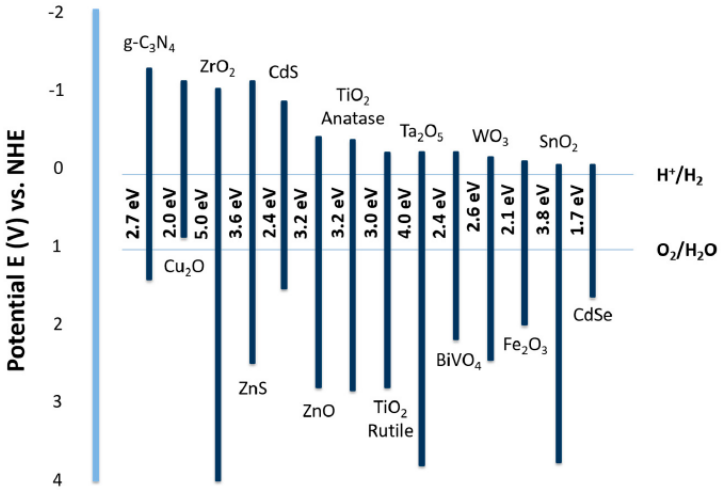

Figure 2.12: Band gap energies of various semiconductors with respect to NHE for water splitting (Ong et al., 2016).

2.8 Water Oxidation on clean TiO_2 (101) surface

The photoelectrolysis of water at the surface of semiconductor metal oxides has attracted much attention since the pioneering work on TiO_2 (Fujishima and Honda, 1972). This process provides hydrogen as a clean and sustainable carrier of solar energy. Most studies on photoelectrochemical cells, have a semiconductor photoanode and a metal cathode immersed in an electrolyte. In the PEC cell, water splitting is performed in two half-reactions; the oxygen evolution reaction (OER) taking place at the photoanode and the hydrogen evolution reaction (HER) taking place at the cathode. Unfortunately, the OER at the photoanode is responsible for the significant energy loss, mainly due to high overpotentials. This difficulty is also present for TiO_2, one of the most important photoanode materials for the OER.

As mentioned previously, intense research efforts have been devoted to reducing the OER overpotential on TiO_2, for instance by doping with various elements (Chen and Mao, 2007; Liu et al., 2013a; Asahi et al., 2001). However, it is still unclear how to design a photocatalyst with high OER activity, largely because of the limited understanding of the

chemical processes and kinetics involved in OER.

The mechanism of O_2 evolution on TiO_2 surfaces has been a subject of several studies. Wilson first identified the formation of oxidative species on a TiO_2 anode by electrochemical scanning (Wilson, 1980). Using the same technique, Salvador et al. suggested that Wilson's surface species may be attributed to adsorbed H_2O_2, produced by the coupling of surface OH radicals (Salvador and Gutierrez, 1984). It is often assumed that the reaction proceeds on a single active site, with four proton-coupled electron transfers (PCET), going through a nucleophilic attack with formation of adsorbed OOH intermediates (Di Valentin, 2016). Indeed, Nakamura et al. identified OOH and OO species under reaction conditions (Nakamura and Nakato, 2004; Nakamura et al., 2004), and proposed that they formed through nucleophilic attack of a water molecule on a surface-trapped hole at surface lattice oxygen. Altogether, it is generally agreed that the oxidation of water is initiated by the formation of surface-trapped photoholes. These holes (h^+) can oxidize water to O_2 through four sequential proton coupled electron transfer (PCET) steps. For example, Valdes et al. (Valdes et al., 2008) proposed the following most presumed PCET steps: (a) $H_2O + * \rightarrow HO* + H^+ + e^-$; (b) $HO* \rightarrow O* + H^+ + e^-$; (c) $H_2O + O* \rightarrow HOO* + H^+ + e^-$; (d) $HOO* \rightarrow O_2 + * + H^+ + e^-$, where * denotes active site on TiO_2 surface such as Ti_{5C} and X* is the adsorbed species.

2.8.1 Mechanism of OER

Density functional theory (DFT) calculations of the OER energetics have showed that the first proton coupled electron transfer (PCET) process, i.e. the hydroxyl formation, is the rate determining step on both rutile (Valdes et al., 2008) and anatase (Li et al., 2010) TiO_2. Li et al. investigated possible mechanism of OER on the three differently structured anatase surfaces: (101), (001) and (102) (Li et al., 2010). This study will however be focussed on the discussion of the most stable and dominant 101 surface. On anatase (101) surface, the OER proceeds by the direct splitting of H_2O on a Ti_{5c} site to produce an adsorbed OH group, H_2O adsorption on anatase (101) surface is thermodynamically unfavourable. The OH then loses a further proton, and the O (oxygen) adatom lean down to bond with an adjacent lattice O_{2C}, to form a surface-bridging O-O peroxo-like species. Next, a second H_2O molecule adsorbs at the surface Ti_{5C} near the O-O species, then decomposes to an

adsorbed OH by losing a proton, the bridging O-O species breaks one of its Ti-O bonds, turning into a terminal O_2. Upon further lose of a proton from the OH species, the terminal O can lean down to connect with surface O-O. Finally, O_2 desorbs from the surface with a very low reaction barrier (0.1 eV). In this OER path, there are no adsorbed OOH and HOOH species. It is further noted that under-coordinated surface Ti_{5C} are the OER sites, although the holes are trapped in the surface lattice O's. According to Li et at al., it is energetically unfavourable to initiate OER by a direct attack of H_2O molecule at a surface lattice O of TiO_2, as proposed by Nakamura and Nakato (Nakamura and Nakato, 2004).

Li et al. noted that removal of the first proton must overcome 0.69 eV even at an overpotential of 0.7 V, making cumulative overpotential to be 1.39 V. The presence of dopants in co-doped (Nb + N) and (Mo + C) anatase (101) surfaces was found to lower the surface free energies to 0.48 eV and 0.08 eV, respectively. The band gap of the doped system is greatly reduced, and as a result, the states appear above the VB of pure anatase. It is reported that, the Ti-OH bonding state is located below the maximum of VB of TiO_2, hence there is obvious net electron transfer from the TiO_2 surface to OH. However, such electron transfer is at the expense of the TiO_2 lattice bonding, since the TiO_2 surface is stoichiometric and oxidation of the surface is energetically unfavourable. In the presence of co-dopants, extra occupied states above the VB are introduced, which can enhance the electron transfer to the adsorbed OH group and thus facilitate the first proton removal step. In short, the high overpotential of OER can be attributed to the instability of the surface-adsorbed OH state after the first proton removal. By introducing occupied levels above the VB of pure TiO_2, the OER activity can be significantly enhanced.

2.8.2 Kinetics of OER

There is significant evidence that kinetic effects are also essential for the OER. On nc-TiO_2 photoanodes the required photohole lifetime for O_2 evolution is estimated to be $\sim$ 30 ms at pH 12.7 (Cowan et al., 2010) and $\sim$ 0.2 s at pH $\approx$ 6.5, (Tang et al., 2008). The faster rate of water oxidation at higher pH suggests a change in the water oxidation mechanism with pH. Similarly, photoluminescence (PL) measurements on rutile TiO_2 have shown that the PL intensity, which is proportional to the recombination rate of the photogenerated carriers, sharply decreases at pH values larger than $\sim$ 4 (Imanishi et al., 2007), indicating that the

OER rate increases at higher pH. These results cannot be explained on the basis of pure energetics. In fact theoretical analysis of the OER energetics show that the overpotential does not change with pH, (Valdes et al., 2008) thus suggesting that the enhanced activity at high pH could originate from kinetic effects.

Chen et al. (Chen et al., 2013) carried out a theoretical study of the first PCET step: $^*H_2O + h^+ \rightarrow {}^*OH + H^+$ to obtain the kinetics of the OER. As highlighted before, this step is considered the rate-determining step of the OER. Chen et al. performed FPMD and hybrid DFT calculations at the interface between anatase TiO_2 (101) and liquid water. On the basis of their results, the kinetics of the first OER-PCET step on TiO_2 can be understood as follows. The first PCET is sequential and initiated by proton transfer. At low pH, OH^- groups are scarce on the TiO_2 surface. Thus, proton transfer (PT) determines the rate of the reaction, with a moderate barrier of 0.2 to 0.5 eV. At higher pH values, the TiO_2 surface is covered by hydroxyl anions, and the overall PCET reaction rate does not depend on PT barrier. In this case, the PCET kinetics are determined by the barrier for the electron transfer (ET), which is significantly smaller than that of PT. As a result, the OER is faster at high pH, as indeed observed experimentally (Imanishi et al., 2007; Cowan and Durrant, 2013).

Chen et al. further suggested a strategy to increase the overall OER activity, by increasing the surface Lewis acidity, which facilitates first proton removal. They argued that anion doping, e.g. replacing oxygen with N, C, or S, should not change the rate of the first PCET significantly, as the Lewis acid site is always a surface Ti ion, that is the Ti_{5C} atom. For transition metal doping, however, the rate of the first PCET may change significantly, due to the different Lewis acidity of transition metal dopants substituting Ti_{5C} . This is consistent with experiments, thus showing significant changes of the OER overpotential on TiO_2 doped with different transition metals (Liu et al., 2013a).

Di Valentin (Di Valentin, 2016) used first-principles density functional study to investigate the interaction of a self-trapped hole at a bridging oxygen site on the anatase (101) TiO_2 surface with one water molecule. He observed a hole-induced water dissociation, resulting in an OH radical and a surface bridging OH species was observed. This process is proposed to be a concerted proton/hole transfer. It is noted that the hole transfer is from a surface bridging oxygen to the dissociating water molecule, whereas the concomitant proton

transfer is from the water molecule to a different surface bridging oxygen. On the basis of this mechanism, OH radicals are formed through the oxidation of water molecules and not as a result of hole trapping by surface OH. This means that the degree of surface hydroxylation is not a determinant for the formation of the OH radicals during the water photooxidation process. The formed surface OH radicals can easily interact with other water molecules at the interface and this triggers successive hole/proton transfers forming OH radicals in the liquid phase where they might pair into hydrogen peroxide molecules. If two OH radicals happen to meet, then the H_2O_2 formation is energetically favourable.

Li and Selloni (Li and Selloni, 2016) studied pathways and kinetics of the OER on the (101) anatase TiO_2 surface in water environment using hybrid DFT calculations and first-principles molecular dynamics (FPMD) simulations. They found that terminal Ti-OH groups are stable intermediates at the aqueous (101) interface, in accordance with the experimental finding that OH radicals are efficiently produced on anatase, unlike rutile (Kim et al., 2014). Oxidation of Ti-OH gives rise to a second stable intermediate, a surface-bridging peroxo dimer $(O_2^{2-})_{br}$ composed of one water molecule and one surface lattice oxygen atom, consistent with the surface peroxo intermediates observed on rutile (Nakamura and Nakato, 2004; Imanishi et al., 2007). Their calculations further predicted that molecular oxygen evolves directly from $(O_2^{2-})_{br}$ through a concerted two-electron transfer, thus leading to oxygen exchange between TiO_2 and the adsorbed species. This is in contrast to the sequential single-transfer pathway in rutile. The authors also found the nucleophilic attack (NA) mechanism proposed by Nakumara et al. (Nakamura and Nakato, 2004) for rutile to be energetically unfavorable on anatase (101). It is further argued that, the O (oxygen) source for O_2 molecule is largely determined by the geometry of the O* species, highlighting the important dependence of the OER pathway on the surface structure. The requirement of a concerted two-electron transfer, a process with low probability, on anatase may then be the reason for the lower OER activity of this polymorph with respect to rutile TiO_2 (Li et al., 2015a). Nevertheless, anatase is the major phase in nanocrystalline TiO_2 for particle sizes up to several nanometers, and that nanosized particles can expose much larger surface area (Li et al., 2010). Hence, anatase TiO_2 is of great interest for application in photocatalytic water splitting.

CHAPTER THREE

COMPUTATIONAL THEORY

3.1 Introduction

The properties of condensed matter and molecules are determined by the electrons and the nuclei. The study of electrons provides salient information about electronic, magnetic, optical and bulk properties of matter. Electronic structure calculations can be divided into ground state and excited state properties. For the ground state, features like the elastic properties, the charge density, equilibrium volumes and vibrational frequencies, may be obtained among many other interesting properties of matter. On the other hand, electronic excited states provide useful information about the optical properties. Various electronic structure methods have been developed in the past, but the most prominent method used for solid systems is Density Functional Theory (DFT) (Hohenberg and Kohn, 1964; Kohn and Sham, 1965). DFT is a reliable theory for predicting properties of new materials, to confirm experimental data, or to provide explanation of new phenomena observed in experimental work.

3.2 Many Body Problem

The non-relativistic time-independent Schrodinger equation for a system of N_e electrons and N_n nuclei, is written as

$$H\Psi = E\Psi, \tag{3.1}$$

where Ψ is the many-particle wavefunction, E is the total energy of the system and H is Hamiltonian. The many-particle wave function can either be symmetric or anti-symmetric. The symmetric case is expressed as

$$\Psi = \Psi(r_1.....r_N), \tag{3.2}$$

while the anti-symmetric case is given by

$$\Psi = \Psi(r_1...., r_i r_j ... r_N) = -\Psi(r_1...., r_i r_j ....., r_N). \tag{3.3}$$

The particles with half integer spins such as electrons are described by the anti symmetric wave functions and they obey the Pauli exclusion principle. Such particles are called fermions, while those particles whose wave functions are symmetric under particle interchange and have integral or zero intrinsic spin, are called bosons. The general Hamiltonian for the many body system is thus given by equation 3.4, as,

$$\hat{H} = \sum_i -\frac{\hbar^2}{2M_i}\nabla_i^2 + \frac{1}{2}\sum_{i,j}\frac{Z_i Z_j e^2}{|\mathbf{R}_i - \mathbf{R}_j|} - \sum_k \frac{\hbar^2}{2m_e}\nabla_{rk}^2 + \frac{1}{2}\sum_{k,l}\frac{e^2}{|\mathbf{r}_k - \mathbf{r}_l|} - \sum_{k,l}\frac{Ze^2}{|\mathbf{r}_k - \mathbf{R}_l|}. \tag{3.4}$$

where M_i is the mass of the nucleus at position R_i and R_j, m_e is the mass of an electron located at position r_k and r_l, Z is the atomic number of atoms forming the solid. Z_i and Z_j are the atomic numbers of the nucleus at position R_i and R_j. The first and third terms are the kinetic energies of the nuclei and electrons, respectively, while the second and fourth terms describe the nucleus-nucleus and electron-electron Coulomb repulsion, respectively. The fifth term describes the Coulomb attraction between the nuclei and electrons.

3.3 Hartree-Fock Approximation

The Hartree-Fock approximation was an improvement on Hartree approximation (Ostlund and Szabo, 1996) that failed to represent the way in which particular (as opposed to the average) configuration of the $(N-1)$ electrons affects an electron under consideration. The Hartree-Fock approximation is viewed as the basis or foundation for more accurate approximations involving correlation between electrons (Ostlund and Szabo, 1996). Within the Hartree-Fock approximation, the many body wave function of the system can be treated as a single Slater determinant of independent electrons which satisfies anti symmetry rule (Slater, 1951). Hartree-Fock theory provides an exact treatment of the exchange and correlation, which are useful for calculations involving molecules and larger N-body systems (Slater, 1951). Modification of the Hartree equation gives a Schrodinger-like equation with an effective Hamiltonian operator that depends on the state as shown by equation 3.5.

$$H_{eff}^i \Psi(r) = \left(-\frac{\hbar^2}{2m_e}\nabla^2 + V_{eff}^{i,\sigma}(r)\right)\Psi_i^\sigma(r) = E_i^\sigma \Psi_i^\sigma(r). \tag{3.5}$$

The effective potential $V_{eff}^{i,\sigma}(r)$ that acts on each electron of spin σ at point r is expressed as

$$V_{eff}^{i,\sigma}(r) = V_{ext}(r) + V_{Hartree}(r) + V_x^{i,\sigma}(r), \tag{3.6}$$

where V_{ext} is the external potential, $V_{Hartree}$ is the Hartree potential and $V_x^{i,\sigma}$ is exchange potential. The exchange term operator V_x is given by a sum over orbitals of the same spin as σ

$$V_x^{i,\sigma}(r) = -\sum_j \int dr' \Psi_j^{\sigma\star}(r') \Psi_i^{\sigma}(r') \frac{1}{|\mathbf{r} - \mathbf{r}'|} \frac{\Psi_j^{\sigma}(r)}{\Psi_i^{\sigma}(r)}. \tag{3.7}$$

The sum $\sum_i \Psi_j^{\sigma *}(r') \Psi_i^{\sigma}(r')$ is the Coulomb potential due to the exchange density for each state i, σ.

3.4 Density functional theory (DFT)

DFT was developed by Hohenberg, Kohn and Sham (Hohenberg and Kohn, 1964) and it gives very accurate description of the ground state properties of solids and molecules. DFT is based on the electronic density distribution n(r) rather than the many electron wave function Ψ (Kohn et al., 1996). In DFT an accurate ground state is crucial for the determination of equilibrium volume, bulk modulus, lattice constants and other properties of solids. DFT not only allows for the simulation of simple electronic properties, but it also allows for the treatment of quite complex materials properties such as determination of magnetic and electric susceptibilities, spin polarized ground states, and superconductivity (Kohn et al., 1996) among other properties. Besides, the determination of ground state properties using DFT, it allows one to describe the excited state properties to a certain extent, although this is well described by time dependent density functional theory (TDDFT) that employs adiabatic approximation together with PBE functionals used for the ground state. This is based on the fact that the ground state density of an electronic system uniquely determines external potential that the particles move in, which is associated with a specific Hamiltonian operator. This specific Hamiltonian operator fully describes the ground state as well as the excited states (Görling, 1996).

3.4.1 Hohenberg and Kohn formulation

Hohenberg and Kohn made the operation of DFT a reality (Hohenberg and Kohn, 1964), when they showed that the ground state electron density n(r), was sufficient to a good approximation to determine the many body total energy. They also showed that there existed a universal functional $F_{HK}[n(r)]$, such that for a given external potential $V(r)$, the actual ground state energy E and electron density n(r) was obtained by minimizing the energy functional:

$$E[n(r)] = F_{HK}[n(r)] + \int V(r)n(r)d^3r, \tag{3.8}$$

with respect to the variations in n(r) under the condition that the number of particles $N = \int n(r)(r)dr$ in the system remains constant.

3.4.2 Kohn Sham equations

Description of properties of solids from *ab-initio* calculation involves solving the Kohn-Sham equations, which are a general set of one particle equations. However, accurate and time efficient methods for solving these equations remains a big challenge. Pseudopotential methods which substitute the inert atomic cores by a pseudo potential, and orthogonalize a set of pseudo-valence states to these model cores (Wimmer et al., 1981; Kerker, 1980) is widely applied. Kohn and Sham (Kohn and Sham, 1965) derived their coupled set of differential equations to determine the ground-state density n_0(r) of a non-interacting system. The Kohn-Sham approach replaces the difficult many-body interacting system obeying Hamiltonian given by equation 3.4 with a different auxiliary system that can be solved more easily. The Kohn and Sham approach assumes that the ground state charge density of the original interacting system is equal to that of some chosen non-interacting system. This leads to independent-particle equations for the non-interacting system that can be considered exactly solvable with all the difficult many-body terms incorporated into an exchange-correlation functional of the density. By solving the equations, one finds the electronic ground state density and energy of original interacting system with accuracy limited only by the approximations in the exchange-correlation functional. The actual calculations are performed on the auxiliary independent-particle system defined by auxiliary Hamiltonian H^{σ}_{aux}(using

Hartree atomic units ($\hbar = m_e = 1$), that,

$$H^{\sigma}_{aux} = -\frac{1}{2}\nabla^2 + V^{\sigma}(r). \tag{3.9}$$

At this point the form of $V^{\sigma}(r)$ is not specified.

The density of the auxiliary system is given by the sum of squares of the orbitals of each spin:

$$n(r) = \sum_{\sigma}\sum_{i=1}^{N^{\sigma}} |(\Psi^{\sigma}_i(r)|^2, \tag{3.10}$$

while the independent particle energy T_s is given by,

$$T_s = \frac{1}{2}\sum_{\sigma}\sum_{i=1}^{N^{\sigma}} |\nabla\Psi^{\sigma}_i|^2. \tag{3.11}$$

The classical Coulomb interaction energy of electron density n(r) interacting with itself can be defined as per equation 3.12,

$$E_{Hartree}[n] = \frac{1}{2}\int d^3r d^3r' \frac{n(r)n(r')}{|\mathbf{r} - \mathbf{r}'|}. \tag{3.12}$$

The Kohn-Sham approach of the full interacting many-body problem involves the Hohenberg-Kohn expression for the ground state energy functional in the form,

$$E_{KS} = T_s[n(r)] + \int dr V_{ext}(r)n(r) + E_{Hartree}[n(r)] + E_{11}[n(r)] + E_{XC}[n]. \tag{3.13}$$

Here $V_{ext}(r)$ is the external potential due to the nuclei and any other external fields (assumed to be independent of spin) and E_{11} is the interaction between nuclei. Thus, the sum of the terms involving V_{ext}, $E_{Hartree}$ and E_{11} constitute the potential interactions in the Hamiltonian for the system of electrons and nuclei. The independent-particle kinetic energy T_s is given explicitly as a Functional of orbitals. However T_s for each spin σ must be a unique functional of the density $n(r, \sigma)$ by application of the Hohenberg-Kohn formalism applied to the independent-particle Hamiltonian. Equation 3.13 also defines the exchange-correlation functional E_{XC}. It is noted that all many-body effects of exchange and correlation are grouped into the exchange and correlation energy E_{XC}, which can be written in terms of

the Hohenberg-Kohn functional as

$$E_{XC}[n(r)] = \langle \hat{T} \rangle + T_s + \langle \hat{V}_{internal} \rangle - E_{Hartree}[n(r)], \tag{3.14}$$

where $\langle \hat{T} \rangle$ is the electron expectation value of kinetic energy operator $\hat{T}$. It is important to note that non-interacting electrons moving in an external potential $V_{eff}(r)$ are described by a ground state charge density

$$n_0(r) = \sum_{i=1}^{N} |\psi_{i,}(r)|^2. \tag{3.15}$$

The solution of the Kohn-Sham auxiliary system for the ground state can be viewed as the problem of minimization of total energy with respect to either the density $n(r, \sigma)$ or the effective potential V_{eff}^{σ}. From variational principle and the Lagrange multiplier method of handling constraints, this leads to the Kohn-Sham Schrodinger like equations of the form,

$$(H_{KS}^{\sigma} - \varepsilon_i^{\sigma})\Psi_i^{\sigma}(r) = 0, \tag{3.16}$$

where the ε_i^{σ} are the eigenvalues, and H_{KS}^{σ} is the Kohn-Sham effective Hamiltonian (in Hartree atomic units) which can be written as,

$$H_{KS}^{\sigma}(r) = -\frac{1}{2}\nabla^2 + V_{KS}^{\sigma}(r), \tag{3.17}$$

with

$$V_{KS}^{\sigma}(r) = V_{ext}(r) + \frac{\delta E_{Hartree}}{\delta n(r, \sigma)} + \frac{E_{XC}}{\delta n(r, \sigma)}, \tag{3.18}$$

or

$$V_{KS}^{\sigma}(r) = V_{ext}(r) + V_{Hartree}(r) + V_{XC}^{\sigma}(r). \tag{3.19}$$

This set of equations can be solved self-consistently. Equations 3.18 or 3.19 of a non-interacting reference system would lead to the exact ground-state density and energy for the interacting system, if the exchange energy functional $E_{XC}[n]$ were known. However, this functional is not known and hence the application of DFT requires the use of various approximate forms for the E_{XC} energy such as the local density approximation (LDA)

(Perdew and Zunger, 1981) and the generalized gradient approximation (GGA) (Perdew et al., 1996).

3.4.3 Local Density Approximation

Within the framework of the local density approximation (LDA) (Perdew and Zunger, 1981), the value of $E_{XC}[n(r)]$ is approximated by the exchange-correlation energy of an electron in a homogeneous electron gas of density n(r), so that,

$$E_{XC}^{LDA}[n(r)] = \int E_{XC}[n(r)]n(r)dr. \tag{3.20}$$

The LDA functional reproduces the ground state properties of many systems rather accurately. For example, Korir *et al* (Korir et al., 2011) showed that the bulk properties of group 4d transition metals were well described by LDA, as opposed to other approaches. However, there are situations whereby LDA fails due to the manner in which it treats the charge density. For example, LDA predicts the wrong magnetic structure of iron (Leung et al., 1991), while LDA also predicts inaccurately the band gap of semiconductor materials (Grüning et al., 2006). This therefore requires new methods to be used such as generalized gradient approximation.

3.4.4 Generalized Gradient Approximation (GGA)

For a long time, the local density approximation was considered the method of choice in electronic structure calculations. However, due to the failures already alluded to LDA, there was need to improve on it. One strategy to improve upon LDA was to include the gradient of the charge density in the exchange-correlation functional, something that should take into account the inhomogeneity of the electron gas. The resulting method, where the XC potential is a functional of both the charge density (at a given point), and the first-order gradient of the charge density (at the same point), is known as the generalized gradient approximation (GGA) (Perdew et al., 1998). The resulting energy $E_{XC}^{GGA}[r]$ is given by equation 3.21.

$$E_{XC}^{GGA}[n] = \int d^3r f(n, \nabla n). \tag{3.21}$$

$E_{XC}^{GGA}[n]$ is the exchange-correlation energy per particle of an electron gas. The GGA method gives better total energies, especially for small molecules, but computationally it is more time consuming than LDA due to the added features. Generally, GGA has the following advantages over LDA (Singh and Nordström, 2006):

1. GGA improves ground state properties for light atoms, molecules and clusters.

2. GGA predicts the correct magnetic properties of 3d transition metals such as body centred iron among others.

Although, GGA seems to be superior compared to LDA, it has several setbacks, which includes its failure to accurately treat the hydrogen bond. This defect is clearly manifested through expansion and hence softening of bonds (Proynov et al., 1995).

3.4.5 Pseudopotentials

Practical solutions to the self-consistent Kohm-Sham equations are subject to various approximations. Methods have been developed to reduce the computational cost (rapid convergence) without compromising the outcome of the calculations. The first-principle pseudopotential methods (Cohen and Heine, 1970) normally consider the valence electrons only, excluding the deep-inner core states and the strong potential that binds them to the nuclei. This makes the calculation less computationally expensive as compared to full-potential methods. Normally, the core electrons have minimal influence on the properties of solids, but their proper inclusion into the pseudopotentials creates room for the sufficient use of plane wave basis sets in electronic structure calculations (Rappe et al., 1990). There are several types of pseudopotentials: norm-conserving pseudo potentials (Hamann et al., 1979), ultra-soft pseudopotentials (Vanderbilt, 1990) and projector augmented wave (PAW) type of pseudopotentials (Kresse and Joubert, 1999). The PAW method is a unique method for determination of the electronic structure of materials since it describes well the nodal behaviour of the valence electron wave function, and it also allows for the inclusion of the upper core states into the self consistent iterations procedure.

3.5 K-point grid

The Monkhorst-Pack grid is a popular technique of sampling Brillouin zone. This method generates special points in the Brillouin zone, together with their integration weights which provide an efficient means of integrating periodic functions in the k-space (Monkhorst and Pack, 1976). The accuracy of integration entirely depends on the choice of the integration grid, and therefore the Monkhorst-Pack technique allows for specific integration of portions of the Brillouin zone only, but also for sampling of the entire Brillioun zone. However, the symmetry of the cell may drastically reduce the number of points within the Brillouin zone, thereby reducing computational cost of the system.

3.6 LDA+U (Hubbard Correction)

LDA and GGA miss important features of the physical behaviour of strongly correlated materials and high-T_c superconductors. For instance both local spin-density approximation (LSDA) and spin-polarized generalized gradient approximations ($\sigma-$GGA), fail to predict the insulating behaviour of many simple transition metal oxides (TMO), not only by severely underestimating their electronic band gap but, in most cases, producing a qualitatively wrong metallic ground state. The LDA+U approach, developed by Anisimov and coworkers (Anisimov et al., 1991; Anisimov et al., 1993; Solovyev et al., 1994), has been applied to study a large variety of strongly correlated compounds with considerable improvement with respect to LSDA or $\sigma-$GGA results. Anisimov et al. (Anisimov et al., 1991; Anisimov et al., 1993; Solovyev et al., 1994) corrected the standard functional by adding an on-site Hubbard-like interactions, E_{Hub}:

$$E_{LDA+U}[n(r)] = E_{LDA}[n(r)] + E_{Hub}[\{n_m^{I,\sigma}\}] - E_{dc}[\{n^{I,\sigma}\}], \tag{3.22}$$

where $n_m^{I,\sigma}$ are the atomic-orbital occupations for the atom I experiencing the "Hubbard" term and the last term is subtracted in order to avoid double counting of the interactions contained both in E_{Hub} and in E_{LDA}. When a rotational invariant formulation is introduced, the orbital dependence of E_{Hub} is borrowed from Hartree-Fock formalism, double counting term is evaluated as the mean field approximation of Hubbard one, while the exchange

interaction (J) is neglected (Cococcioni and De Gironcoli, 2005). We get:

$$E_U[\{n^{I,\sigma}_{mm'}\}] = \frac{U}{2}\sum Tr[n^{I,\sigma}(1-n^{I,\sigma})]. \tag{3.23}$$

where U is the Coulomb repulsion parameter on atomic site I (usually applied on the d states of a transition metal) and n^I are the occupation matrices. Equation 3.22 becomes:

$$E_{LDA+U} = E_{LDA}[\rho] + E_U[\{n^{I,\sigma}_{mm'}\}] = E_{LDA}[\rho] + \frac{U}{2}\sum_{I,\sigma} Tr[n^{I,\sigma}(1-n^{I,\sigma})], \tag{3.24}$$

because of rotational invariance, we can use a diagonal representation, with $0 \leq \lambda^{I,\sigma}_i \leq 1$, the energy correction becomes:

$$E_U[\{n^{I,\sigma}_{mm'}\}] = \frac{U}{2}\sum_{I,\sigma}\sum_i \lambda^{I,\sigma}_i(1-\lambda^{I,\sigma}_i), \tag{3.25}$$

from where it appears clearly that the energy corrections introduces a penalty, tuned by the value of the U parameter, for partial occupation of the localized orbitals and thus favours disproportionation in fully occupied ($\lambda \approx 1$) or completely empty ($\lambda \approx 0$) orbitals. This is the basic physical effect built in the DFT+U functional.

The exact DFT produces total energy with unphysical curvatures for noninteger occupation and spurious minima in correspondence of fractional occupation of the orbital of the atomic system. This behavior is not well described by LDA or GGA as depicted in Fig. 3.1 (Cococcioni and De Gironcoli, 2005). This leads to serious problems when one considers the dissociation limit of heteropolar molecules or an openshell atom in front of a metallic surface, (Perdew et al., 1982; Celli et al., 1984) and is at the heart of the LDA/GGA failure in the description of strongly correlated systems (Anisimov et al., 1991). To correct this situation, an approximately piecewise linear total energy curve is obtained by adding a correction to the LDA total energy which vanishes for integer number of electrons and eliminates the curvature of the LDA energy profile in every interval with fractional occupation (see bottom curve of Fig. 3.1). But this is exactly the kind of correction that is provided by equation 3.23, if the numerical value of the parameter U is set equal to the curvature of the LDA/GGA energy profile. Nevertheless, it is well known (Jones and Gunnarsson, 1989)

that total energy differences between different states can be reproduced quite accurately by the LDA or GGA approach, if the occupation of the orbitals is constrained to assume integer values. Therefore, the interaction parameter U can be defined as the (unphysical) curvature of the LDA energy as a function of N which is associated with the spurious self interaction of the fractional electron injected into the system. It depends not only on occupation matrices, but also the approximate exchange-correlation functional to be corrected, and should vanish if the exact DFT functional were used.

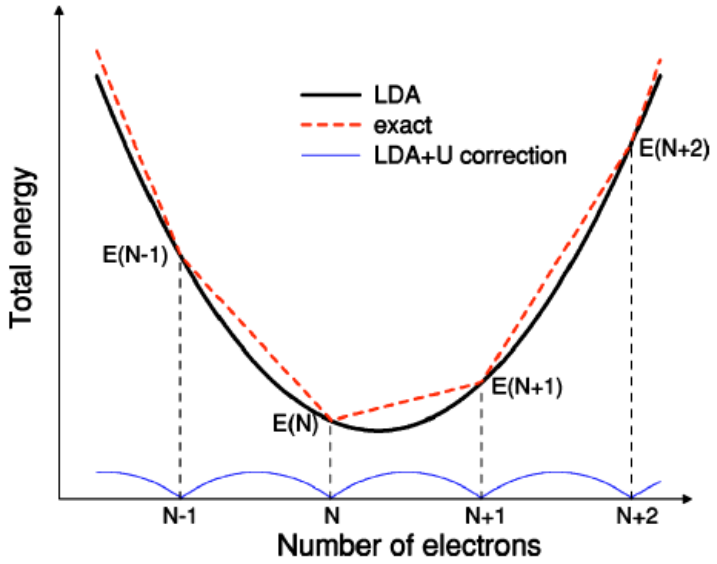

Figure 3.1: Sketch of total energy profile as a function of number of electrons in generic atomic system in contact with reservoir (Cococcioni et al., 2005).

3.7 First-Principles Atomistic Thermodynamics for Oxidation Catalysis

This section describes the thermodynamic formalism and how it is combined with DFT total-energy calculations based on theoretical scheme developed by Karsten Reuter and Matthias Scheffler (Reuter and Scheffler, 2001).

3.7.1 Introduction

Density-functional theory (DFT) is often argued to be a zero-temperature, zero-pressure technique. As such, the results of static total-energy calculations at surfaces have to be transferred with considerable care to typical high-pressure applications such as catalysis, a situation which finds its correspondence in the experiment in form of the ex situ methods of ultrahigh-vacuum (UHV) surface science.

Trying to bridge these gaps, one needs to determine the equilibrium composition and geometry of a surface in contact with a given environment at finite temperature and pressure. Under these conditions the stable surface structure is a result of the statistical average of adsorption and desorption processes, and hence an analysis based on thermodynamics must be employed. When one aims to describe experiments that are conducted at constant pressure and temperature, the appropriate thermodynamic potential to consider is the Gibbs free energy G(T,p). If DFT total energies enter in a suitable way into a calculation of G(T, p) for a material surface, ab initio thermodynamics is the result, and the predictive power of the first-principles technique is extended to a more relevant temperature and pressure range.

3.7.2 Surface free energy

As an illustration, one can consider a RuO_2 (110) surface in contact with an oxygen atmosphere described by an oxygen pressure (p) and temperature (T). This means that the environment acts as a reservoir, because it can give (or take) any amount of oxygen to (or from) the sample without changing the temperature or pressure. The appropriate thermodynamic potential required to describe such a system is the Gibbs free energy G(T, p, N_{Ru} ,N_O), which also depends on the number of Ru, (N_{Ru}) , and O, (N_O) ,atoms in the sample. The most stable surface composition and geometry is then the one that minimizes the surface free energy, γ (T,p), defined as

$$\gamma(T,P) = \frac{1}{A}[G(T,p,N_{Ru}) - N_{Ru}\mu_{Ru}(T,p) - N_O\mu_O(T,p)], \tag{3.26}$$

where μ_{Ru} and μ_O are the chemical potentials of a Ru atom and an O atom, respectively, and γ (T,p) is normalized energy per unit area by dividing through the surface area A. If the surface system is modeled by a slab with two equivalent surfaces, equation 3.26 becomes,

$$\gamma(T,P) = \frac{1}{2A}[G(T,p,N_{Ru}) - N_{Ru}\mu_{Ru}(T,p) - N_O\mu_O(T,p)], \tag{3.27}$$

here A is the area of the surface unit cell and N_{Ru} and N_O are numbers of Ru and O atoms in a three dimensional supercell, respectively.

3.7.3 Range of allowed O chemical potentials

In experimental procedures, it is the O_2 pressure and temperature which are varied, hence, it's more realistic to consider the dependence of the surface structure with respect to $\mu_O(T,p)$. It is important to note that experimentally, μ_O is varied within certain limits. If μ_O becomes too low, all oxygen would leave the sample, i.e., the oxide would decompose into solid Ru and oxygen gas. Thus,

$$max[\mu_{Ru}(T,p)] = g_{Ru}^{bulk}(T,p), \tag{3.28}$$

where $g_{Ru}^{bulk}(T,p)$ is the Gibbs free energy of metallic ruthenium. The Gibbs free energy of RuO_2 bulk oxide is given by,

$$g_{RuO_2}^{bulk}(T,p) = \mu_{Ru}(T,p) + 2\mu_O(T,p), \tag{3.29}$$

where g is Gibbs free energy per formular unit. From equation 3.29 and using T= 0 K and p= 0 atm limit for bulk energies, the oxygen poor limit (or equivalently "Ru-rich" environment) is expressed as:

$$min[\mu_O(T,p)] = \frac{1}{2}[g_{RuO_2}^{bulk}(0,0) - g_{Ru}^{bulk}(T,p)]. \tag{3.30}$$

This is a good estimate of the real physical limit and, most importantly, it is a theoretically well defined reference point on the μ_O axis. The most oxygen-rich conditions can be defined as the point beyond which gas phase O would start to condense on the sample. However, in the temperature and pressure range we are interested in, a condensed O_2-solid phase does not exist (the critical temperature of O_2 , i.e., above which gas and liquid phase are degenerate, is $T_c \approx 150K$). Thus, similar to equation 3.28, an appropriate and well-defined estimate of the upper limit of the oxygen chemical potential is

$$max[\mu_O(T,p)] = \frac{1}{2}E_{O_2}^{total}, \tag{3.31}$$

where $E_{O_2}^{total}$ is the total energy of a free, isolated O_2 molecule at T=0 K. Then, introducing the Gibbs free energy of an O_2 molecule, we see that the range of oxygen chemical potentials between our theoretical boundaries is

$$\frac{1}{2}\Delta G_f(0,0) < \mu_O(T,p) - \frac{1}{2}E_{O_2}^{total} < 0. \tag{3.32}$$

3.7.4 Gibbs free energies vs total energies

DFT total energies are evaluated for a certain volume V of the unit cell. The resulting $E^{total}(V, N_{Ru}, N_O)$ is related to a thermodynamical quantity only in a restricted way, corresponding to the Helmholtz free energy at zero temperature and neglecting zero-point vibrations. In general, the Helmholtz free energy can thus be written as

$$F(T, V, N_{Ru}, N_O) = E^{total}(V, N_{Ru}, N_O) + F^{vib.}(T, V, N_{Ru}, N_O), \tag{3.33}$$

with

$$F^{vib.}(T, V, N_{Ru}, N_O) = E^{vib.}(T, V, N_{Ru}, N_O) + TS^{vib.}(T, V, N_{Ru}, N_O), \tag{3.34}$$

comprising all contributions, which depend on vibrational modes in the system. Here $E^{vib.}$ and $S^{vib.}$ are the vibrational energy (including the zero-point energy) and entropy, respectively. In turn, the Helmholtz free energy is associated with the Gibbs free energy by

$$G(T, p, N_{Ru}, N_O) = F(T, p, N_{Ru}, N_O) + pV(T, p, N_{Ru}, N_O). \tag{3.35}$$

The contribution of pV term [$pV/A \sim 10^{-3} meV/\mathring{A}^2$] is negligible compared to the Helmoholtz free energy, which is in the order of tenths of $meV/\mathring{A}^2$. The only additional contribution to $G(T, p, N_{Ru}, N_O)$, apart from the DFT total energy, is the vibrational term $F^{vib.}(T, V, N_{Ru}, N_O)$. Using the phonon density of states (DOS) $\sigma(\omega)$, this vibrational component of the free energy can be written as an integral over the modes ω,

$$F^{vib.}(T, V, N_{Ru}, N_O) = \int d\omega F^{vib.}(T, \omega)\sigma(\omega). \tag{3.36}$$

3.7.5 Pressure and temperature dependance of $\mu_O(T, p)$

For an ideal gas of N particles at constant pressure p and temperature T, the chemical potential is given by the Gibbs free energy per atom:

$$\mu = \frac{\delta G}{\delta N}_{T,p,N} = \frac{G}{N}. \tag{3.37}$$

As the Gibbs free energy is a potential function depending on pressure and temperature, its total derivative is given as

$$\delta G = (\frac{\delta G}{\delta T})_p dT + (\frac{\delta G}{\delta p})_T dp = -SdT + Vdp, \tag{3.38}$$

Using the ideal gas equation of state, $pV = NkT$, the partial derivative of $G(T,p)$ with respect to pressure at constant temperature is consequently,

$$\frac{\delta G}{\delta p}_T = V = \frac{NkT}{p}. \tag{3.39}$$

In turn, a finite pressure change from p to p^o at constant temperature results in

$$G(T,p) - G(T,p^o) = \int_{p^o}^{p} (\frac{\delta G}{\delta p})_T dp = NkTln(\frac{p}{p^o}). \tag{3.40}$$

Combining equations 3.39 and 3.40, the chemical potential of O, can be written as,

$$\mu_O(T,p) = \mu_O(T,p^0) + \frac{1}{2}kTln(\frac{p}{p^0}), \tag{3.41}$$

which gives the temperature and pressure dependence, if only the temperature dependence of $\mu(T,p^0)$ is known at one particular pressure, p^0.

3.8 Free energies of the intermediates in a Fuel-cell electrode

This section is based on the formalism developed by Nørskov and co-workers(Nørskov et al., 2004). In this approach the free energy of all intermediates as a function of the electrode potential is determined directly from density functional theory calculations. For example, consider simple dissociation mechanisms:

$$\frac{1}{2}O_2 + (^*) \rightarrow O^*, \tag{3.42}$$

$$O^* + H^+ + e^- \rightarrow HO^*, \tag{3.43}$$

$$HO^* + H^+ + e^- \rightarrow H_2O+^*, \tag{3.44}$$

$$H_2O+^* \rightarrow HO^* + \frac{1}{2}H_2, \tag{3.45}$$

$$H_2O+^* \rightarrow O^* + H_2, \tag{3.46}$$

where H_2O and H_2 are in gas phase. The free energy of the intermediates of electrochemical reactions are theoretically modelled as follows:

1. When the reference potential is set to be that of standard hydrogen electrode (SHE), one can relate the chemical potential (the free energy per H) for the reaction $(H^+ + e^-)$ to that of $1/2H_2$ in equilibrium with $H_2 \rightarrow 2(H^+ + e-)$. This means that, at pH=0 in the electrolyte and 1 bar of H_2 in the gas phase at 298 K, the reaction free energies of eqns. 3.45 and 3.46 are equal to those of the reverse reactions eqns. 3.44 and 3.43 at an electrode potential of U= 0 relative to the SHE.

2. To model the water environment of the electrochemical cell, the effect of a monolayer of water on the stability of adsorbed O and OH is included in the calculation. For the low coverage results, water is simply added to fill the surface, while a bilayer of water is added on top of the adsorbed O and OH for the high coverage results. The interaction with water stabilizes OH groups on the surface relative to adsorbed oxygen due to hydrogen bonding. The effect of the water layer on adsorbed oxygen is negligible. This procedure can be improved by including more water in the calculation.

3. The effect of a bias voltage on all states involving an electron in the electrode is included, by shifting the energy of this state by -eU, where U is the electrode potential.

4. The adsorbed states also interact with the field set up outside the surface by the electrochemical double layer. The effect of the electrical field on the adsorption energy is negligible, ≈ 0.015 eV.

5. At a pH different from 0, the free energy of H^+ ions is corrected by the concentration dependence of the entropy: $G(pH) = -kTln[H^+] = kTln10 \times pH$.

6. The free energies of the intermediates at zero potential and pH=0 is calculated as $\Delta G = \Delta E_{w,water} + \Delta ZPE - T\Delta S$, where ΔE is the reaction energy of eqn. 3.45 or 3.46, ΔZPE is the difference in zero point energies due to the reaction, and ΔS is the change in entropy. These parameters are taken from DFT calculations or thermodynamic tables.

CHAPTER FOUR

COMPUTATIONAL METHODOLOGY

4.1 Introduction

The demand for materials for various applications such as renewable energy is the driving force behind the heightened research in material science in the 21st century. One of the cheapest and easiest ways to investigate materials is by first principle calculations. The idea behind first principles, also known as *ab-initio* calculation, is to apply the basic laws of physics to identify the composition of materials, under different thermodynamic conditions. This is achieved through computer simulations using different softwares such as Quantum Espresso, among many others.

Quantum ESPRESSO (Giannozzi et al., 2009) stands for opEnSource Package for Research in Electronic Structure, Simulation, and Optimization. It is an open source software, released under the GNU General Public License. The code is designed to perform density functional theory calculations and it uses plane wave basis sets and pseudopotentials in its applications. Its features range from the calculation of ground-state energy and Kohn-Sham orbital's to the calculation of atomic forces, stresses, and structural optimization, molecular dynamics on the ground state Born-Oppenheimer surface, Nudged Elastic Band (NEB) and Fourier String Method Dynamics. Quantum ESPRESSO is also able to perform other calculations such as phonon frequencies and eigenvectors at a generic wave vector, effective charges and dielectric tensors, electron-phonon interaction coefficients for metals, Infrared and Raman (non resonant) cross section, e.t.c.

In DFT, the code is able to simulate a wide range of materials including crystalline and nano crystalline solids, molecules and surfaces quite easily. In this work, calculations were done using parallel computing machines, owing to the flexibility of the code to run on different platforms, including simple stand-alone computers.

This study used plane wave self consistent calculations (PWSCF), which uses a plane-wave basis set to describe the ground state wave functions of the system where the number of plane waves needed to describe the system is determined by the kinetic energy cut-off. The more the number of plane waves, the more accurate is the calculation. However, this also

increases computation time, and hence computationally expensive. For periodic structures, it is often easier to describe the system in momentum or k-space. In this case, the region of available k-points for a system is known as the Brillouin zone. Many of the physical parameters associated with a system such as total energy, charge, magnetic moment etc. can be expressed in terms of the integration over k-points in the Brillouin zone. The k-point grid is usually expressed in terms of Monkhorst-Pack grid (Monkhorst and Pack, 1976), where the grids describe divisions in the k_x, k_y and k_z directions.

The geometry of the crystal structure determines many of its physical and chemical properties. This is why it becomes extremely essential that the lattice positions be optimized. The arrangement of atoms in the crystal and more specifically the electrons around the atom determine the energy level of that crystal. The objective of geometry optimization is to find the point at which the energy is at a minimum because this is where the crystal is most stable. Hence the geometry optimization is also referred to as the 'energy minimization'. It is therefore the purpose of geometry optimization to locate the minima based on some geometry for the crystal system. In this study all atoms were allowed to relax in x, y and z directions except for one Ti atom. Thereafter, the total energies and charge densities of the relaxed systems were obtained, and used to further compute properties of the materials.

4.2 Structural Optimization

Spin polarized calculations were carried out in the framework of density functional theory, as implemented in the Quantum-Espresso code, (Giannozzi et al., 2009) using a plane wave basis set. Vanderbilt ultrasoft pseudopotentials were used to describe core-valence interactions (Vanderbilt, 1990). The study employed DFT+U (Dudarev et al., 1998) with the GGA-PBE (Perdew et al., 1996) exchange-correlation functional and the Hubbard U correction in the version of Dudarev et al. (Dudarev et al., 1998). The values of U were taken from the literature: a value of 4.2 eV was used for titanium (Camellone et al., 2011; Seriani et al., 2015) and 5.2 eV for copper (Scanlon et al., 2009; Seriani et al., 2015). Kinetic energy cutoffs of 40 and 480 Ry were employed for wave functions and charge density, respectively, and used for structural minimizations and total energy calculations. A lattice constant of 4.32 Å was obtained for bulk cubic Cu_2O (experiment: 4.26 Å (Meyer et al., 2012)), with

a Cu-O bond distance of 1.87 Å (experiment: 1.85 Å (Meyer et al., 2012)); for monoclinic CuO, a Cu-O bond distance of 1.95 Å was calculated (experiment: 1.96 Å (Åsbrink and Norrby, 1970)). The copper oxide nanowires and clusters were deposited on the anatase-TiO_2 (101) surface. The 3-layer TiO_2 anatase (101) surface (72 atoms) was modeled with a rectangular (1×2) surface cell of size (10.27 Å $\times$ 7.57 Å). A k-point grid of ($1 \times 2 \times 1$) with the method of Monkhorst and Pack (Monkhorst and Pack, 1976) was used. The TiO_2 slabs had a thickness of three layers, corresponding to ∼10 Å, and the vacuum between the TiO_2 slab and its replica is ∼14 Å thick. Cu_2O and CuO nanowires and clusters were mounted on one side of the slab. In geometry optimizations, all atomic positions were relaxed using conjugated-gradient method and Broyden-Fletcher-Goldfarb-Shanno (BFGS) quasi-Newton algorithm gradient method until the force on each atom was smaller than 0.03 eV/Å. Isolated H_2 and H_2O molecular calculations were performed by placing each one of them in a cubic box of (∼10 Å).

A single water molecule was adsorbed either molecularly or dissociatively (split into OH and H) on possible adsorption sites on Cu_2O/TiO_2 and CuO/TiO_2 nanostructures. The adsorption energy was calculated to determine the most favourable adsorption configurations as follows:

$$E_{ads} = E_{TiO_2/Cu_xO} + E_{H_2O} - E_{TiO_2/Cu_xO/H_2O}, \tag{4.1}$$

where E_{ads} is the adsorption energy, $E_{TiO_2/Cu_xO/H_2O}$, E_{TiO_2/Cu_xO} and E_{H_2O} are DFT total energies of the respective species. In this case, a higher positive value of E_{ads} corresponds to stronger adsorption. The difference in adsorption energy between single water molecule adsorbed on one side and on both sides of the TiO_2 slab was found to be $\sim$ 5.1 meV. Moreover, from Lowdin charge analysis, no net charge transfer is observed on the clean TiO_2 slab.

4.3 Ab Initio Thermodynamics

Gibbs' free energies of formation are calculated by combining DFT calculated free energies with chemical potential for oxygen as explained in (Reuter and Scheffler, 2001; Seriani et al., 2006). In particular, the Gibbs' free energy of formation of a bulk Cu_xO phase is calculated

as the difference:

$$\Delta G^{f}_{Cu_xO}(T,p) = g^{bulk}_{Cu_xO} - g^{bulk}_{Cu}(T,p) - \frac{x}{2} g^{gas}_{O_2}(T,p), \tag{4.2}$$

where $g^{gas}_{O_2}$ (T,p) is the free energy of a dioxygen molecule in the gas phase and g^{bulk} can be written as:

$$g^{bulk} = f^{latt} + f^{vibr} + pV. \tag{4.3}$$

In the expression (4.3), f^{latt}, is the calculated total DFT energy per Cu atom of the optimized crystal. The term f^{vibr} is not taken into account since it results in a small shift that is within the error bar associated with other DFT approximations and the pv term is neglected in solid phases (Reuter and Scheffler, 2001; Seriani et al., 2006; Seriani, 2009).

The chemical potential of oxyen μ_O, is calculated as a function of temperature and oxygen pressure taking into account the translational, vibrational and rotational degrees of freedom of the oxygen molecule in the gas phase (Seriani, 2009; McQuarrie and Simon, 1999a; Dill and Bromberg, 2003):

$$\mu_O = -\frac{1}{2} k_B T ln(Q), \tag{4.4}$$

$$Q = 3(\frac{2\Pi m k_B T}{h^2})^{\frac{3}{2}} \frac{k_B}{p} \frac{T}{2\Theta_{rot}} \frac{1}{1 - e^{-\Theta_{vib}/T}}, \tag{4.5}$$

where m is the mass of the oxygen molecule, k_B Boltzmann's constant, h Planck's constant, T the temperature, p the pressure, Θ_{rot} the rotational temperature (2.08 K) and Θ_{vib} the vibrational temperature (2274 K) (Dill and Bromberg, 2003). The chemical potentials obtained by this formula differ by less than 20 meV from the measured values (Stull and Prophet, 1971) used in other implementations of ab initio thermodynamics (Reuter and Scheffler, 2001; Seriani et al., 2006) and have been extensively employed in previous works (Seriani and Mittendorfer, 2008; Mittendorfer et al., 2007).

4.4 Thermodynamics of Water Photo-Oxidation

Developing efficient photoelectrocatalysts requires optimizing various properties (e.g., band gaps, band edge character and alignments, electron/hole conductivity and lifetime, and reac-

tion thermodynamics and kinetics). The current study focuses on reaction thermodynamics only. Water oxidation reaction steps are simulated here at the periodic DFT +U level by referencing to the SHE to avoid explicit modeling of proton release into water and electron injection into the semiconductor. Referencing to the SHE greatly simplifies the computation.

As mentioned before, water oxidation is initiated by the formation of surface-trapped photoholes. Valdes and Kroes reported a DFT study on TiO_2 showing that calculations using neutral clusters as reactive catalysts give very similar results as calculations on positively charged clusters with one hole (Valdes and Kroes, 2010). They also showed that these cluster calculations gave similar results as periodic DFT calculations. Physically, localized holes at the surface should enhance water oxidation, thus charge neutral models should provide a theoretical upper bound for overpotential estimates based on thermodynamics. On the other hand, since kinetic barriers are not evaluated here, the estimated overpotentials based on thermodynamics are lower bound estimates for the measured overpotentials. These two counter factors compete, resulting in error cancellation to some degree, hence theoretical overpotentials scale well with actual measured overpotentials. For instance, in hematite, the experimental and theoretical overpotential of (0.5 - 0.6) V (Sivula et al., 2011) and 0.7 V (Liao et al., 2012), respectively, are comparable.

Water oxidation is a four-electron semi-reaction leading to the formation of molecular oxygen. The path way that involves direct recombination of two oxygen adsorbates could in principle be a viable mechanism for the O-O bond formation step, however calculations show that this route has a prohibitively high activation energy (Nguyen et al., 2014). Generally, the most accepted mechanism is that of a nucleophilic attack of a solvent water molecule on an oxygen adsorbate, leading to the formation of a hydroperoxo group HOO^*. From previous studies in this field, (Nguyen et al., 2014; Nørskov et al., 2004) the water oxidation mechanism consists of the following series of proton-coupled electron transfer (PCET) steps:

$$
\begin{aligned}
2H_2O + (^*) &\xrightarrow{A} HO^* + H_2O + H^+ + e^- \\
&\xrightarrow{B} O^* + H_2O + 2(H^+ + e^-) \\
&\xrightarrow{C} HOO^* + 3(H^+ + e^-) \\
&\xrightarrow{D} O_2 + (*) + 4(H^+ + e^-),
\end{aligned} \tag{4.6}
$$

where (*) represents an active surface site; for example, O* is an oxygen atom adsorbed at an active surface site. Step C represents the nucleophilic attack. The step ordering can be different from surface to surface.

To calculate the free energy differences between the intermediates in the PCET reaction steps presented in equation 4.6, the method introduced by Nørskov and co-workers is adopted (Nørskov et al., 2004). The standard hydrogen electrode (SHE) potential, where the equilibrium 1/2 $H_2 \leftrightharpoons H^+ + e^-$ at $p(H_2) = 1$ bar and T = 298 K is established, is set to be the reference potential, hence has by definition an electrode potential U = 0. For a PCET, the chemical potentials of electrons and protons do not need to be known separately, and using the SHE as reference their sum can be taken to be equal to the chemical potential of gas phase hydrogen, which can be easily computed. At standard conditions (U_b = 0, pH = 0, p = 1 bar, T = 298 K), the reaction free energy of $HA^* \rightarrow A + H^+ + e^-$ can therefore be calculated as that of $HA^* \rightarrow A + 1/2H_2$. The effect of the external bias U_b (measured against the SHE) is to modify the chemical potential of the electrons by $-eU_b$, while the effect of pH is to modify the chemical potential of the protons by $-k_B$T ln(10)pH. Accordingly, the reaction free energy of a PCET step is computed according to

$$
\Delta G(U_b, pH) = \Delta E + (\Delta ZPE - T\Delta S) - eU_b - k_B T ln(10) pH, \tag{4.7}
$$

where the reaction energy (ΔE), the zero point energy change (ΔZPE), and the entropy change (TΔS) are calculated using DFT.

The DFT energy values of H_2O and H_2 are used as references states since they are well described within DFT (Valdes et al., 2008). The free-energy change of the total reaction $H_2O \rightarrow 1/2\ O_2 + H_2$ is fixed at the experimentally found value of 2.46 eV per water molecule.

This is done in order to avoid DFT calculations of O_2 since this molecule has a complicated electronic structure, which is not described accurately with DFT (Valdes et al., 2008). This means that in the reaction step involving the formation of O_2, its considered that:

$$\begin{aligned}\Delta G_{2H_2O \rightarrow O_2+2H_2} &= 4.92\, eV \\ &= E_{O_2} + 2E_{H_2} - 2E_{H_2O} + (\Delta ZPE - T\Delta S)_{2H_2O \rightarrow O_2+2H_2}. \end{aligned} \tag{4.8}$$

In this model, its approximated that, the overall effect of a water layer would be similar for all intermediates species, hence their relative energies would result to minor differences compared to the vacuum case, that is under consideration herein (Nguyen et al., 2014). It has also been shown that presence of a water layer only slightly changes the overpotential (0.06 V) (Liao et al., 2012). Valdes et al. reported a water oxidation model of TiO_2 rutile 110 surface, in which the effect of interaction energy of water with O*, OH*, OOH*, or an empty coordinately unsaturated site (CUS) is considered similar and approximated, to be equal to the energy of a hydrogen bond (Valdes et al., 2008). This effect was found to be negligible in similar rutile-type oxides (Rossmeisl et al., 2007). In these calculations, it's assumed that entropy, S = 0 for the atoms and molecules adsorbed to the CUS site. The temperature dependence of the enthalpy is neglected in the calculations (its assumed ΔH(298 K) = ΔH(0 K) (Valdes et al., 2008).

CHAPTER FIVE

RESULTS AND DISCUSSIONS

5.1 Structural, Thermodynamic and Electronic properties of Bulk Cu_2O and CuO Oxides

5.1.1 Structural and Thermodynamic properties

Cu_2O has a cubic structure with space group *Pn3m* and the crystal structure is shown in Fig. 5.1a, while CuO has a monoclinic crystal structure with C2/c symmetry, as shown in Fig. 5.1b.

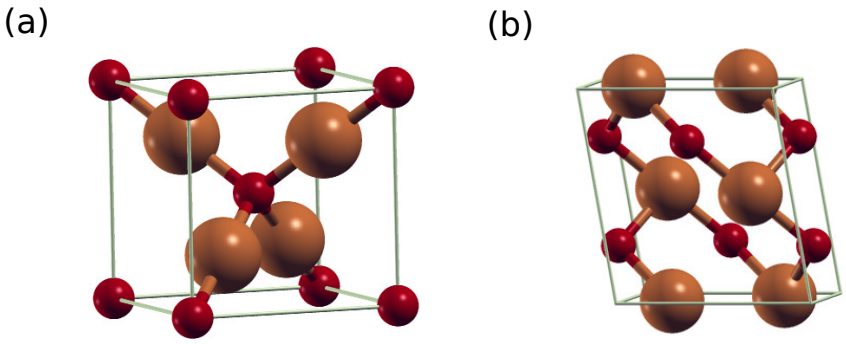

Figure 5.1: Optimized crystal structures of bulk copper oxides: (a) Cu_2O and (b) CuO. Red balls: oxygen; red-brown ball: copper.

The lattice parameters were determined and compared with experimental data: Cu_2O (Meyer et al., 2012) and CuO (Åsbrink and Norrby, 1970) as shown in Table 5.1.

Table 5.1: DFT-PBE+U calculated Cu_2O and CuO structural parameters and Cu-O bond lengths compared to experimental data.

		This Work (Å)	Experimental (Å)
Cu_2O	a	4.3224	4.2696
	Cu-O	1.87	1.85
CuO	a	4.692	4.6837
	b	3.529	3.4422
	c	5.203	5.1288
	Cu-O	1.95	1.96

The agreement between our calculated structural parameters and experimental data is fairly good. The lattice constant, a and Cu-O distance for cubic Cu_2O differ from experiment by +1.23% and +1.08%, respectively. For the CuO, the deviations from experimental values

for a, b and c are +0.12%, +3.1% and +1.4%, respectively. The small deviations are due to DFT approximations.

From the optimized structures, the thermodynamic stability of the two copper oxides phases in equilibrium with gas-phase O_2 at a specified pressure p and temperature T was calculated by use of *ab initio* thermodynamics according to references (Reuter and Scheffler, 2001; Seriani et al., 2006; Seriani, 2009). As mentioned before, the Gibbs free energy of formation of bulk Cu_xO is calculated as the difference:

$$\Delta G^{f}_{Cu_xO}(T,P) = g^{bulk}_{Cu_xO}(T,p) - g^{bulk}_{Cu}(T,p) - \frac{x}{2} g^{gas}_{O_2}(T,p), \tag{5.1}$$

where $g^{gas}_{O_2}$ is the free energy of a dioxygen molecule obtained from O_2 DFT energy and chemical potential, μ_O. The Gibbs free energy, g^{bulk} can be written as $g^{bulk}=f^{latt}+f^{vibr}+pv$. f^{latt} is the total DFT energy per Cu atom. As mentioned earlier, the term f^{vibr} is not taken into account since it results in a small shift that is within the error bar associated with other DFT approximations and the pv term is neglected in solid phases.

Plots of Gibbs free energy versus temperature at oxygen pressure equal to 1 atm and calculated phase diagram of the copper oxides are shown in Fig. 5.2. The location of the phase transitions and the temperature dependence are in good agreement with both theoretical, (Heinemann et al., 2013) and the experimentally determined phase diagrams (Schmidt-Whitley et al., 1974). These findings show that at temperature interval between 100 K and 617 K, Cupric oxide (CuO) is the most stable phase of the copper oxides, therefore Cuprous oxide (Cu_2O) can easily be oxidized to CuO at room temperature. At higher temperatures above 617 K, metallic copper is thermodynamically stable.

5.1.2 Electronic properties

The calculated total density of states (TDOS) and the projected density of states (PDOS) of bulk Cu_2O are presented in Fig. 5.3. The valence band (VB) is dominated by Cu 3d states and moderate contribution from O 2p with minor contributions from Cu 4s states at the top of the valence band. The bottom of the conduction band (CB) is composed of Cu 4p and O 2p states, while Cu 4s and Cu 4p states occupy the top of the CB. The calculated band gap is 0.69 eV, which agrees quite well with other DFT+U calculated values that

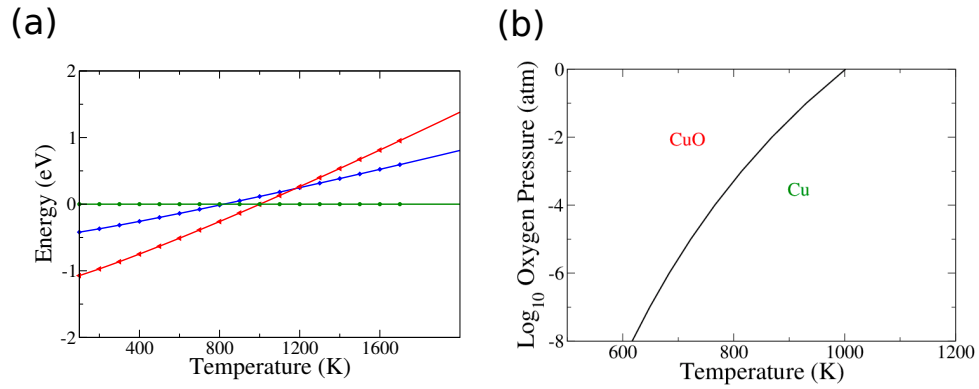

Figure 5.2: (a) Calculated Gibb's free energy of CuO (red line with triangles), Cu_2O (blue line with diamonds) and Cu (green line with circles) at 1 atm oxygen pressure as a function of temperature. Metallic copper has 0 eV free energy. (b) Phase diagram showing the pressure and temperature ranges of bulk copper oxides.

ranged between 0.63-0.94 eV (Tran and Blaha, 2011) and is even greater than the earlier calculated DFT-PBE value of 0.47 eV (Soon et al., 2005). However, it is significantly lower than the experimental value of 2.17 eV (Heinemann et al., 2013) due to inherent errors to the functionals used in local density and generalized gradient approximation such as self-interaction and over-delocalization of electrons. Because of the closed 3d shell, Cu_2O is not considered to be a strongly correlated material (Bruneval et al., 2006) and DFT+U method slightly improves the accuracy of band gap calculation.

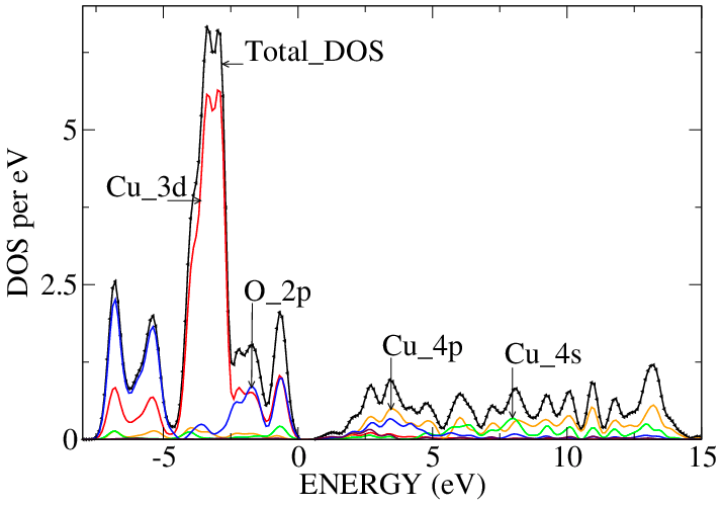

Figure 5.3: TDOS and PDOS of bulk Cu_2O oxide. The Fermi-level is set to zero. The total DOS has been reduced by a factor of 3.5 to put them on the same scale as the PDOS.

The TDOS and PDOS of CuO from DFT+U calculations is shown in Fig. 5.4. The symmetric DOS for both spin up and down indicates an antiferromagnetic state. This

work determined an energy gap of 1.2 eV, which is close to similar DFT+U studies that yielded an energy gap of 1.0 eV (Wu et al., 2006). This value is in good agreement with the experimental energy gap of monoclinic CuO determined to lie between 1.21 eV and 1.7 eV (Koffyberg and Benko, 1982). It is important to note that, PBE-PAW pseudopotentials and DFT+U+J (U=5.2 eV, J=2.5 eV) were employed to obtain an energy gap of 1.2 eV and a local magnetic moment per formula unit of 0.66 μ_B, the latter lies within the range of experimental values of (0.65-0.68) μ_B (Mishra et al., 2016). Himmetoglu et al. (Himmetoglu et al., 2011) reported that the exchange interaction parameter J, localizes a hole in Cu $3d_{z2}$, which favors band gap formation and stabilized magnetic interactions. Calculations performed at U=5.2 eV and GGA-PBE pseudopotentials, yielded unclear energy gap and the d-states crossed the Fermi level. Moreover, it results into inaccurate reproduction of the insulating and antiferromagnetic nature of CuO.

From the PDOS (see Fig. 5.4), the valence band is mainly composed of Cu 3d states with notable contributions from O 2p states. The top of the valence band is dominated by O 2p states that are hybridized with moderate contributions from Cu 3d states in agreement with observations of Ekuma et al (Ekuma et al., 2014). In the CBM, the states near the Fermi level are predominantly Cu 3d states with significant contributions from O 2p states. The results from bulk calculations formed the basis of the following theoretical work on Cu oxide nanowires and clusters.

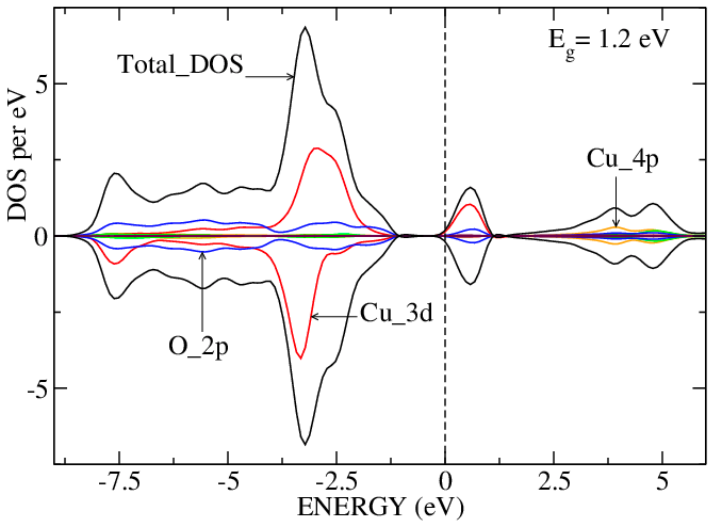

Figure 5.4: TDOS and PDOS of bulk CuO oxide. The Fermi-level is set to zero. The total DOS has been divided by 2.5 to put on the same scale as the PDOS.

5.2 Ab Initio Simulations of Copper Oxide Nanowires and Clusters on TiO_2 (101)Anatase Surface

This section contains results that have been published (Meng'wa et al., 2017).

5.2.1 Atomic Structures

This study considered an extensive structural search of possible structures with Cu_2O and CuO stoichiometries, with four copper atoms in the simulation cell. Different strategies were followed to produce initial configurations for the optimization algorithm. First, clusters and more elongated structures were created by extracting them from the bulk oxide structures. Second, an appropriate amount of oxygen atoms were added to the tetrahedron Cu_4 cluster that was found to be stable in previous work on metallic clusters (Seriani et al., 2015), and that had been shown to have a low barrier for conversion of CO_2 to methane (Liu et al., 2015a). Third, building on the outcome of these relaxations, educated guesses for further possible structures were considered.

The optimized geometries are shown in Fig. 5.5 and Fig. 5.6 for the Cu_2O and CuO stoichiometries, respectively. The most stable structure is the Cu_2O nanowire shown in Fig. 5.5a, with an almost planar geometry. Interestingly, planar structures were also found to be favourable for copper clusters in vacuum (Baishya et al., 2011). For each figure, the difference in total energy ($\triangle$E) at zero temperature between each structure and the most stable one for each stoichiometry is also reported. For the structures with the Cu_2O stoichiometry, the stable nanowire structure lies lower than the second most stable structure by 1.15 eV, which is several times larger than k_BT at room temperature. On the contrary, in the case of CuO, the second lowest structure is only 0.13 eV higher in energy, suggesting that coexistence may be possible.

The metastable tetrahedral Cu_2O cluster (Fig. 5.5b), has two O atoms bound on the sides of tetrahedral Cu_4 cluster. The O atom at the top of the tetrahedral is bound to triangular Cu atoms, while the other O atom is bound between two Cu atoms and a Ti surface atom. The Cu_2O cluster in Fig. 5.5c is similar to the metastable tetrahedral Cu_2O cluster, except for the orientation, which is perpendicular to the TiO_2 surface and the Cu atom at the bottom of the cluster, that also forms bonds with Ti surface atoms. The Cu_2O

cluster in Fig. 5.5d, forms 3 Cu_2O units. For the least stable Cu_2O cluster in Fig. 5.5e, one O atom inserts itself into the center of a tetrahedral Cu framework and the other O atom attaches to one Cu atom. The Cu_2O cluster binds to the TiO_2 surface through Cu-Ti bond and two Cu-O bonds.

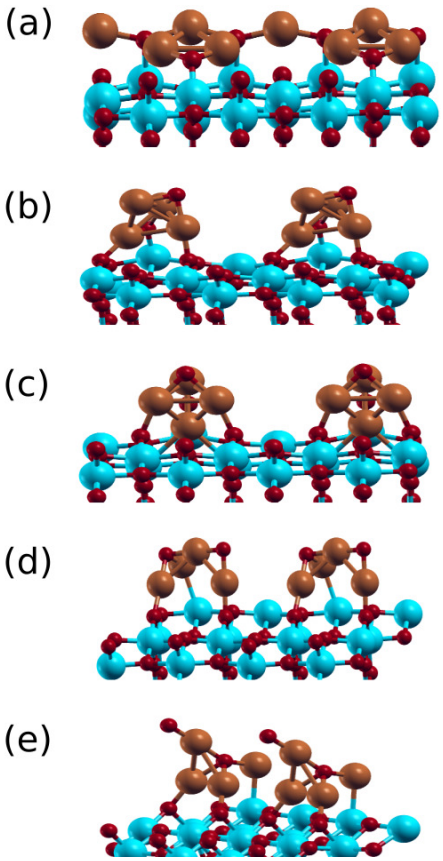

Figure 5.5: Optimized Cu_2O nanowire and clusters mounted on TiO_2 (101) surface with their respective total energy differences with respect to the most stable structure (a). (a) △E=0 eV; (b) △E=1.15 eV; (c) △E= 1.52 eV; (d) △E=2.10 eV; (e) △E=3.54 eV. Blue balls; titanium, red balls; oxygen, red-brown balls; copper. The two Cu_2O nanowire/clusters shown on TiO_2 anatase (101) surface are replicas of each other.

The stoichiometry of the copper oxide nanostructures are either Cu_2O or CuO. However, their structure might differ considerably from those of the bulk oxides. To illustrate this, in Table 5.2 and Table 5.3, the average atomic distance are reported.

For Cu_2O structures, the range of Cu-Cu bonds are very close to that of experimental bulk metal copper of 2.54 Å, but more than Cu-Cu lengths of the dimer (Cu_2) that ranged between 2.28 Å, and 2.31 Å, (Seriani et al., 2015). The Cu-O bond lengths increased and decreased in the range of 0.11 Å, to 0.01 Å, respectively, compared to the experimental Cu_2O bulk value of 1.85 Å, and longer than Cu-O length of 1.8 Å, from DFT calculations for bulk

Table 5.2: The average bond lengths in optimized structures of Cu_2O/TiO_2 nanowire and clusters. All in units of Å.

nanowire/clusters	Cu-Cu	Cu-O	Cu-Ti	O-Ti_{5C}	Cu-$O_{2C-surf.}$
a	2.53	1.96		2.02	1.92
b	2.52	1.91		1.82	1.88
c	2.44	1.90	2.79	1.76	1.98
d	2.60	1.84	2.68		1.90
e	2.59	1.88	2.62		1.90

Cu_2O (Heinemann et al., 2013). A Cu-Ti bond is found in the structures shown in Figs. 5.5c to 5.5e, with bond lengths ranging from 2.62 Å to 2.79 Å, considerably shorter than the Cu-Ti bond previously found in metallic copper clusters on TiO_2 (2.92 Å), (Seriani et al., 2015). However, it should be noted that the most stable structures exhibit a O-Ti_{5C} rather than a Cu-Ti bond. Regarding coordination, most of the Cu atoms in Cu_2O structures have their total coordination ranging between 4- and 5-fold, and only few have a 2-fold coordination like in the bulk. 3-fold coordinated O atoms are most prevalent, which is also different from bulk Cu_2O, where O is coordinated to 4 Cu atoms.

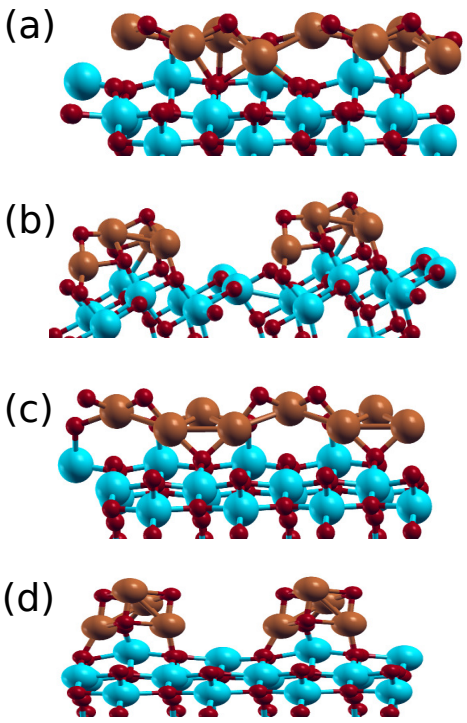

Figure 5.6: Optimized CuO nanowire and clusters mounted on anatase TiO_2 (101) surface with their respective total energy differences referenced to the most stable stable structure. (a) △E=0 eV; (b) △E=0.13 eV; (c) △E= 0.49 eV; (d) △E=1.23 eV. Colour code as shown in Fig. 5.5. The two CuO nanowire/clusters shown on TiO_2 anatase (101) surface are replicas of each other.

The most stable CuO/TiO_2 (see Fig. 5.6a) is built from addition of one O atom at the top of the triangular Cu_3 cluster in Fig. 5.5a. The other O atom is added between the two adjacent Cu atoms that are not bonded. The metastable CuO cluster on TiO_2 surface shown in Fig. 5.6b, was cut as a planar structure from bulk CuO. The atomic structure of the cluster is very similar to that of the CuO nanowire on the (101) TiO_2 surface (see Fig. 5.6a), except for the separation between the replica of at least 4.0 Å, that makes it not to form a nanowire. The CuO nanowire on TiO_2 surface in Fig. 5.6c is modified from the most stable CuO/TiO_2 structure, whereby one oxygen atom has been removed from the top of the triangular Cu atoms and then anchored on the Cu atom to make it coordinated to four O atoms, similar to the situation in the bulk. For the optimized structure in Fig. 5.6d, two O atoms were added to the Cu_2O/TiO_2 cluster shown in Fig. 5.5b, whereby each O atom is placed on the side of the triangular Cu atoms. This resulted into 3 sets of tetrahedra each with 3 Cu atoms at the base and one O atom at the vertex.

In the CuO nanostructures, the Cu-Cu bond lengths are about 0.1 Å longer than those of experimental bulk copper metal of 2.54 Å; on the contrary, in the Cu_2O the distances were similar to those in bulk metallic copper. The Cu-O bonds are in most cases slightly contracted in a range of -0.02 Å to -0.01 Å. A Cu-Ti bond is present in one of the structures (Fig. 5.6b) with a Cu-Ti distance of 2.78 Å. The O-Ti_{5C} bond distances are in good agreement with O-Ti bond lengths seen in surface x-ray diffraction (SXRD) studies of anatase-TiO_2 (101) surface that ranged between 1.89 Åand 2.03 Å(Treacy et al., 2017), except for one value of 1.81 Å. The Cu-O_{2C} bond, which is between Cu atom and two-fold coordinated oxygen atom (O_{2C}) on the TiO_2 surface ranges between 1.89 Åand 2.13 Å. These values are within the ranges almost equivalent to O-Ti bond lengths obtained in SXRD studies of anatase-TiO_2 (101) surface (Treacy et al., 2017).

A greater number of the Cu atoms in the CuO structures are 4-, 5- and 6-fold coordinated. Except for one 4-fold coordinated Cu atom, nearly all Cu atoms are overcoordinated compared to Cu atoms in bulk CuO. In contrast, almost all oxygen atoms are undercoordinated with the O_{3C} being the most frequent. The triangular frameworks of Cu-Cu-Cu and Cu-Cu-O are the most dominant patterns in Cu_2O, in agreement with other cluster studies (Yang et al., 2010; Jadraque and Martín, 2008). The Cu_3 units are significantly present in the CuO nanowire/clusters and in almost all the copper oxide structures under

Table 5.3: The average bond lengths in the optimized structures of CuO/TiO_2 nanowires and clusters. The bond lengths are in Å.

nanowires/clusters	Cu-Cu	Cu-O	Cu-Ti	O-Ti_{5C}	Cu-$O_{2C-surf.}$
a	2.68	1.94		1.95	2.13
b	2.65	1.96	2.78	1.89	1.91
c	2.68	1.95		2.00	1.96
d	2.62	1.95		1.81	1.89

Table 5.4: Calculated formation energies of the three most stable structures of 3L (see Figs. 5.5a-5.5c) and 2L Cu_2O/TiO_2 (see Fig. A.1: Appendix A) structures.

Structures	Formation energies (eV)	
	3L (10 Å× 7.57 Å)	2L (10 Å× 15.15 Å)
a	-5.45	-4.58
b	-4.30	-4.21
c	-3.93	-3.78

consideration.

This study also considered the most stable 3-layer (3L; 10 Å× 7.5 Å) structures with a vacuum 14 Å, of relaxed Cu_2O/TiO_2 (see Figs. 5.5a to 5.5c) and CuO structures (see Figs. 5.6a to 5.6c) and increased the supercell size to (10 Å× 15 Å) with vacuum of 18 Å. The enlarged supercells were made 2-layers (2L) to reduce the computational costs. Structural relaxations were performed and three most stable optimized 2L Cu_2O/TiO_2 and CuO/TiO_2 structures are arranged in the decreasing order of stability in Fig. A.1 and Fig. A.2 (Appendix A), respectively. Calculated formation energies of the three most stable 3L and 2L Cu_2O/TiO_2 and CuO/TiO_2 systems are reported in Tables 5.4 and 5.5, respectively.

It is noted that for low density/large distance between nanowires and clusters on TiO_2 2L (101) surface, the formation energy values change, but only slightly compared to the

Table 5.5: Calculated formation energies of the three most stable structures of 3L (see Figs. 5.6a-5.6c) and 2L CuO/TiO_2 (see Fig. A.2: Appendix A) structures.

Structures	Formation energies (eV)	
	3L (10 Å× 7.57 Å)	2L (10 Å× 15.15 Å)
b(3L) and a(2L)	-2.56	-2.35
a(3L) and b(2L)	-2.48	-1.41
d(3L) and c(2L)	-1.46	-1.39

values of high density of wires/clusters (3L) but stable structures remain consistent.

5.2.2 Thermodynamic Stability of Nanowires

Thermodynamic stability of the most stable Cu_2O/TiO_2 and CuO/TiO_2 nanowires shown in Figs. 5.5a and 5.6a, respectively, were investigated at finite temperature. The Gibbs free energies in equilibrium with gas-phase O_2 at a specified pressure (p) and temperature (T) using *ab-initio* thermodynamics were approximated by DFT total energies and oxygen chemical potential, μ_O (Reuter and Scheffler, 2001; Seriani et al., 2006; Seriani, 2009; McQuarrie and Simon, 1999b). In particular, the Gibbs free energy of formation is calculated as the difference:

$$\Delta G^f_{Cu_xO/TiO_2}(T,P) = g_{Cu_xO/TiO_2} - g_{Cu_4/TiO_2} - \frac{x}{2} g^{gas}_{O_2}, \tag{5.2}$$

where $g^{gas}_{O_2}$ is the free energy of a dioxygen molecule obtained as described in Ref. (Reuter and Scheffler, 2001) and g can be written as g=f^{latt}+f^{vibr}+pv. f^{latt} is the total DFT energy per Cu atom. The term f^{vibr} is the vibrational contribution and is not taken into account(Reuter and Scheffler, 2001; Seriani et al., 2006; Seriani, 2009; McQuarrie and Simon, 1999b) since it results in a small shift, which is within the error bar associated with other DFT approximations, and the pv term is neglected in solid phases. Plots of the calculated Gibbs free energy values against temperature at 1 atmosphere (atm), 10^{-5} atm and 10^{-10} atm of oxygen pressure are shown in Fig. 5.7. At both low and high temperature and oxygen pressure, the CuO/TiO_2 nanowire was found to have higher values of Gibbs free energy compared to Cu_2O/TiO_2. This indicates that Cu_2O nanowire on TiO_2 (101) surface is thermodynamically more stable than CuO nanowire on the same surface, unlike in bulk Cu oxides, where CuO is the most stable phase compared to Cu_2O at ambient conditions (Heinemann et al., 2013). This is also consistent with results of Ayyub et al. (Ayyub et al., 1995), where their studies on the effect of reducing the size of the particles on the crystal structure of Cu_2O and CuO over a nanometer scale, found cubic Cu_2O to be more stable than monoclinic CuO. This was attributed to the fact that Cu_2O is more symmetric and more ionic than CuO. The nanometer particle size increases the ionic nature of the copper oxides and makes the lattice less directional, and hence the more symmetric phase becomes

more stable (Han et al., 2005).

The same results could also be interpreted as a consequence of the lower surface energy of Cu_2O surfaces. Theoretical works (Soon et al., 2007b; Soon et al., 2007a; **?**) predict that CuO (111), which is the most stable CuO surface, has a higher surface energy of 0.76 J/m^2 compared to 0.048 J/m^2 and 0.4 J/m^2 for the oxygen-rich and oxygen-poor terminations of Cu_2O(111). This could explain obtained result, since for nanoparticles, the surface energy contribution is very important in determining stability (Seriani et al., 2007).

The energy versus temperature plots in Fig. 5.7, show a corresponding decrease of transition temperature with pressure for the Cu oxides nanowires to Cu metal on TiO_2 (101) anatase surface. For the case of CuO to Cu (see Figs. 5.7b and 5.7c), the transition temperature at p=10^{-5} atm and p=10^{-10} atm is 871 K and 680 K, respectively.

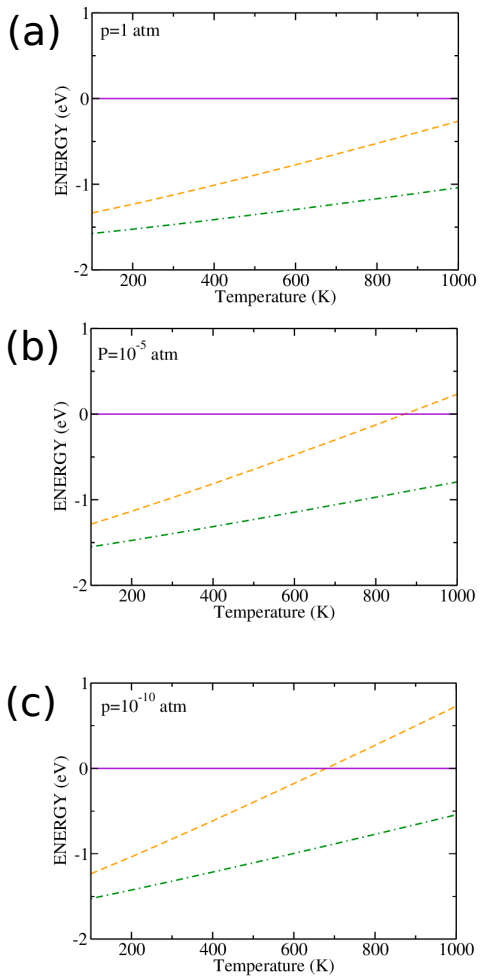

Figure 5.7: Calculated Gibb's free energy of CuO (orange dashed line) and Cu_2O (green dotted-dashed line) with respect to Cu (violet solid line) nanowires on TiO_2 (101) anatase surface at (a) 1 atm, (b) 10^{-5} atm and (c) 10^{-10} atm oxygen pressure as a function of temperature.

5.2.3 Electronic Structure

The total density of states (TDOS) and partial densities of electronic states (PDOS) of the most stable Cu_2O/TiO_2 and the metastable CuO/TiO_2 nanowire have been investigated, to shed light on the behaviour of the system in dependence of the degree of oxidation of the copper nanostructures. The PDOS of the Cu_2O nanowire is shown in Fig. 5.8. The upper valence band from -5 eV to -1.25 eV is mainly occupied by Cu 3d states with moderate contributions from O 2p. The Cu 3d and O 2p states extend the valence band edge by $\sim$1.5 eV into titania energy gap. The lower valence band consists mainly of hybridized states of O 2p, Cu 3d and Ti 3d. The conduction band is predominantly composed of empty Ti 3d states.

The Löwdin atomic charges and spin magnetic moments show no charge transfer between the Cu_2O nanowire and the TiO_2 anatase (101) surface atoms (see Table 5.6) and (Table A.1 in Appendix A).

Table 5.6: Change in total Löwdin charge ($\triangle$Q) and Polarization ($\triangle\mu$) of Cu and O atoms in clean Cu_2O nanowire and Cu_2O/TiO_2 nanowire with respect to Cu_2O bulk as calculated from their respective PDOS.

Atomic species	$\triangle$Q(|e|)		$\triangle\mu(\mu_B)$	
Cu/O	Cu_2O-NW	Cu_2O/TiO_2-NW	Cu_2O-NW	Cu_2O/TiO_2-NW
Cu	0.00	0.00	0.00	0.00
Cu	0.03	0.14	0.00	0.00
Cu	0.08	0.14	0.00	0.00
Cu	0.15	0.06	0.00	0.00
O	0.07	0.18	0.00	0.00
O	0.10	0.18	0.00	0.00

A narrowed energy gap of 1.61 eV was obtained because the states of Cu_2O nanowire extended into the titania bandgap. The energy level alignment favours electron transfer from the CB of Cu_2O nanowire into TiO_2 CB. This is in agreement with the findings of Dongliang et al. (Dongliang et al., 2015), who established that for Cu_2O/TiO_2 coupled system, visible light excitation forces photogenerated electrons to be transferred from the CB of Cu_2O to the CB of TiO_2. Meanwhile, valence band alignment drives holes towards Cu_2O, thus fostering charge separation and hence suppressing recombination of photogenerated electrons and holes. The reduced energy gap in turn extends the photoabsorption to visible range. Jagminas et al. (Jagminas et al., 2014) similarly noted that the shift in the energy gap

of titania nanotube film sample from ∼ 3.18 eV to visible range ∼2.3 eV for Cu_2O/TiO_2 sample is attributable to visible light charge transfer from Cu_2O to TiO_2. The electronic structure of metastable Cu_2O cluster (Fig. 5.5b) displays similar features, except for the small shoulder peak at the bottom of the CB of TiO_2 (see Fig. 5.10a).

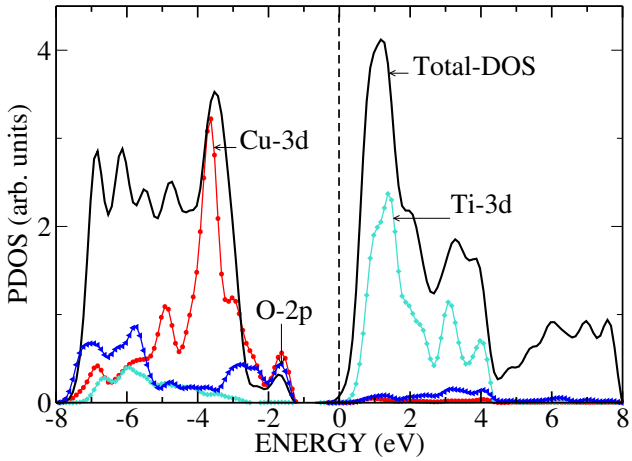

Figure 5.8: PDOS of the Cu_2O nanowire on the TiO_2 (101) surface. Black solid line: total DOS; red line with circles: Cu-3d; blue line with triangles: O-2p; turquoise line with diamonds: Ti-3d. Fermi level is set at 0 eV. The total DOS has been reduced by a factor of 15 to be on the same scale as the PDOS.

The PDOS of TiO_2 anatase (101) surface modified by the CuO nanowire is shown in Fig. 5.9. This study established that, the top of the valence band is predominantly composed of O 2p states with significant contribution from Cu 3d states. The valence band is largely made up of Cu 3d states with moderate and small contributions of O 2p states and Ti 3d states, respectively. The TiO_2 energy gap is occupied by O 2p states and Cu 3d states with a pronounced peak located at ∼0.8 eV above the Fermi level. This empty Cu 3d state near the bottom of the conduction band is not present in the Cu_2O structures. Photogenerated electrons should therefore be preferentially transferred to this CuO state from titania. This is in agreement with the findings of Yu et al. (Yu et al., 2011), who reported that the conduction band (CB) edge of TiO_2 is higher than that of CuO clusters, therefore photogenerated electrons transfer from the CB of TiO_2 into the CB of CuO clusters. Since also the highest filled states belong to CuO, holes should be transferred there as well. This is an important difference with respect to Cu_2O structures, where only holes should be transferred to the copper oxide.

Similar to the case of Cu_2O on TiO_2 (101) anatase surface at 0 K, it was observed that no charge is donated from CuO nanowire to TiO_2 surface atoms as depicted in Table 5.7

and Table A.2 (Appendix A).

Table 5.7: Change in total Löwdin charge ($\triangle$Q) and Polarization ($\triangle\mu$) of Cu and O atoms in isolated CuO nanowire and CuO/TiO_2 nanowire with respect to CuO bulk as calculated from their respective PDOS.

Atomic species	$\triangle$Q(|e|)		$\triangle\mu(\mu_B)$	
Cu/O	CuO-NW	CuO/TiO_2-NW	CuO-NW	CuO/TiO_2-NW
Cu	0.01	0.09	0.03	0.18
Cu	0.00	0.03	0.45	0.05
Cu	0.00	0.03	0.45	0.68
Cu	0.12	0.02	0.13	0.12
O	0.12	0.02	0.36	0.39
O	0.04	0.00	0.93	0.02
O	0.03	0.19	0.91	0.25
O	0.01	0.19	0.85	0.31

The qualitative features of TDOS and PDOS of metastable CuO/TiO_2 cluster (see Fig. 5.10b) are similar to those of most stable CuO/TiO_2 nanowire, except for the less pronounced peaks of Cu 3d and O 2p in TiO_2 energy gap.

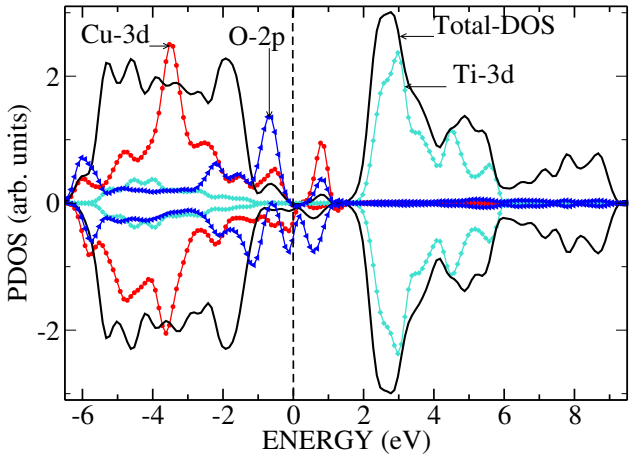

Figure 5.9: PDOS of a CuO nanowire on the TiO_2 (101) surface. Black solid line: total DOS; red line with circles: Cu-3d; blue line with triangles: O-2p; turquoise line with diamonds: Ti-3d. Fermi level is set at 0 eV. The total DOS has been reduced by a factor of 20 to be on the same scale as the PDOS.

The results of this study suggest that for Cu nanostructured oxides on TiO_2, Cu_2O/TiO_2 is more efficient for charge separation than CuO/TiO_2. This is in qualitative agreement with Ref. (Liu et al., 2013b), where it was observed that presence of Cu^+ led to a higher photocatalytic activity, which was attributed to a better charge separation. Regarding electron transfer in CuO/TiO_2, the results of this study are in good agreement with the

experiments by Yu and co-workers (Yu et al., 2011), who conclude that the empty CuO states are below the bottom of the conduction band of TiO_2 and the filled states of CuO are above the top of the valence band of TiO_2. Thus, a driving force for transfer of both electrons and holes to CuO is present. However, in the same work, they observe that, while electrons are readily transferred to CuO, holes are present both in CuO and in TiO_2. This points to different transfer rates for holes and electrons. Still, this findings suggest that Cu^+ species should work better towards separation of photogenerated electrons and holes in comparison to Cu^{2+}. Moreover, nanostructured Cu_2O/TiO_2 is thermodynamically more stable than CuO/TiO_2 and therefore more likely to be present under reaction conditions.

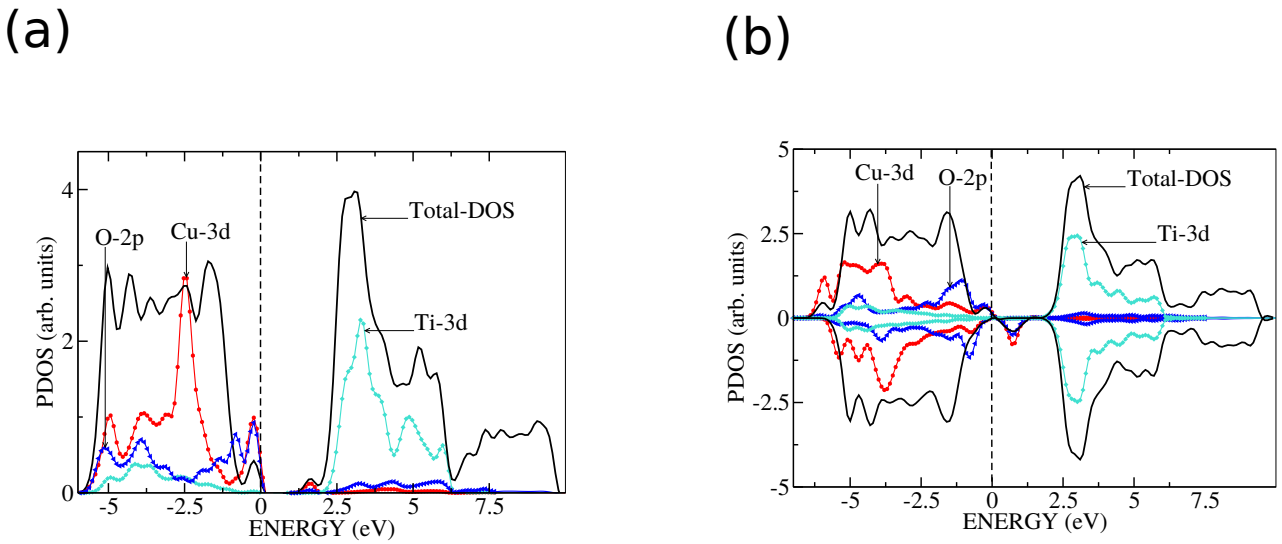

Figure 5.10: TDOS and PDOS of most stable clusters; (a) Cu_2O on TiO_2 (Fig. 5.5b) and (b) CuO on TiO_2 (Fig. 5.6b)(101) anatase surface. Black solid line: total DOS; red line with circles: Cu-3d; blue line with triangles: O-2p; turquoise line with diamonds: Ti-3d. Fermi level is set at 0 eV. The Total-DOS has been scaled down to be on the same scale as the PDOS.

5.2.4 Polarons in nanowired Cu_2O/TiO_2 anatase (101) surface

The polaronic state at $\sim$ 0.8 eV below the conduction band minimum (Ti 3d peak in the energy gap) is displayed in Fig. 5.12. The polaron is characterized by magnetic moment of Ti atom, its charge and geometric distortion. The polaron forms at Ti_{6C} atom lying right below the copper oxide nanowire (Fig. 5.11a). The total charge donated from copper atoms calculated from Löwdin charge is not sufficient to affect the overall charge on the Cu_2O nanowire. It is known that effective atomic charges such as L öwdin charges rarely reproduce the actual charges in transition metal compounds (Resta, 2008). This is normally

attributed to the nature of formal oxidation states and to the fact that electronic charge is delocalized in nearly all atoms in the real material. Furthermore, effective atomic charges arise from different principles, either from the total electronic charge distribution, for the case of Bader charges (Bader, 1990), or from the wave functions, for the case of Löwdin charges (Löwdin, 1955; Seriani, 2012). Again, in Löwdin charges, the actual values of the effective charges could depend on the choice of basis set and atomic wave functions used for the projection. This makes an assignment of atomic charge not absolute, hence calculated values should be used with caution. The analysis becomes more complicated, when electrons donated to these metal oxides go also to the oxygen atoms around the metal ions (Islam and Fisher, 2014). Still, it is accepted in the literature that a polaron in a transition metal oxide is better described by atomic effective charges, magnetic moments and the geometric distortion of the atomic configuration. Specifically, it has been proven that spin localization, given by an increase in the atomic magnetic moment, is a better indicator of the presence of the Ti^{3+} ions than the effective charges (Mellan et al., 2013; Crespo and Seriani, 2014). Using Löwdin analysis (Löwdin, 1955), the computed change in magnetic moment for the Ti atom under discussion here is 0.99 μ_B. The Ti-O distances that constitute the octahedral with Ti atom in question are also increased, the new distances are 2.15 Å, and 2.11 Å, for atoms on the horizontal plane; 2.06 Å, for azimuthal atoms and 2.04 Å, for atoms on the diagonal plane. For comparison, Ti-O distances of the same 6-fold coordinated Ti atom without distortions are 1.92 Å, and 2.06 Å, (vertical), 1.96 Å, (azimuthal) as well as 2.00 Å, and 2.04 Å, (diagonal). The polaronic state is shown by the isodensity plot in Figure 5.11a. This state forms a pronounced Ti-3d peak within the energy gap, as clearly seen in the DOS (Fig. 5.12). As mentioned before, the polaron lies 0.8 eV below the CBM, which is in good agreement with polarons that lie 0.7-0.9 eV below the CB edge, which were observed experimentally in (110) surface of rutile induced by oxygen vacancies (Ganduglia-Pirovano et al., 2007).

The presence of a polaronic state Ti^{3+} generated by localization of charge coming from copper (Cu donated charge of 0.12 |e|, calculated from Löwdin charge) on Ti_{6C} atom right below the Cu_2O nanowire is important for enhancement of photocatalytic performance. In clean titania, it has been reported that storage of electrons at Ti^{3+} sites improves photocatalytic activity (Liu and Li, 2014), probably by increasing the photoabsorption (Serpone,

2006). Certainly, it is known that polarons easily diffuse to the surface in titania, and that electrons from Ti^{3+} sites participate in CO_2 reduction even in the dark (Liu and Li, 2014). Therefore, these calculations support the view that copper can indeed induce the formation of further Ti^{3+} sites, hence fostering photocatalytic activity. Therefore, one significant contributions of copper could be that of increasing the number of Ti^{3+} in the proximity of the surface.

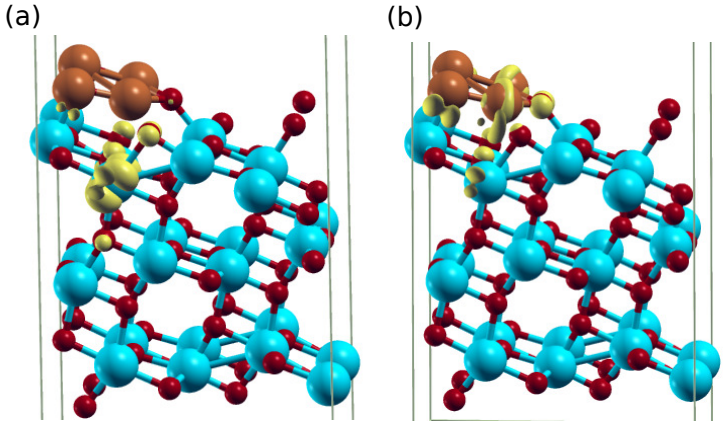

Figure 5.11: Isodensity surfaces for Cu_2O/TiO_2 (101) anatase nanowire system relaxed with DFT+U. a) Polaronic state consisting mainly of Ti-3d states of subsurface six-fold coordinated titanium atom. This state is occupied. b) State consisting of Cu-3d and O-2p states of the copper atoms. The state is empty.

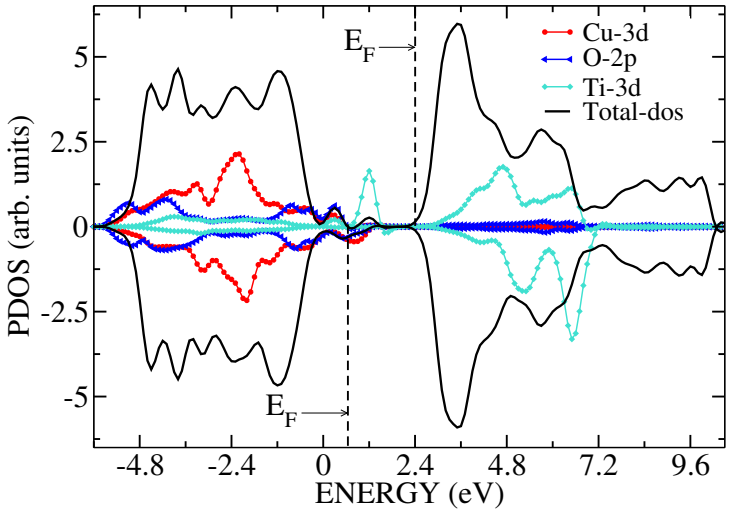

Figure 5.12: TDOS and PDOS of most stable Cu_2O/TiO_2 (101) anatase nanowire system with an excited electron leading to a polaronic state. Fermi level is set to 0 eV. The total DOS has been reduced to be on the same scale as PDOS.

5.3 Water Photo-Oxidation on Cu_2O/TiO_2 and CuO/TiO_2 anatase (101) Surfaces

The results reported in this section have been published in a paper titled: Density Functional Theory Study of Water Photo-Oxidation on Cu_2O/TiO_2 and CuO/TiO_2 anatase (101) Surfaces (Meng'wa et al., 2018).

5.3.1 Water Adsorption

Molecular and dissociative adsorption of water have been considered on the most stable nanostructure Cu_2O/TiO_2 (Fig. 5.5a) and CuO/TiO_2 (Fig. 5.6a). We tested ten configurations for each system, which reduced to symmetries reported in Figs. 5.13 and 5.14, that are based on stabilities and preferential adsorption sites. For the system with Cu_2O, the most stable configurations are shown in decreasing order of stability in Fig. 5.13. The corresponding adsorption energies are shown in Table 5.8.

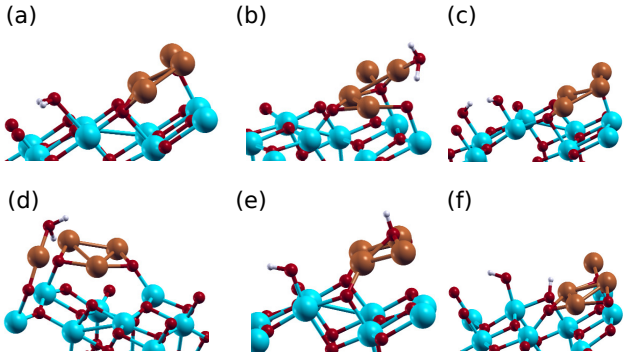

Figure 5.13: Optimized configurations of adsorbed H_2O on Cu_2O/TiO_2 anatase (101) nanowire surface arranged in decreasing order of stability. Blue balls: titanium; red balls: oxygen; red-brown balls: copper and white balls: hydrogen

Table 5.8: Calculated adsorption energies of water molecule on Cu_2O/TiO_2 nanowire surface. The structures are as shown in Fig. 5.13.

Structure	E_{ads} (eV)
a	0.78
b	0.67
c	0.50
d	0.43
e	0.32
f	0.30

Water prefers to adsorb molecularly on Cu_2O/TiO_2 with the oxygen atom from water

molecule being bonded to five-fold coordinated Ti (Ti_{5C}) on the TiO_2 surface with E_{ads} of 0.78 eV (Fig. 5.13a). The most stable dissociated configuration has OH on Ti_{5C} and H on O_{2C} site (Fig. 5.13c). On the contrary, on CuO/TiO_2 dissociated water is favoured, with OH species located at a bridge site between Ti and Cu atoms, and H bound to an O atom on CuO (Fig. 5.14a and Table 5.9). The adsorption energy is 1.12 eV, which is larger than that on Cu_2O/TiO_2.

This behaviour should be compared with those on pure oxides. On TiO_2(101), water is known to adsorb molecularly at low coverage (Vittadini et al., 1998; Herman et al., 2003; Sun et al., 2010; Zhao et al., 2011), with co-existence of molecular and dissociated water at high (monolayer) coverage (Walle et al., 2011; Patrick and Giustino, 2014).

The trend, found with molecular adsorption in presence of Cu_2O and dissociative adsorption in presence of CuO, is in line with the behaviour of the pure copper oxides. DFT indeed predicts molecular adsorption on (111) (Zhang et al., 2013) and (110) (Saraireh and Altarawneh, 2013) surface of Cu_2O, with an adsorption energy of 0.82 eV on the former. Dissociative adsorption is favoured on CuO(111), with an adsorption energy of 0.9 eV (Zhang et al., 2016). We can therefore conclude that CuO contributes to water dissociation, while Cu_2O does not play a role at this stage, since water still prefers to adsorb at sites of the TiO_2 surface. Also metallic copper is unlikely to be a good site for water adsorption or dissociation, since it is known to have low adsorption energies, around 0.4 eV (Chen et al., 2010a), with partial dissociation appearing above 150 K (Andersson et al., 2005). Its important to note that most stable water terminations on Cu_2O/TiO_2 and CuO/TiO_2 are concomitant with empty states at the bottom of the conduction band found in the projected density of states of this systems in our previous work (Meng'wa et al., 2017).

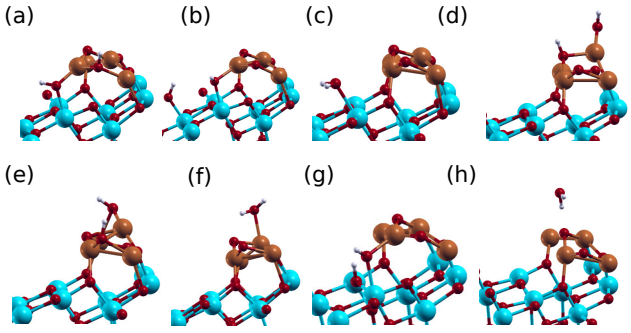

Figure 5.14: Optimized geometries of adsorbed H_2O on CuO/TiO_2 (101) nanowire surface arranged in decreasing order of stability.

Table 5.9: Calculated adsorption energies of water molecule on CuO/TiO_2 nanowire surface. The structures are as shown in Fig. 5.14.

Structure	E_{ads} (eV)
a	1.12
b	1.07
c	1.03
d	0.90
e	0.81
f	0.53
g	0.51
h	0.32

5.3.2 Thermodynamic Stability

Water splitting leads to the formation of surface hydroxyls, hydrogens, oxygens, and other adsorbed species. The thermodynamic stability of the surface in presence of these adsorbants has been determined, as a function of the applied electric bias.

In the following, a given surface termination is denoted as S_k^m (k=1-3 and m=1-2) where k=1: pristine TiO_2 anatase (101) surface; k=2: Cu_2O/TiO_2 terminated surface; k=3: CuO/TiO_2 terminated surface. Two terminations for each of Cu_2O/TiO_2 and CuO/TiO_2 are considered, and either m=1 or m=2 are used to distinguish them. Moreover, $S_k^{m\ (\alpha\beta\gamma)}$ has α O*, β HO*, and γ HOO* adsorbed species. The free energy is given as:

$$G_{S_k^{m(\alpha\beta\gamma)}} = E_{S_k^{m(\alpha\beta\gamma)}} + (ZPE - TS)_{S_k^{m(\alpha\beta\gamma)}}, \tag{5.3}$$

where $E_{S_k^{m(\alpha\beta\gamma)}}$ is the total energy of the respective terminations calculated using DFT+U. ZPE and TS are zero point energy and entropy contributions, respectively, from the adsorbed species. These contributions to the free energies of the reaction intermediates are calculated at room temperature (298 K). The ZPE and TS values of intermediates (O^* , HO^*, HOO^*) on different metal oxides do not change considerably (Nguyen et al., 2014), hence the ZPE and TS values are taken from Ref. (Valdes et al., 2008) shown in Table 5.10.

To determine the stability of the surface-adsorbed species under PCET conditions, the method developed by Nørskov and co-workers (Nørskov et al., 2004) to calculate the surface free energy is employed:

Table 5.10: Zero point energy (ZPE) and entropic contributions (TS) to free energies (G)

Intermediate	ZPE (eV)	TS (eV)	ZPE-TS (eV)
H_2O	0.56	0.67	-0.11
H_2	0.27	0.41	-0.14
1/2 O_2	0.05	0.32	-0.27
HO*	0.35	0	0.35
HOO*	0.41	0	0.41
O*	0.05	0	0.05

$$\gamma(U_b) = \frac{1}{A}[G - \sum_i n_i \mu_i(U_b)], \tag{5.4}$$

where G is the free energy of pristine TiO_2 anatase (101) surface, Cu_2O/TiO_2 or CuO/TiO_2 covered with intermediate species (O, OH, OOH), n_i and μ_i are the number of atoms and chemical potential of type i, respectively. U_b is the effective bias and A is the area of each surface on which the species are adsorbed. In the case of pristine TiO_2 anatase (101) surface, it will be 2A, where the factor of 2 is included since both surface orientations at the top and bottom are equivalent. The redox potential for the photogenerated holes, according to the photoelectrochemical studies (Nozik and Memming, 1996) is about 3.25 V versus the normal hydrogen electrode (NHE) for TiO_2 at pH=0. Thus, the stability of oxidation species at values of $U_b \geq 3.25$ V are of great interest. The chemical potentials of different atomic types (O, H, Ti, Cu) are modified by the bias as follows:

$$\mu_H = \frac{1}{2}G_{H_2} - eU_b, \tag{5.5}$$

$$\mu_O = G_{H_2O} - G_{H_2} + 2eU_b, \tag{5.6}$$

$$\mu_{Ti} = \mu_{TiO_2} - 2\mu_O, \tag{5.7}$$

$$\mu_{Ti} = \mu_{TiO_2} - 2G_{H_2O} + 2G_{H_2} - 4eU_b, \tag{5.8}$$

$$\mu_{Cu}^{Cu_2O} = \mu_{Cu_2O} - \frac{1}{2}(G_{H_2O} - G_{H_2} + 2eU_b), \tag{5.9}$$

$$\mu_{Cu}^{CuO} = \mu_{CuO} - G_{H_2O} + G_{H_2} - 2eU_b, \tag{5.10}$$

$$\mu_{Cu} = G_{Cu}. \tag{5.11}$$

Thus, the surface free energy for pristine TiO_2 anatase (101) surface is:

$$\begin{aligned}\gamma_{S_k{}^{(\alpha\beta\gamma)}} =& \frac{1}{2A}\{G - [n_{Ti}(\varepsilon_{TiO_2} - 2G_{H_2O} + 2G_{H_2}) \\ &+ n_O(G_{H_2O} - G_{H_2}) + n_H\frac{1}{2}G_{H_2} \\ &+ (2n_O - 4n_{Ti} - n_H)eU_b]\},\end{aligned} \tag{5.12}$$

similarly, the surface free energy for Cu_2O/TiO_2:

$$\begin{aligned}\gamma_{S_k^{m(\alpha\beta\gamma)}} =& \frac{1}{A}\{G - [n_{Ti}(\varepsilon_{TiO_2} - 2G_{H_2O} + 2G_{H_2}) \\ &+ n_{Cu}(\varepsilon_{Cu_2O} - \frac{1}{2}G_{H_2O} + \frac{1}{2}G_{H_2}) \\ &+ n_O(G_{H_2O} - G_{H_2}) + n_H\frac{1}{2}G_{H_2} \\ &+ (2n_O - 4n_{Ti} - n_H - n_{Cu})eU_b]\},\end{aligned} \tag{5.13}$$

also, the surface free energy for CuO/TiO_2:

$$\begin{aligned}\gamma_{S_k^{m(\alpha\beta\gamma)}} =& \frac{1}{A}\{G - [n_{Ti}(\varepsilon_{TiO_2} - 2G_{H_2O} + 2G_{H_2}) \\ &+ n_{Cu}(\varepsilon_{CuO} - G_{H_2O} + G_{H_2}) \\ &+ n_O(G_{H_2O} - G_{H_2}) + n_H\frac{1}{2}G_{H_2} \\ &+ (2n_O - 4n_{Ti} - n_H - 2n_{Cu})eU_b]\}.\end{aligned} \tag{5.14}$$

The surface free energy of Cu_2O/TiO_2 and CuO/TiO_2 in reference to Cu metal atom is:

$$\gamma_{S_k^{m(\alpha\beta\gamma)}} = \frac{1}{A}\{G - [n_{Ti}(\varepsilon_{TiO_2} - 2G_{H_2O} + 2G_{H_2}) + n_{Cu}(G_{Cu}) + n_O(G_{H_2O} - G_{H_2}) + n_H\frac{1}{2}G_{H_2} + (2n_O - 4n_{Ti} - n_H)eU_b]\}, \quad (5.15)$$

where n_{Ti}, n_{Cu}, n_O and n_H denote number of Ti, Cu, O and H atoms, respectively.

The chemical potential of the bulk TiO_2, (μ_{TiO_2}) is approximated to be equal to DFT energy per formula unit (ε_{TiO_2}). For Cu_2O and CuO nanowires, its chemical potential is approximated to be equal to DFT energy per copper atom of bulk CuO and Cu_2O, respectively, i.e ε_{Cu_2O} and ε_{CuO}. For Cu, its chemical potential is approximated to be equal to free energy of Cu metal (G_{Cu}) that is given by the DFT energy per copper atom. See Appendix B for an example on thermodynamic calculations of O* oxidation species ($S_2^{2(100)}$).

In Figs. 5.15, 5.16 and 5.17, plots of surface free energy against potential are shown for various adsorbed species on pristine TiO_2 surface, Cu_2O/TiO_2 and CuO/TiO_2, and Cu_2O/TiO_2 and CuO/TiO_2 with respect to Cu metal. The vertical dashed line indicates a U_b value of 3.25 V versus the normal hydrogen electrode (NHE) at which photogenerated holes are produced.

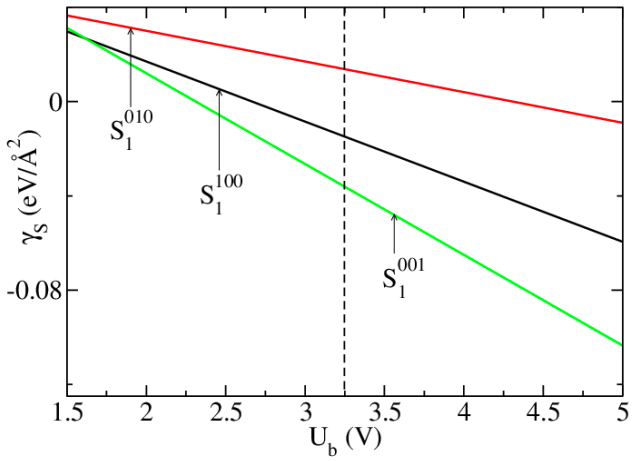

Figure 5.15: Surface free energies, γ_s (eV/Å^2) of different water oxidation species as a function of applied bias on pristine TiO_2 anatase (101) surface (see equation 5.12).

The most stable termination is S_1^{001} (green solid line) for pristine TiO_2 anatase (101)

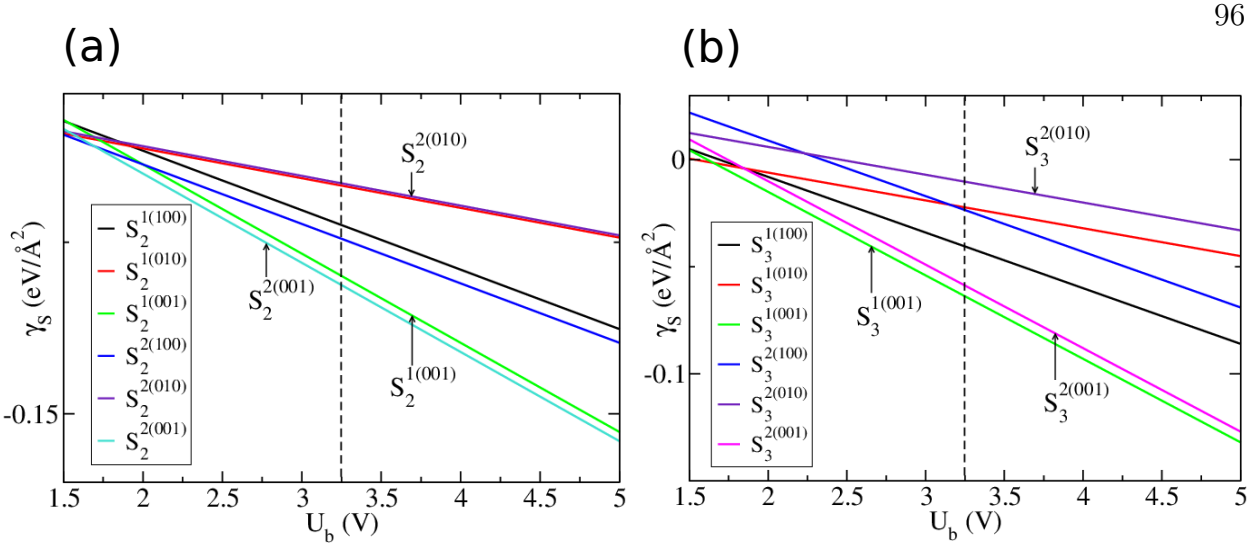

Figure 5.16: Surface free energies, γ_s (eV/Å^2) of different water oxidation species as a function of applied bias on (a) Cu_2O/TiO_2 (see equation 5.13) and (b) CuO/TiO_2 (see equation 5.14).

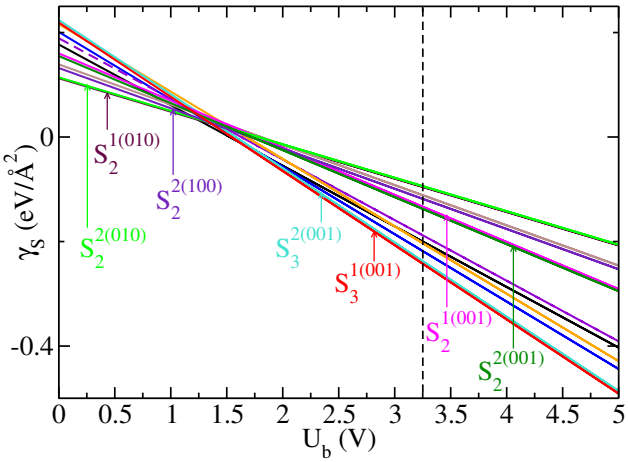

Figure 5.17: Surface free energies, γ_s (eV/Å^2) of different water oxidation species as a function of applied bias on Cu_2O/TiO_2 ($S_2^{m\ (\alpha\beta\gamma)}$) and CuO/TiO_2 ($S_3^{m\ (\alpha\beta\gamma)}$)(101) surface with bulk copper as reference. Other surface terminations not indicated are shown as: $S_3^{1(100)}$ (blue solid line), $S_3^{2(100)}$ (orange solid line), $S_3^{1(010)}$ (black solid line), $S_3^{2(010)}$ (violet solid line) and $S_2^{1(100)}$ (brown solid line), $S_2^{2(100)}$ (indigo solid line). $S_2^{1(010)}/S_2^{2(010)}$ overlap. (see equation 5.15).

surface (Fig. 5.15). The stable terminations on Cu_2O/TiO_2 surface are $S_2^{2(001)}$ (turqoise solid line) and $S_2^{1(001)}$ (green solid line) (Fig. 5.16a). Similarly, the most stable terminations for CuO/TiO_2 surface are $S_3^{1(001)}$ (green solid line) and $S_3^{2(001)}$ (magenta solid line) (Fig. 5.16b). Again, for Cu_2O and CuO on TiO_2 anatase (101) surface referenced to Cu metal, $S_3^{1(001)}$ and $S_3^{2(001)}$ termination are the most stable at effective bias (U_b= 3.25 V) and have almost equivalent stabilities (Fig. 5.17).

For each termination, the most stable configuration is that with an adsorbed OOH. At an effective bias of U_b = 3.25 V, the CuO/TiO_2 systems are more stable than the

Cu_2O/TiO_2. This is an effect of the photoelectrochemical conditions. Indeed, as already reported before (Meng'wa et al., 2017), at zero applied bias the order of stability is reversed. This is consistent with some observation that, under reaction conditions, Cu_2O experiences surficial oxidation reaction to CuO (Hou et al., 2016a).

The most stable species, OOH on CuO/TiO_2 ($S_3^{1(001)}$), is located at the bridge site between Ti and Cu atoms, indicating a possible cooperative behaviour of the two elements. The hydroperoxo is in fact the most stable species on all considered terminations. The same was found to apply to Ga_2O_3 -covered hematite (Ulman et al., 2017). On the contrary, the hydroxyl is the least stable species on most terminations.

The optimized geometries of the most stable oxidation species on pristine and copper oxides terminated TiO_2 anatase (101) surface are shown in Figs. 5.18, 5.19 and 5.20, respectively.

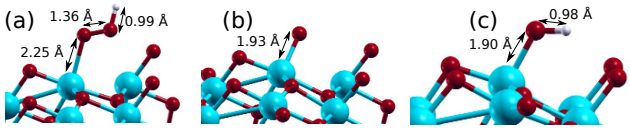

Figure 5.18: Optimized geometries of oxidation species on pristine TiO_2 anatase (101) surface arranged in decreasing order of stability: (a) $S_1^{(001)}$, (b) $S_1^{(100)}$, (c) $S_1^{(010)}$.

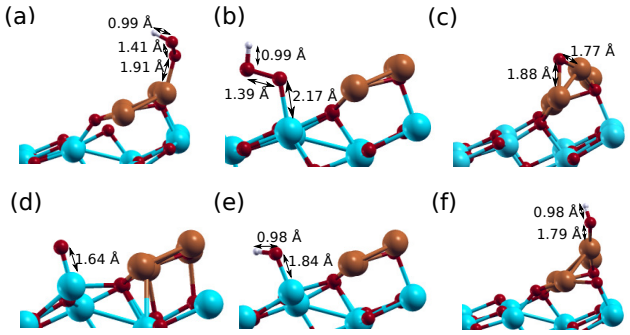

Figure 5.19: Optimized geometries of oxidation species on Cu_2O/TiO_2 anatase (101) surface arranged in decreasing order of stability: (a) $S_2^{2(001)}$, (b) $S_2^{1(001)}$, (c) $S_2^{2(100)}$, (d) $S_2^{1(100)}$, (e) $S_2^{1(010)}$, (f) $S_2^{2(010)}$.

5.3.3 Photo-Oxidation of Water

The process of water photo-oxidation proceeds through four sequential proton-coupled electron transfer steps (PCET) giving rise to the intermediate species hydroxyl (HO*), atomic oxygen (O*) and hydroperoxo (HOO*). As mentioned before, the water oxidation reaction

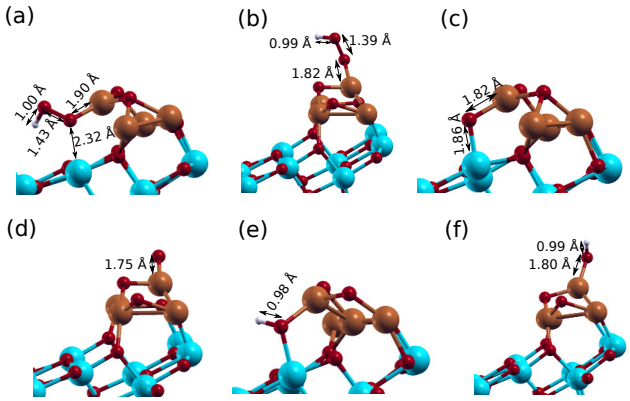

Figure 5.20: Optimized geometries of oxidation species on CuO/TiO_2 anatase (101) surface arranged in decreasing order of stability: (a) $S_3^{1(001)}$, (b) $S_3^{2(001)}$, (c) $S_3^{1(100)}$, (d) $S_3^{2(100)}$, (e) $S_3^{1(010)}$ (f) $S_3^{2(010)}$.

follows the scheme in equation 4.6, which is presented here for ease of reference:

$$\begin{aligned} 2H_2O + (^*) &\xrightarrow{A} HO^* + H_2O + H^+ + e^- \\ &\xrightarrow{B} O^* + H_2O + 2(H^+ + e^-) \\ &\xrightarrow{C} HOO^* + 3(H^+ + e^-) \\ &\xrightarrow{D} O_2 + (*) + 4(H^+ + e^-), \end{aligned}$$

where (*) is the active site on the photoanode. The reaction step labelled A denotes hydroxylation of an active site, step B is the dehydrogenation of an adsorbed hydroxyl group, step C is the formation of hydroperoxo species and step D creates the release of an O_2 molecule from the surface. This reaction path is followed in the present calculations. The potential required for water oxidation at every PCET step is 1.23 V and the net reaction free energy change is 4.92 eV at standard conditions (T=298.15 K, P= 1 bar, pH = 0). However, in a real situation, potential above 1.23 V is needed for this reaction to proceed. This additional potential is referred to as overpotential. The overpotential is calculated as follows: overpotential=max(G_A,G_B,G_C,G_D)/e - 1.23 V. The calculated overpotential is a thermodynamic quantity, determined from the differences between equilibrium states, as opposed to the kinetic barriers that exists between the states. Nevertheless, the computed overpotential compares well with measured overpotential, which takes into consideration the concentration of active sites and the current density (Man et al., 2011).

The free-energy changes (ΔG) of the water oxidation reaction steps labelled A, B, C,

and D in equation 4.6 at applied potential U and pH=0 are calculated as follows:

$$\Delta G_A = \Delta E_A + \frac{1}{2}E_{H_2} - E_{H_2O} + (\Delta ZPE - T\Delta S)_A - eU, \tag{5.16}$$

$$\Delta G_B = \Delta E_B + \frac{1}{2}E_{H_2} + (\Delta ZPE - T\Delta S)_B - eU, \tag{5.17}$$

$$\Delta G_C = \Delta E_C + \frac{1}{2}E_{H_2} - E_{H_2O} + (\Delta ZPE - T\Delta S)_C - eU, \tag{5.18}$$

$$\Delta G_D = 4.92eV + \Delta E_D - \frac{3}{2}E_{H_2} + 2E_{H_2O} + (\Delta ZPE - T\Delta S)_D - eU. \tag{5.19}$$

The values of (ΔZPE-TΔS) are presented in Table 5.11 for the reaction steps in equations 5.16 to 5.19.

Table 5.11: ΔZPE and TΔS for different reaction steps

(ΔZPE-TΔS)$_A$	0.40
(ΔZPE-TΔS)$_B$	-0.37
(ΔZPE-TΔS)$_C$	0.39
(ΔZPE-TΔS)$_D$	-0.42

The calculated reaction free energies ΔE at zero bias for each PCET step are summarised in Table 5.12.

Table 5.12: Calculated reaction energy differences $\triangle$E (eV) of different intermediates species at steps (A, B, C, D) in the water oxidation process for the pristine TiO_2, Cu_2O/TiO_2 and CuO/TiO_2 anatase (101) surface for various surface terminations.

	S_1	S_2^1	S_2^2	S_3^1	S_3^2
$\triangle E_A = E_{HO^*} - E^*$	-450.00	-451.14	-451.04	-451.88	-450.94
$\triangle E_B = E_{O^*} - E_{HO^*}$	17.26	18.21	17.59	18.10	18.41
$\triangle E_C = E_{HOO^*} - E_{O^*}$	-451.01	-451.12	-450.90	-451.20	-452.01
$\triangle E_D = E^* - E_{HOO^*}$	883.74	884.04	884.35	884.97	884.54

The DFT energy of water molecule used in the calculation is E_{H_2O} = -468.063968022 eV, while that of hydrogen molecule, E_{H_2}= -31.690430636 eV. For example, to calculate G_A for pristine TiO_2 anatase 101 surface at zero bias (see equation 5.16):

$$\begin{aligned} G_A &= -450\ eV - 15.845215318\ eV + 468.063968022\ eV + 0.40\ eV \\ &= 2.618752704\ eV \\ &= 2.62\ eV. \end{aligned} \tag{5.20}$$

The overpotential is calculated as follows: overpotential=max(G_A,G_B,G_C,G_D)/e - 1.23 V. Lets consider the case of pristine TiO_2 (101) anatase surface (see Figure 5.21):

$$\begin{aligned} \text{Overpotential} &= \max(2.62\ eV, 1.05\ eV, 1.60\ eV, -0.35\ eV)/e - 1.23\ V \\ &= 2.62\ V - 1.23\ V \\ &= 1.39\ V. \end{aligned} \tag{5.21}$$

5.3.3.1 Pristine TiO_2 anatase (101) Surface

As mentioned before, the water oxidation reaction follows the reaction path shown in equation 4.6. On TiO_2 anatase (101) surface, H_2O is split at a Ti_{5C} site resulting into the adsorption of an OH group on an active site (Ti_{5C}). The OH then loses a proton, and the remaining O forms a bond with OH group from another water molecule to form a hydroperoxo species (OOH) and another proton is subsequently released. Finally, an O_2 molecule desorbs from the surface as a proton and electron (H^++e^-) are released.

From the water oxidation cycle shown in Fig. 5.21, its clear that the overpotential determining step is the hydroxylation of the water molecule in agreement with the findings in Ref. (Li et al., 2010; Valdes et al., 2008). This reaction step has a Gibb's free energy difference of 2.62 eV. The calculated overpotential is 1.39 V, and this means that the removal of the first proton must overcome this overpotential for this process to proceed. This is in excellent agreement with a cumulative overpotential of 1.39 V of the first proton removal step, determined from an energy cost of 0.69 eV at an overpotential of 0.7 V (1.93 V vs SHE) for anatase (101) surface (Li et al., 2010). It is also in fairly good agreement with experimental overvoltage that ranged from (0.9 V- 1.1 V) for water splitting process on TiO_2 rutile crystal (Nozik, 1975) and another overpotential of 1.19 V from theoretical studies on

TiO_2 (110) rutile surface (Rossmeisl et al., 2007). The most favoured step is D, which is the last PCET step and it results into an oxygen molecule being produced.

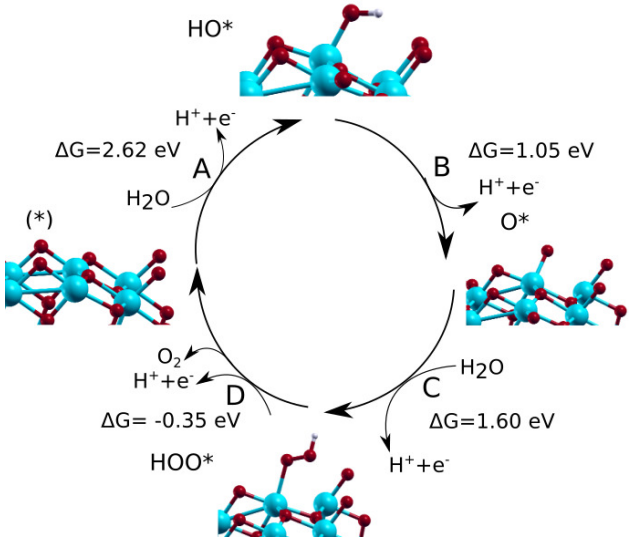

Figure 5.21: Water oxidation cycle on pristine TiO_2 anatase (101) surface (S_1). The first proton release at step A, is energetically unfavourable due to the high free energy.

Li et al. (Li et al., 2010) attributed the high overpotential of OER to the instability of the surface-adsorbed OH states after the first electron removal step. This is corroborated by the results of this study on relative stability of the water oxidation species shown in Fig. 5.15. The authors of Ref. (Li et al., 2010) investigated co-doped TiO_2 systems and noted that introduction of occupied levels above the VB of pure anatase-TiO_2 greatly enhanced OER activity. Chen et al. (Chen et al., 2013) carried out a theoretical study of the kinetics of the first PCET on TiO_2 anatase surface and found that at low pH, the overpotential determining step is proton transfer, while at high pH, PCET is almost barrier-less. The authors suggested an increase of surface Lewis activity to enhance OER activity with transition metal dopants substituting Ti_{5C} as suitable dopants to lower pK_a of the reaction.

Plotted free energy diagram at different potentials is shown in Fig. 5.22. The overpotential steps begin to go downhill in energy at a bias potential of U=2.62 V, which is the potential needed to overcome the energy demanding step. This is consistent with the experimentally determined potential of 2.6 V for direct electrochemical OH radical formation (Macounova et al., 2017) in TiO_2 anatase anodic processes.

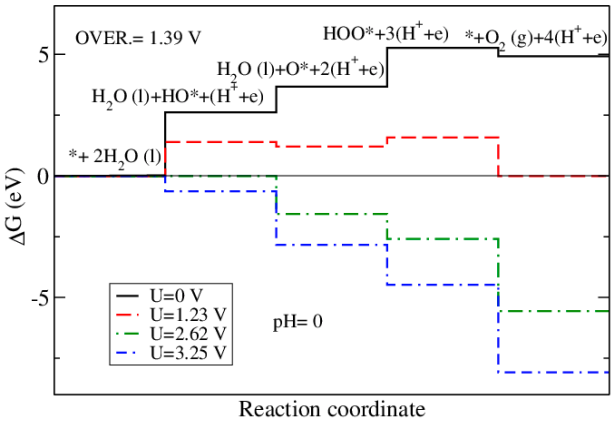

Figure 5.22: The free energies of the intermediates on pristine TiO_2 anatase (101) surface (S_1) surface termination at pH=0. At equilibrium potential U=1.23 V, most steps are still uphill in energy. All steps are downhill at U=2.62 V. OVER. is an abbreviation of overpotential.

5.3.3.2 Nanostructured Cu_2O/TiO_2 anatase (101) Surface

Water oxidation reactions were carried out at two terminations of Cu_2O/TiO_2; one at the Ti_{5C} atom (see Fig. 5.13a) and the other at a Cu atom on Cu_2O-supported TiO_2 substrate (see Fig. 5.13b). The reaction pathways are the same as those on clean TiO_2 anatase (101) surface. Calculations of water photooxidation established overpotentials of 0.77 V and 0.48 V for the two terminations, whose water oxidation cycles are shown in Figs. 5.23a and 5.23b, respectively. The overpotential-determining steps are the dehydrogenation of the adsorbed hydroxyl group and formation of the hydroperoxo (OOH) species, respectively. This is different from the overpotential-determining step (hydroxylation) for pristine anatase surface. There are many systems where these steps determine the overpotential: dehydrogenation of the hydroxyl group is responsible for overpotentials of $\sim$ 0.8 V on bare and gallium oxide-covered hematite (0001) surfaces (Ulman et al., 2017); hydroperoxo formation determines overpotentials of 0.37 V and 0.56 V on RuO_2 and IrO_2 (110) surfaces, respectively (Rossmeisl et al., 2007).

The calculated overpotentials of 0.77 V and 0.48 V represent a substantial decrease from the value of 1.39 V calculated for clean TiO_2, and the value of 0.9 V measured for copper oxide (Liu et al., 2015b). For the Ti_{5C} site, the decrease in overpotential is attributed to the presence of the copper oxide, which alters the adsorption energies of the reaction intermediates. In particular, comparing the reaction energies and configurations on pristine anatase and on this system, it is possible to observe that the key contribution of the copper

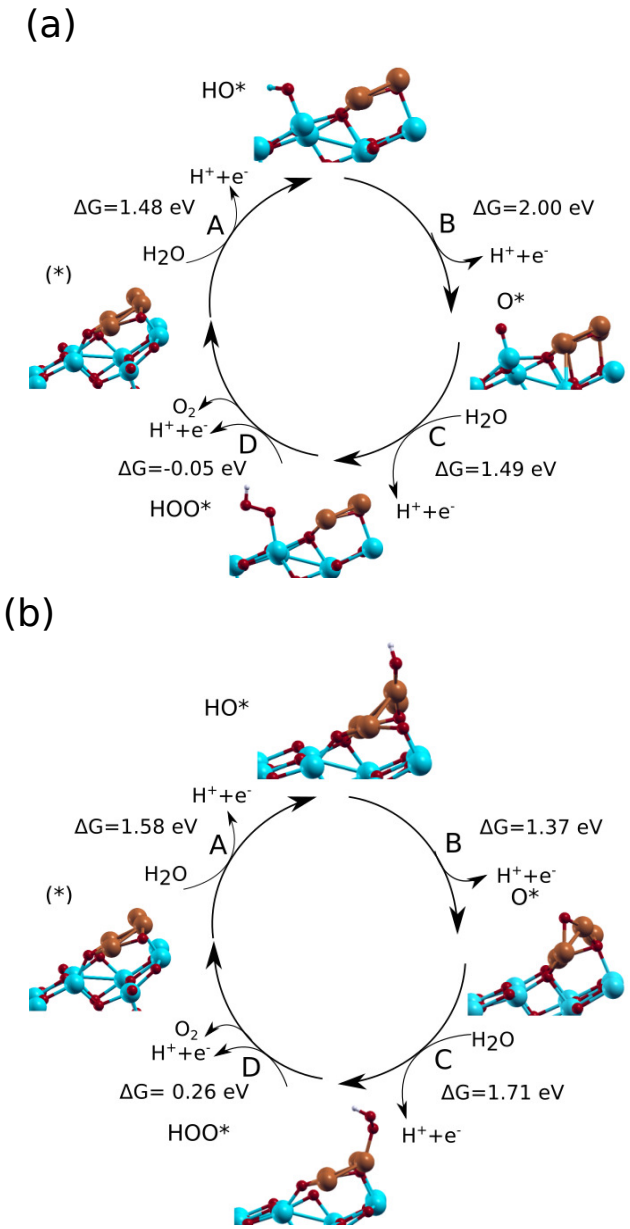

Figure 5.23: Water oxidation cycle on Cu_2O/TiO_2 anatase (101) surface (a) Water-oxidation reaction occurring at Ti_{5C} site (S_2^1), (b) Water oxidation reaction on Cu_2O covered TiO_2 (S_2^2). The free energy of 1.71 eV at step C in (b) is the lowest compared to energetics of the other overpotential determining steps of Cu oxides/TiO_2 and responsible for the reduced overpotential of 0.48 V.

oxide is to stabilize the adsorbed OH group. For the adsorption at the Ti_{5C} site, this is possible because copper modifies the geometry of this site. In fact, in the presence of Cu, the range of O_{2C} bond to two Ti atoms increased ($\sim$ 0.1 Å, and $\sim$ 0.3 Å, respectively), accordingly, the Ti_{5C}-OH bond decreased by 0.06 Å, compared to similar bond on the pristine TiO_2 surface. This indicates that OH adsorbs well at Ti_{5C} site on Cu_2O/TiO_2 surface, which is consistent with our thermodynamic studies. This assertion is further confirmed by adsorption energies of OH at Ti_{5C} site on pristine TiO_2 surface and Cu_2O/TiO_2 surface,

which are 1.42 eV and 2.56 eV, respectively.

In the case of the cycle on the Cu atom, the stronger OH adsorption is due to the low oxygen-coordination of the copper atom, bound to only one oxygen atom, i.e. to the nanostructured nature of the copper oxide. In fact, the low coordination of that copper atom is also related to the appearance of states in the band gap of TiO_2 (Meng'wa et al., 2017). As an additional effect, Cu 3d and O 2p states extending in the gap could contribute to a better photo-response (Meng'wa et al., 2017; Sharma et al., 2017), and to an enhanced electron transfer to adsorbed OH (Li et al., 2010).

The calculated overpotential of 0.48 V is comparable to that of Mn-doped TiO_2 nanowires (Liu et al., 2013a), and only higher than that of RuO_2 (0.37 V) (Rossmeisl et al., 2007), which is however a costly material. An applied bias of U= 2.0 V and U= 1.71 V for the cycles shown in Figs. 5.24a and 5.24b, respectively, is sufficient to make every step to become downhill in energy.

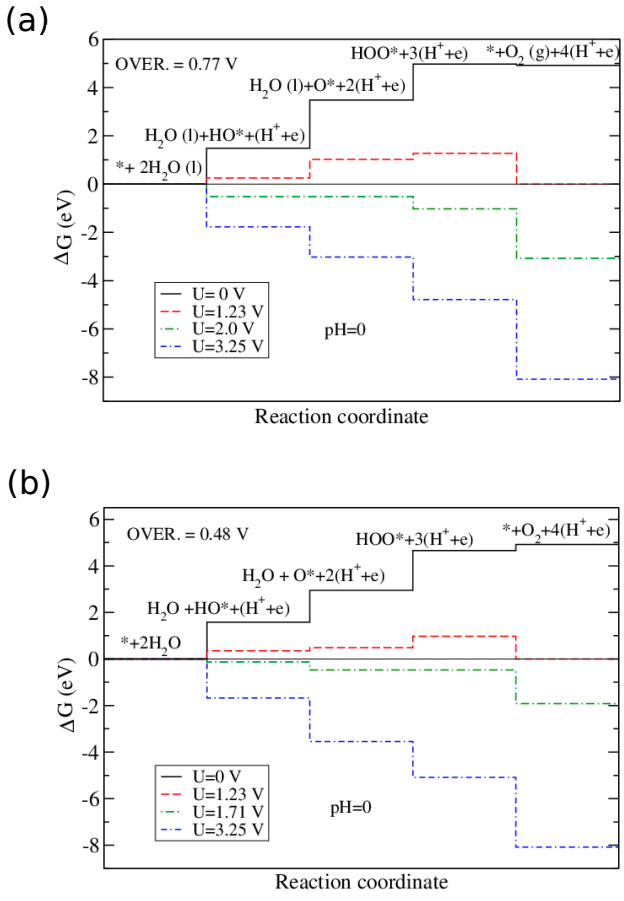

Figure 5.24: The free energies of the intermediates on Cu_2O/TiO_2 (a) S_2^1 and (b) S_2^2 surface terminations at pH=0. At equilibrium potential U=1.23 V, some steps are still uphill in energy. All steps are downhill at U=2.0 V and U=1.71 V, respectively. OVER. is an abbreviation of overpotential.

5.3.3.3 Nanostructured CuO/TiO_2 anatase (101) Surface

On this system, the catalytic cycle that was investigated comprised of the most favourable configuration with dissociative adsorbed water (Fig. 5.14a), and the cycle taking place completely on CuO (Fig. 5.14d). In the former, OH adsorbs at a bridge site between a Ti and a Cu atom, while hydrogen binds to an oxygen atom of the CuO nanostructure.

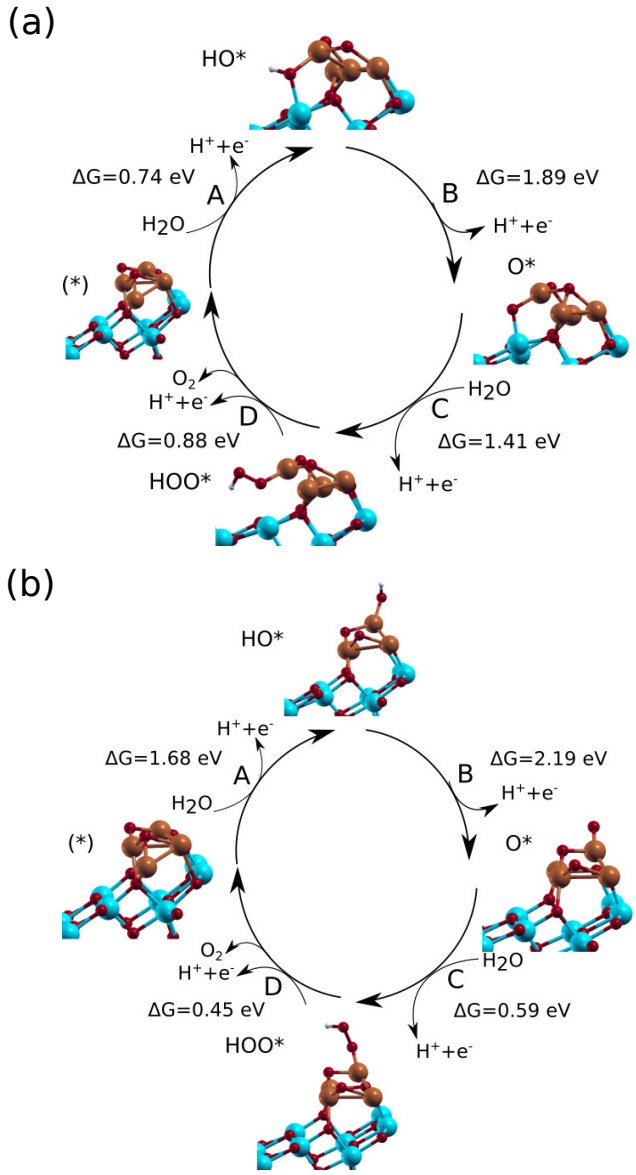

Figure 5.25: Water oxidation cycle on CuO/TiO_2 anatase (101) surface. The energetics at step B, which correspond to dehydrogenation of OH species are unfavorable. (a) Water-oxidation reaction at the interface of CuO and TiO_2 anatase surface (S_3^1), (b) Water-oxidation reaction on CuO supported by TiO_2 anatase surface (S_3^2).

The two water oxidation cycles are shown in Figs. 5.25a and 5.25b, respectively. They yield overpotentials of 0.66 V and 0.96 V, again considerably lower than the 1.39 V of clean TiO_2. The value of 0.96 V for the cycle taking place on the CuO nanostructure is in line with

the experimental value for CuO (Liu et al., 2015b). As mentioned before for Cu_2O/TiO_2, the presence of filled CuO states at the top of the valence band of CuO/TiO_2 electronic structure contributed to the decreased overpotential (Meng'wa et al., 2017; Sharma et al., 2017; Li et al., 2010).

At both sites, the overpotential-determining step is the dehydrogenation of the adsorbed hydroxyl group, again at variance from what happens at the pristine anatase surface. The free energies of the steps demanding more potential are 1.89 eV and 2.19 eV, respectively. As such, for these reactions to be on the downhill, potentials of 1.89 V and 2.19 V, respectively are needed as shown in the free energy diagrams (see Figs. 5.26a and 5.26b).

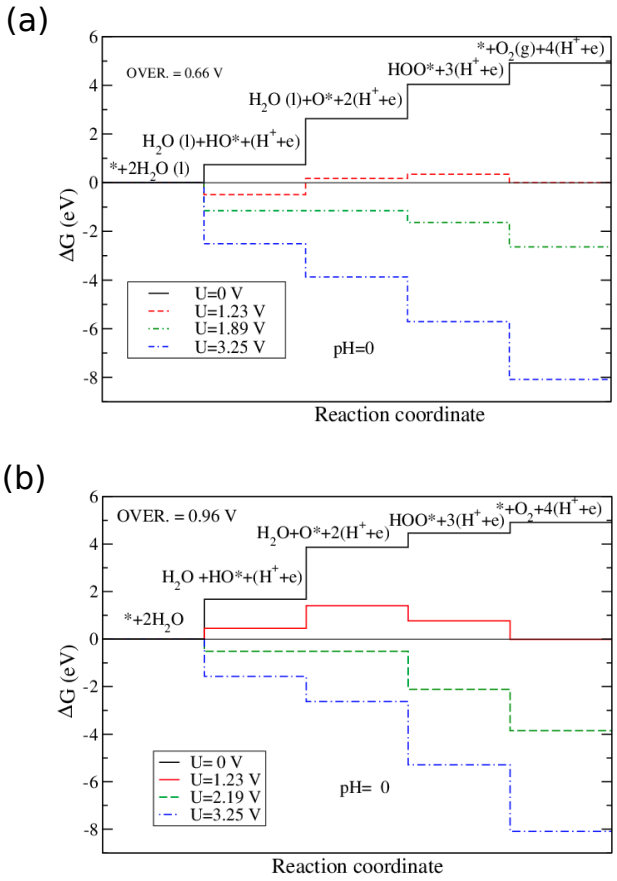

Figure 5.26: The free energies of the intermediates on CuO/TiO_2 (a) S_3^1 and (b) S_3^2 surface terminations at pH=0. At equilibrium potential U=1.23 V, some steps are still uphill in energy. All steps are downhill at U=1.89 V and U=2.19 V, respectively. OVER. is an abbreviation of overpotential.

CHAPTER SIX

CONCLUSIONS AND RECOMMENDATIONS

6.1 Conclusions

Copper oxides nanostructures deposited on TiO_2 anatase (101) surface were investigated by density functional theory and ab-initio thermodynamics. The Cu_2O nanowires were found to be more stable than clusters with the same stoichiometry, and than all CuO structures. This is at variance from the case of bulk oxides, where CuO is more stable at room temperature conditions. The triangular frameworks of Cu_2O and Cu_3 trimer are dominant across all Cu oxides/TiO_2 structures and may have stabilized the coupled metal oxide systems. The atomic configurations of the low-energy structures are quite different from their bulk counterparts: in the Cu_2O structures, the average of Cu-Cu bond lengths (2.536 Å) are in very good agreement to that of experimental bulk metal copper (2.54 Å), while Cu-O bond lengths differed by ∼0.1 Å from those of bulk Cu_2O. In the most stable structure, there is no direct Cu-Ti bond.

The copper oxide nanostructures display filled electronic states (Cu 3d and O 2p) that extend from the upper valence band into the band gap of titania, thereby decreasing the band gap of the system by over 1 eV, thereby extending titania photoabsorption into the visible range. The lowest-lying empty states belong to titania (Ti 3d) in the case of the Cu_2O nanowire, and to CuO (Cu 3d and O 2p) in the case of the CuO nanowire. This suggests that the Cu_2O nanostructures should favour hole transfer from titania to the copper oxide, while keeping photoexcited electrons in TiO_2. This contributes to charge separation and hence suppressing recombination. On the contrary, on the CuO nanostructures also the photoexcited electrons should be transferred to the copper oxide. The Lowdin analysis from the PDOS of our ground state calculations demonstrate absence of charge transfer between the copper oxide nanowires and the TiO_2 (101) anatase surface. The formation of polaronic state Ti^{3+} in the proximity of the Cu_2O/TiO_2 nanowire is expected to enhance photoresponse of TiO_2 in the visible range of the light spectrum.

This work has also investigated the energetics of photoelectrocatalytic oxidation of water on the TiO_2 anatase (101) surface modified by copper oxides, by means of density functional

theory (DFT). The overpotentials for this reaction amount to 0.48 V for Cu_2O/TiO_2 (S_2^2), which is a 65 % decrease and 0.66 V for CuO/TiO_2 (S_3^1), which is a 52.52 % decreasea, a sharp decrease with respect to pristine titania (1.39 V). The main reason for this improvement is the stronger adsorption of hydroxyl (OH) on the copper-modified systems. This also reflects in the nature of the overpotential-determining step: on the pristine surface, it is the hydroxyl formation, while on the other systems considered here it is the dehydrogenation of adsorbed hydroxyl group except for the Cu_2O/TiO_2 (S_2^2), which was at the formation of the hydoroperoxo species. There is however a difference between the two oxides at zero electric bias with regard to water adsorption, molecular water adsorption at Ti_{5C} site prevails in the presence of Cu_2O and partially dissociative adsorption is favoured at the interface of CuO and TiO_2 with OH at the bridge site between Ti and Cu, the other H is bonded to O on CuO.

Finally, this study has shown that, under photoelectrochemical conditions, the CuO system becomes more stable than the Cu_2O, contrary to what happens in absence of an electric bias. Therefore, CuO will most likely be present under photoelectrochemical reaction conditions.

This work shows that there is a synergetic effect arising from the addition of nanostructured copper oxide to titania, leading to an improvement of the energetics of the reaction and to a subsequent lowering of the overpotential. The calculated overpotential is among the lowest overpotentials for this reaction, and is obtained with cheap and safe materials.

6.2 Recommendations

The energetics of these calculations were determined at ground state and under vacuum conditions, therefore, its recommended that theoretical studies including effects of finite temperature fluctuations and realistic environments are necessary to bring closer contact with applications and experiments. In that regard, its proposed that first principle molecular dynamics (FPMD) of most stable nanostructured Cu_2O/TiO_2 and CuO/TiO_2 in aqueous environment be performed to determine the kinetics and chemical processes of the coupled photocatalyst. Furthermore, experiments on copper oxide-modified titania in liquid water under controlled conditions of illumination and bias would be necessary to test our cal-

culations. Since Cu_2O/TiO_2 and CuO/TiO_2 photocatalysts can find applications in CO_2 reduction, theoretical and experimental studies of CO_2 photoreduction on the most stable nanostructured copper oxide-modified titania photocatalytic systems are highly recommended.

REFERENCES

Allen, S. E., Walvoord, R. R., Padilla-Salinas, R., and Kozlowski, M. C. (2013). Aerobic copper-catalyzed organic reactions. *Chemical Reviews*, 113(8):6234–6458.

Andersson, K., Gómez, A., Glover, C., Nordlund, D., Öström, H., Schiros, T., Takahashi, O., Ogasawara, H., Pettersson, L., and Nilsson, A. (2005). Molecularly intact and dissociative adsorption of water on clean Cu (110): A comparison with the water/Ru (001) system. *Surface Science*, 585(3):L183–L189.

Anisimov, V. I., Solovyev, I., Korotin, M., Czyżyk, M., and Sawatzky, G. (1993). Density-functional theory and NiO photoemission spectra. *Physical Review B*, 48(23):16929.

Anisimov, V. I., Zaanen, J., and Andersen, O. K. (1991). Band theory and mott insulators: Hubbard U instead of stoner I. *Physical Review B*, 44(3):943.

Anpo, M., Chiba, K., Tomonari, M., Coluccia, S., Che, M., and Fox, M. A. (1991). Photocatalysis on native and platinum-loaded TiO_2 and ZnO catalysts-origin of different reactivities on wet and dry metal oxides. *Bulletin of the Chemical Society of Japan*, 64(2):543–551.

Asahi, R., Morikawa, T., Ohwaki, T., Aoki, K., and Taga, Y. (2001). Visible-light photocatalysis in nitrogen-doped titanium oxides. *Science*, 293(5528):269–271.

Asahi, R., Taga, Y., Mannstadt, W., and Freeman, A. J. (2000). Electronic and optical properties of anatase TiO_2. *Physical Review B*, 61(11):7459.

Åsbrink, S. and Norrby, L.-J. (1970). A refinement of the crystal structure of copper (ii) oxide with a discussion of some exceptional esd's. *Acta Crystallographica Section B: Structural Crystallography and Crystal Chemistry*, 26(1):8–15.

Ayyub, P., Palkar, V., Chattopadhyay, S., and Multani, M. (1995). Effect of crystal size reduction on lattice symmetry and cooperative properties. *Physical Review B*, 51(9):6135.

Bader, R. (1990). Atoms in molecules: A quantum theory: Oxford univ. press.

Bai, S., Ge, J., Wang, L., Gong, M., Deng, M., Kong, Q., Song, L., Jiang, J., Zhang, Q., Luo, Y., et al. (2014). A unique semiconductor–metal–graphene stack design to harness charge flow for photocatalysis. *Advanced Materials*, 26(32):5689–5695.

Baishya, K., Idrobo, J. C., Öğüt, S., Yang, M., Jackson, K. A., and Jellinek, J. (2011). First-principles absorption spectra of Cu_n (n= 2-20) clusters. *Physical Review B*, 83(24):245402.

Bandara, J., Udawatta, C., and Rajapakse, C. (2005). Highly stable CuO incorporated TiO_2 catalyst for photocatalytic hydrogen production from H_2O. *Photochemical & Photobiological Sciences*, 4(11):857–861.

Banfield, J. et al. (1998). Thermodynamic analysis of phase stability of nanocrystalline titania. *Journal of Materials Chemistry*, 8(9):2073–2076.

Barreca, D., Carraro, G., Gombac, V., Gasparotto, A., Maccato, C., Fornasiero, P., and Tondello, E. (2011). Supported metal oxide nanosystems for hydrogen photogeneration: Quo vadis? *Advanced Functional Materials*, 21(14):2611–2623.

Bennett, R. (2000). The re-oxidation of the substoichiometric TiO_2 (110) surface in the presence of crystallographic shear planes. *PhysChemComm*, 3(3):9–14.

Berger, T., Sterrer, M., Diwald, O., Knözinger, E., Panayotov, D., Thompson, T. L., and Yates, J. T. (2005). Light-induced charge separation in anatase TiO_2 particles. *The Journal of Physical Chemistry B*, 109(13):6061–6068.

Bessekhouad, Y., Robert, D., and Weber, J.-V. (2005). Photocatalytic activity of Cu_2O/TiO_2, Bi_2O_3/TiO_2 and $ZnMn_2O_4/TiO_2$ heterojunctions. *Catalysis Today*, 101(3-4):315–321.

Bhanushali, S., Ghosh, P., Ganesh, A., and Cheng, W. (2015). 1d copper nanostructures: progress, challenges and opportunities. *Small*, 11(11):1232–1252.

Bredow, T. and Jug, K. (1995a). Sindo1 study of photocatalytic formation and reactions of OH radicals at anatase particles. *The Journal of Physical Chemistry*, 99(1):285–291.

Bredow, T. and Jug, K. (1995b). Theoretical investigation of water adsorption at rutile and anatase surfaces. *Surface Science*, 327(3):398–408.

Bruneval, F., Vast, N., Reining, L., Izquierdo, M., Sirotti, F., and Barrett, N. (2006). Exchange and correlation effects in electronic excitations of Cu_2O. *Physical Review Letters*, 97(26):267601.

Camellone, M. F., Kowalski, P. M., and Marx, D. (2011). Ideal, defective, and gold-promoted rutile TiO_2 (110) surfaces interacting with CO, H_2, and H_2O: Structures, energies, thermodynamics, and dynamics from PBE+U. *Physical Review B*, 84(3):035413.

Cargnello, M., Gasparotto, A., Gombac, V., Montini, T., Barreca, D., and Fornasiero, P. (2011). Photocatalytic H_2 and added-value by-products–the role of metal oxide systems in their synthesis from oxygenates. *European Journal of Inorganic Chemistry*, 2011(28):4309–4323.

Carneiro, J. T., Savenije, T. J., Moulijn, J. A., and Mul, G. (2009). Toward a physically sound structure-activity relationship of TiO_2-based photocatalysts. *The Journal of Physical Chemistry C*, 114(1):327–332.

Carneiro, J. T., Savenije, T. J., Moulijn, J. A., and Mul, G. (2011). How phase composition influences optoelectronic and photocatalytic properties of TiO_2. *The Journal of Physical Chemistry C*, 115(5):2211–2217.

Celli, V., Tully, J., Schönhammer, K., Gunnarsson, O., Gadzuk, J., Hood, E., Langreth, H. M. D., and Suhl, H. (1984). Many body phenomena at surfaces. *Academic, Orlando*.

Chan, G. H., Zhao, J., Hicks, E. M., Schatz, G. C., and Van Duyne, R. P. (2007). Plasmonic properties of copper nanoparticles fabricated by nanosphere lithography. *Nano Letters*, 7(7):1947–1952.

Chen, B.-R., Nguyen, V.-H., Wu, J. C., Martin, R., and Kočí, K. (2016). Production of renewable fuels by the photohydrogenation of CO_2: effect of the Cu species loaded onto TiO_2 photocatalysts. *Physical Chemistry Chemical Physics*, 18(6):4942–4951.

Chen, J., Li, Y.-F., Sit, P., and Selloni, A. (2013). Chemical dynamics of the first proton-coupled electron transfer of water oxidation on TiO_2 anatase. *Journal of the American Chemical Society*, 135(50):18774–18777.

Chen, L., Zhang, Q., Zhang, Y., Li, W. Z., Han, B., Zhou, C., Wu, J., Forrey, R. C., Garg, D., and Cheng, H. (2010a). A first principles study of water dissociation on small copper clusters. *Physical Chemistry Chemical Physics*, 12(33):9845–9851.

Chen, X. and Mao, S. S. (2007). Titanium dioxide nanomaterials: synthesis, properties, modifications, and applications. *Chemical Reviews*, 107(7):2891–2959.

Chen, X., Shen, S., Guo, L., and Mao, S. S. (2010b). Semiconductor-based photocatalytic hydrogen generation. *Chemical Reviews*, 110(11):6503–6570.

Clarizia, L., Spasiano, D., Di Somma, I., Marotta, R., Andreozzi, R., and Dionysiou, D. D. (2014). Copper modified-TiO_2 catalysts for hydrogen generation through photoreforming of organics. A short review. *International Journal of Hydrogen Energy*, 39(30):16812–16831.

Cococcioni, M. and De Gironcoli, S. (2005). Linear response approach to the calculation of the effective interaction parameters in the LDA+ U method. *Physical Review B*, 71(3):035105.

Cohen, M. L. and Heine, V. (1970). The fitting of pseudopotentials to experimental data and their subsequent application. In *Solid State Physics*, volume 24, pages 37–248.

Cowan, A. J. and Durrant, J. R. (2013). Long-lived charge separated states in nanostructured semiconductor photoelectrodes for the production of solar fuels. *Chemical Society Reviews*, 42(6):2281–2293.

Cowan, A. J., Tang, J., Leng, W., Durrant, J. R., and Klug, D. R. (2010). Water splitting by nanocrystalline TiO_2 in a complete photoelectrochemical cell exhibits efficiencies limited by charge recombination. *The Journal of Physical Chemistry C*, 114(9):4208–4214.

Crespo, Y. and Seriani, N. (2014). A lithium peroxide precursor on the α-MnO_2 (100) surface. *Journal of Materials Chemistry A*, 2(39):16538–16546.

Currao, A. (2007). Photoelectrochemical water splitting. *CHIMIA International Journal for Chemistry*, 61(12):815–819.

Daniel, M.-C. and Astruc, D. (2004). Gold nanoparticles: assembly, supramolecular chemistry, quantum-size-related properties, and applications toward biology, catalysis, and nanotechnology. *Chemical Reviews*, 104(1):293–346.

Dau, H., Limberg, C., Reier, T., Risch, M., Roggan, S., and Strasser, P. (2010). The mechanism of water oxidation: from electrolysis via homogeneous to biological catalysis. *ChemCatChem*, 2(7):724–761.

De Angelis, F., Di Valentin, C., Fantacci, S., Vittadini, A., and Selloni, A. (2014). Theoretical studies on anatase and less common TiO_2 phases: bulk, surfaces, and nanomaterials. *Chemical Reviews*, 114(19):9708–9753.

de Brito, J. F., Tavella, F., Genovese, C., Ampelli, C., Zanoni, M. V. B., Centi, G., and Perathoner, S. (2018). Role of CuO in the modification of the photocatalytic water splitting behavior of TiO_2 nanotube thin films. *Applied Catalysis B: Environmental*, 224:136–145.

DeSario, P. A., Pietron, J. J., Brintlinger, T. H., McEntee, M., Parker, J. F., Baturina, O., Stroud, R. M., and Rolison, D. R. (2017). Oxidation-stable plasmonic copper nanoparticles in photocatalytic TiO_2 nanoarchitectures. *Nanoscale*, 9(32):11720–11729.

Di Valentin, C. (2016). A mechanism for the hole-mediated water photooxidation on TiO_2 (101) surfaces. *Journal of Physics: Condensed Matter*, 28(7):074002.

Di Valentin, C., Pacchioni, G., and Selloni, A. (2006). Electronic structure of defect states in hydroxylated and reduced rutile TiO_2 (110) surfaces. *Physical Review Letters*, 97(16):166803.

Di Valentin, C. and Selloni, A. (2011). Bulk and surface polarons in photoexcited anatase TiO_2. *The Journal of Physical Chemistry Letters*, 2(17):2223–2228.

Diebold, U. (2003). The surface science of titanium dioxide. *Surface Science Reports*, 48(5-8):53–229.

Diesen, V. and Jonsson, M. (2014). Formation of H_2O_2 in TiO_2 photocatalysis of oxygenated and deoxygenated aqueous systems: A probe for photocatalytically produced hydroxyl radicals. *The Journal of Physical Chemistry C*, 118(19):10083–10087.

Dill, K. A. and Bromberg, S. (2003). Molecular driving forces, garland science.

Dongliang, H., Jiahai, H., Long, Q., Jiangrui, P., and Zhenji, S. (2015). Optical and photocatalytic properties of Cu-Cu_2O/TiO_2 two-layer nanocomposite films on Si substrates. *Rare Metal Materials and Engineering*, 44(8):1888–1893.

Dudarev, S., Botton, G., Savrasov, S., Humphreys, C., and Sutton, A. (1998). Electron-energy-loss spectra and the structural stability of nickel oxide: An LSDA+U study. *Physical Review B*, 57(3):1505.

Eagles, D. (1964). Polar modes of lattice vibration and polaron coupling constants in rutile (TiO_2). *Journal of Physics and Chemistry of Solids*, 25(11):1243–1251.

Ekuma, C., Anisimov, V., Moreno, J., and Jarrell, M. (2014). Electronic structure and spectra of CuO. *The European Physical Journal B*, 87(1):23.

Elliott, D. (2016). A balancing act for renewables. *Nature Energy*, 1:15003.

Emeline, A., Ryabchuk, V., and Serpone, N. (2005). Dogmas and misconceptions in heterogeneous photocatalysis. some enlightened reflections. *The Journal of Physical Chemistry B*, 109(39):18515–18521.

Fang, B., Xing, Y., Bonakdarpour, A., Zhang, S., and Wilkinson, D. P. (2015). Hierarchical CuO–TiO_2 hollow microspheres for highly efficient photodriven reduction of CO_2 to CH_4. *ACS Sustainable Chemistry & Engineering*, 3(10):2381–2388.

Foo, W. J., Zhang, C., and Ho, G. W. (2013). Non-noble metal Cu-loaded TiO_2 for enhanced photocatalytic H_2 production. *Nanoscale*, 5(2):759–764.

Forsyth, J., Brown, P., and Wanklyn, B. (1988). Magnetism in cupric oxide. *Journal of Physics C: Solid State Physics*, 21(15):2917.

Frank, S. N. and Bard, A. J. (1977). Heterogeneous photocatalytic oxidation of cyanide ion in aqueous solutions at titanium dioxide powder. *Journal of the American Chemical Society*, 99(1):303–304.

Fronzi, M., Daly, W., and Nolan, M. (2016a). Reactivity of metal oxide nanocluster modified rutile and anatase TiO_2: Oxygen vacancy formation and CO_2 interaction. *Applied Catalysis A: General*, 521:240–249.

Fronzi, M., Iwaszuk, A., Lucid, A., and Nolan, M. (2016b). Metal oxide nanocluster-modified TiO_2 as solar activated photocatalyst materials. *Journal of Physics: Condensed Matter*, 28(7):074006.

Fronzi, M. and Nolan, M. (2017). Surface modification of perfect and hydroxylated TiO_2 rutile (110) and anatase (101) with chromium oxide nanoclusters. *ACS Omega*, 2(10):6795–6808.

Fujishima, A. and Honda, K. (1972). Electrochemical photolysis of water at a semiconductor electrode. *Nature*, 238(5358):37.

Fujishima, A., Rao, T. N., and Tryk, D. A. (2000). Titanium dioxide photocatalysis. *Journal of Photochemistry and Photobiology C: Photochemistry Reviews*, 1(1):1–21.

Furube, A., Asahi, T., Masuhara, H., Yamashita, H., and Anpo, M. (2001). Direct observation of a picosecond charge separation process in photoexcited platinum-loaded TiO_2 particles by femtosecond diffuse reflectance spectroscopy. *Chemical Physics Letters*, 336(5-6):424–430.

Ganduglia-Pirovano, M. V., Hofmann, A., and Sauer, J. (2007). Oxygen vacancies in transition metal and rare earth oxides: Current state of understanding and remaining challenges. *Surface Science Reports*, 62(6):219–270.

Gao, M., Zhu, L., Ong, W. L., Wang, J., and Ho, G. W. (2015). Structural design of TiO_2-based photocatalyst for H_2 production and degradation applications. *Catalysis Science & Technology*, 5(10):4703–4726.

Gawande, M. B., Goswami, A., Felpin, F.-X., Asefa, T., Huang, X., Silva, R., Zou, X., Zboril, R., and Varma, R. S. (2016). Cu and Cu-based nanoparticles: synthesis and applications in catalysis. *Chemical Reviews*, 116(6):3722–3811.

Giannozzi, P., Baroni, S., Bonini, N., Calandra, M., Car, R., Cavazzoni, C., Ceresoli, D., Chiarotti, G. L., Cococcioni, M., Dabo, I., et al. (2009). QUANTUM ESPRESSO: a modular and open-source software project for quantum simulations of materials. *Journal of Physics: Condensed Matter*, 21(39):395502.

Gombac, V., Sordelli, L., Montini, T., Delgado, J. J., Adamski, A., Adami, G., Cargnello, M., Bernal, S., and Fornasiero, P. (2009). CuO_x-TiO_2 photocatalysts for H_2 production from ethanol and glycerol solutions. *The Journal of Physical Chemistry A*, 114(11):3916–3925.

Görling, A. (1996). Density-functional theory for excited states. *Physical Review A*, 54(5):3912.

Grondahl, L. O. (1933). The copper-cuprous-oxide rectifier and photoelectric cell. *Reviews of Modern Physics*, 5(2):141.

Grüning, M., Marini, A., and Rubio, A. (2006). Density functionals from many-body perturbation theory: The band gap for semiconductors and insulators. *The Journal of Chemical Physics*, 124(15):154108.

Halmann, M. (1978). Photoelectrochemical reduction of aqueous carbon dioxide on p-type gallium phosphide in liquid junction solar cells. *Nature*, 275(5676):115.

Hamann, D., Schlüter, M., and Chiang, C. (1979). Norm-conserving pseudopotentials. *Physical Review Letters*, 43(20):1494.

Han, S., Chen, H.-Y., Chu, Y.-B., and Shih, H. C. (2005). Phase transformations in copper oxide nanowires. *Journal of Vacuum Science & Technology B: Microelectronics and Nanometer Structures Processing, Measurement, and Phenomena*, 23(6):2557–2560.

Hartmann Douma, D. and Gebauer, R. (2011). Optical properties of dye sensitized TiO_2 nanowires from time-dependent density functional theory. *Physica Status Solidi (RRL)-Rapid Research Letters*, 5(8):259–261.

Hashimoto, K., Irie, H., and Fujishima, A. (2005). TiO_2 photocatalysis: a historical overview and future prospects. *Japanese Journal of Applied Physics*, 44(12):8269.

Heinemann, M., Eifert, B., and Heiliger, C. (2013). Band structure and phase stability of the copper oxides Cu_2O, CuO, and Cu_4O_3. *Physical Review B*, 87(11):115111.

Henderson, M. A. (2011). A surface science perspective on TiO_2 photocatalysis. *Surface Science Reports*, 66(6-7):185–297.

Henrich, V. E. and Cox, P. A. (1996). *The Surface Science of Metal Oxides*. Cambridge university press.

Herman, G. S., Dohnalek, Z., Ruzycki, N., and Diebold, U. (2003). Experimental investigation of the interaction of water and methanol with anatase -TiO_2 (101). *The Journal of Physical Chemistry B*, 107(12):2788–2795.

Himmetoglu, B., Wentzcovitch, R. M., and Cococcioni, M. (2011). First-principles study of electronic and structural properties of CuO. *Physical Review B*, 84(11):115108.

Hirai, T., Suzuki, K., and Komasawa, I. (2001). Preparation and photocatalytic properties of composite CdS nanoparticles–titanium dioxide particles. *Journal of Colloid and Interface Science*, 244(2):262–265.

Hirano, K., Inoue, K., and Yatsu, T. (1992). Photocatalysed reduction of CO_2 in aqueous TiO_2 suspension mixed with copper powder. *Journal of Photochemistry and Photobiology A: Chemistry*, 64(2):255–258.

Hoffmann, M. R., Martin, S. T., Choi, W., and Bahnemann, D. W. (1995). Environmental applications of semiconductor photocatalysis. *Chemical Reviews*, 95(1):69–96.

Hohenberg, P. and Kohn, W. (1964). Inhomogeneous electron gas. *Physical Review*, 136(3B):B864.

Hou, C.-C., Fu, W.-F., and Chen, Y. (2016a). Self-supported Cu-based nanowire arrays as noble-metal-free electrocatalysts for oxygen evolution. *ChemSusChem*, 9(16):2069–2073.

Hou, H., Shang, M., Gao, F., Wang, L., Liu, Q., Zheng, J., Yang, Z., and Yang, W. (2016b). Highly efficient photocatalytic hydrogen evolution in ternary hybrid TiO_2/CuO/Cu

thoroughly mesoporous nanofibers. *ACS Applied Materials & Interfaces*, 8(31):20128–20137.

Hou, W. and Cronin, S. B. (2013). A review of surface plasmon resonance-enhanced photocatalysis. *Advanced Functional Materials*, 23(13):1612–1619.

Huang, L., Peng, F., Wang, H., Yu, H., and Li, Z. (2009). Preparation and characterization of Cu_2O/TiO_2 nano–nano heterostructure photocatalysts. *Catalysis Communications*, 10(14):1839–1843.

Hush, N. (1961). Adiabatic theory of outer sphere electron-transfer reactions in solution. *Transactions of the Faraday Society*, 57:557–580.

Hwang, I., Baek, M., and Yong, K. (2015). Core/shell structured TiO_2/CdS electrode to enhance the light stability of perovskite solar cells. *ACS Applied Materials & Interfaces*, 7(50):27863–27870.

Imanishi, A., Okamura, T., Ohashi, N., Nakamura, R., and Nakato, Y. (2007). Mechanism of water photooxidation reaction at atomically flat TiO_2 (rutile)(110) and (100) surfaces: Dependence on solution pH. *Journal of the American Chemical Society*, 129(37):11569–11578.

Ingram, D. B. and Linic, S. (2011). Water splitting on composite plasmonic-metal/semiconductor photoelectrodes: evidence for selective plasmon-induced formation of charge carriers near the semiconductor surface. *Journal of the American Chemical Society*, 133(14):5202–5205.

Irie, H., Kamiya, K., Shibanuma, T., Miura, S., Tryk, D. A., Yokoyama, T., and Hashimoto, K. (2009). Visible light-sensitive Cu (II)-grafted TiO_2 photocatalysts: activities and x-ray absorption fine structure analyses. *The Journal of Physical Chemistry C*, 113(24):10761–10766.

Islam, M. S. and Fisher, C. A. (2014). Lithium and sodium battery cathode materials: computational insights into voltage, diffusion and nanostructural properties. *Chemical Society Reviews*, 43(1):185–204.

Iwaszuk, A., Lucid, A. K., Razeeb, K. M., and Nolan, M. (2014). First principles investigation of anion-controlled red shift in light absorption in ZnX (X= O, S, Se) nanocluster modified rutile TiO_2. *Journal of Materials Chemistry A*, 2(44):18796–18805.

Iwaszuk, A. and Nolan, M. (2011). Reactivity of sub 1 nm supported clusters:(TiO_2)n clusters supported on rutile TiO_2 (110). *Physical Chemistry Chemical Physics*, 13(11):4963–4973.

Iwaszuk, A. and Nolan, M. (2013). SnO-nanocluster modified anatase TiO_2 photocatalyst: exploiting the Sn (II) lone pair for a new photocatalyst material with visible light absorption and charge carrier separation. *Journal of Materials Chemistry A*, 1(22):6670–6677.

Iwaszuk, A., Nolan, M., Jin, Q., Fujishima, M., and Tada, H. (2013). Origin of the visible-light response of nickel (II) oxide cluster surface modified titanium (iv) dioxide. *The Journal of Physical Chemistry C*, 117(6):2709–2718.

Iwata, K., Takaya, T., Hamaguchi, H.-o., Yamakata, A., Ishibashi, T.-a., Onishi, H., and Kuroda, H. (2004). Carrier dynamics in TiO_2 and Pt/TiO_2 powders observed by femtosecond time-resolved near-infrared spectroscopy at a spectral region of 0.9-1.5 μm with the direct absorption method. *The Journal of Physical Chemistry B*, 108(52):20233–20239.

Jadraque, M. and Martín, M. (2008). DFT calculations of clusters: Evidence for Cu_2O building blocks. *Chemical Physics Letters*, 456(1):51–54.

Jagminas, A., Kovger, J., Rėza, A., Niaura, G., Juodkazytė, J., Selskis, A., Kondrotas, R., Šebeka, B., and Vaičiūnienė, J. (2014). Decoration of the TiO_2 nanotube arrays with copper suboxide by AC treatment. *Electrochimica Acta*, 125:516–523.

Janczarek, M. and Kowalska, E. (2017). On the origin of enhanced photocatalytic activity of copper-modified titania in the oxidative reaction systems. *Catalysts*, 7(11):317.

Jena, P., Khanna, S., and Rao, B. (2013). *Physics and chemistry of finite systems: from clusters to crystals*, volume 374. Springer Science & Business Media.

Jiang, Y., Yuan, H., and Chen, H. (2015). Enhanced visible light photocatalytic activity of Cu_2O via cationic–anionic passivated codoping. *Physical Chemistry Chemical Physics*, 17(1):630–637.

Jin, Q., Fujishima, M., Iwaszuk, A., Nolan, M., and Tada, H. (2013). Loading effect in copper (II) oxide cluster-surface-modified titanium (IV) oxide on visible-and uv-light activities. *The Journal of Physical Chemistry C*, 117(45):23848–23857.

Jones, R. O. and Gunnarsson, O. (1989). The density functional formalism, its applications and prospects. *Reviews of Modern Physics*, 61(3):689.

Jung, M., Scott, J., Ng, Y. H., Jiang, Y., and Amal, R. (2014). CuO_x dispersion and reducibility on TiO_2 and its impact on photocatalytic hydrogen evolution. *International Journal of Hydrogen Energy*, 39(24):12499–12506.

Kamat, P. V. (2012). Manipulation of charge transfer across semiconductor interface. a criterion that cannot be ignored in photocatalyst design. *The Journal of Physical Chemistry Letters*, 3(5):663–672.

Kanninen, P., Johans, C., Merta, J., and Kontturi, K. (2008). Influence of ligand structure on the stability and oxidation of copper nanoparticles. *Journal of Colloid and Interface Science*, 318(1):88–95.

Katoh, R. and Furube, A. (2011). Tunneling-type charge recombination in nanocrystalline TiO_2 films at low temperature. *The Journal of Physical Chemistry Letters*, 2(15):1888–1891.

Kavan, L., Grätzel, M., Gilbert, S., Klemenz, C., and Scheel, H. (1996). Electrochemical and photoelectrochemical investigation of single-crystal anatase. *Journal of the American Chemical Society*, 118(28):6716–6723.

Kerker, G. (1980). Non-singular atomic pseudopotentials for solid state applications. *Journal of Physics C: Solid State Physics*, 13(9):L189.

Kim, W., Tachikawa, T., Moon, G.-h., Majima, T., and Choi, W. (2014). Molecular-level understanding of the photocatalytic activity difference between anatase and rutile nanoparticles. *Angewandte Chemie International Edition*, 53(51):14036–14041.

Koffyberg, F. and Benko, F. (1982). A photoelectrochemical determination of the position of the conduction and valence band edges of p-type CuO. *Journal of Applied Physics*, 53(2):1173–1177.

Kohn, W., Becke, A. D., and Parr, R. G. (1996). Density functional theory of electronic structure. *The Journal of Physical Chemistry*, 100(31):12974–12980.

Kohn, W. and Sham, L. J. (1965). Self-consistent equations including exchange and correlation effects. *Physical Review*, 140(4A):A1133.

Korir, K., Amolo, G., Makau, N., and Joubert, D. (2011). First-principle calculations of the bulk properties of 4d transition metal carbides and nitrides in the rocksalt, zincblende and wurtzite structures. *Diamond and Related Materials*, 20(2):157–164.

Kralj, M., Pertram, T., Seriani, N., Mittendorfer, F., Krupski, A., Becker, C., and Wandelt, K. (2008). Pd (110) surface oxide structures investigated by STM and DFT. *Surface Science*, 602(24):3706–3713.

Kresse, G. and Joubert, D. (1999). From ultrasoft pseudopotentials to the projector augmented-wave method. *Physical Review B*, 59(3):1758.

Kum, J. M., Park, Y. J., Kim, H. J., and Cho, S. O. (2015). Plasmon-enhanced photocatalytic hydrogen production over visible-light responsive Cu/TiO_2. *Nanotechnology*, 26(12):125402.

Kumar, D. P., Reddy, N. L., Srinivas, B., Durgakumari, V., Roddatis, V., Bondarchuk, O., Karthik, M., Ikuma, Y., and Shankar, M. (2016). Stable and active Cu_xO/TiO_2 nanostructured catalyst for proficient hydrogen production under solar light irradiation. *Solar Energy Materials and Solar Cells*, 146:63–71.

Lalitha, K., Sadanandam, G., Kumari, V. D., Subrahmanyam, M., Sreedhar, B., and Hebalkar, N. Y. (2010). Highly stabilized and finely dispersed Cu_2O/TiO_2: a promising visible sensitive photocatalyst for continuous production of hydrogen from glycerol: water mixtures. *The Journal of Physical Chemistry C*, 114(50):22181–22189.

Leung, T., Chan, C. T., and Harmon, B. (1991). Ground-state properties of Fe, Co, Ni, and their monoxides: Results of the generalized gradient approximation. *Physical Review B*, 44(7):2923.

Leytner, S. and Hupp, J. T. (2000). Evaluation of the energetics of electron trap states at the nanocrystalline titanium dioxide/aqueous solution interface via time-resolved photoacoustic spectroscopy. *Chemical Physics Letters*, 330(3-4):231–236.

Li, G., Dimitrijevic, N. M., Chen, L., Rajh, T., and Gray, K. A. (2008). Role of surface/interfacial Cu^{2+} sites in the photocatalytic activity of coupled CuO-TiO_2 nanocomposites. *The Journal of Physical Chemistry C*, 112(48):19040–19044.

Li, R., Weng, Y., Zhou, X., Wang, X., Mi, Y., Chong, R., Han, H., and Li, C. (2015a). Achieving overall water splitting using titanium dioxide-based photocatalysts of different phases. *Energy & Environmental Science*, 8(8):2377–2382.

Li, X. and Li, F. (2001). Study of Au/Au^{3+}-TiO_2 photocatalysts toward visible photooxidation for water and wastewater treatment. *Environmental Science & Technology*, 35(11):2381–2387.

Li, Y., Wang, B., Liu, S., Duan, X., and Hu, Z. (2015b). Synthesis and characterization of Cu_2O/TiO_2 photocatalysts for H_2 evolution from aqueous solution with different scavengers. *Applied Surface Science*, 324:736–744.

Li, Y.-F., Liu, Z.-P., Liu, L., and Gao, W. (2010). Mechanism and activity of photocatalytic oxygen evolution on titania anatase in aqueous surroundings. *Journal of the American Chemical Society*, 132(37):13008–13015.

Li, Y.-F. and Selloni, A. (2016). Pathway of photocatalytic oxygen evolution on aqueous TiO_2 anatase and insights into the different activities of anatase and rutile. *ACS Catalysis*, 6(7):4769–4774.

Li, Z., Liu, J., Wang, D., Gao, Y., and Shen, J. (2012). $Cu_2O/Cu/TiO_2$ nanotube ohmic heterojunction arrays with enhanced photocatalytic hydrogen production activity. *International Journal of Hydrogen Energy*, 37(8):6431–6437.

Liao, P., Keith, J. A., and Carter, E. A. (2012). Water oxidation on pure and doped hematite (0001) surfaces: prediction of Co and Ni as effective dopants for electrocatalysis. *Journal of the American Chemical Society*, 134(32):13296–13309.

Linic, S., Christopher, P., and Ingram, D. B. (2011). Plasmonic-metal nanostructures for efficient conversion of solar to chemical energy. *Nature Materials*, 10(12):911.

Linsebigler, A. L., Lu, G., and Yates Jr, J. T. (1995). Photocatalysis on TiO_2 surfaces: principles, mechanisms, and selected results. *Chemical Reviews*, 95(3):735–758.

Lipiński, W., Davidson, J., Haussener, S., Klausner, J., Mehdizadeh, A., Petrasch, J., Steinfeld, A., and Venstrom, L. (2013). Review of heat transfer research for solar thermochemical applications. *Journal of Thermal Science and Engineering Applications*, 5(2):021005.

Liu, B., Chen, H. M., Liu, C., Andrews, S. C., Hahn, C., and Yang, P. (2013a). Large-scale synthesis of transition-metal-doped TiO_2 nanowires with controllable overpotential. *Journal of the American Chemical Society*, 135(27):9995–9998.

Liu, C., Yang, B., Tyo, E., Seifert, S., DeBartolo, J., von Issendorff, B., Zapol, P., Vajda, S., and Curtiss, L. A. (2015a). Carbon dioxide conversion to methanol over size-selected Cu_4 clusters at low pressures. *Journal of the American Chemical Society*, 137(27):8676–8679.

Liu, D., Fernández, Y., Ola, O., Mackintosh, S., Maroto-Valer, M., Parlett, C. M., Lee, A. F., and Wu, J. C. (2012). On the impact of Cu dispersion on CO_2 photoreduction over Cu/TiO_2. *Catalysis Communications*, 25:78–82.

Liu, L., Gao, F., Zhao, H., and Li, Y. (2013b). Tailoring Cu valence and oxygen vacancy in Cu/TiO_2 catalysts for enhanced CO_2 photoreduction efficiency. *Applied Catalysis B: Environmental*, 134:349–358.

Liu, L. and Li, Y. (2014). Understanding the reaction mechanism of photocatalytic reduction of CO_2 with H_2O on TiO_2-based photocatalysts: a review. *Aerosol Air Qual Res*, 14(2):453–469.

Liu, L., Yang, W., Li, Q., Gao, S., and Shang, J. K. (2014). Synthesis of Cu_2O nanospheres decorated with TiO_2 nanoislands, their enhanced photoactivity and stability under visible light illumination, and their post-illumination catalytic memory. *ACS Applied Materials & Interfaces*, 6(8):5629–5639.

Liu, X., Cui, S., Sun, Z., and Du, P. (2015b). Copper oxide nanomaterials synthesized from simple copper salts as active catalysts for electrocatalytic water oxidation. *Electrochimica Acta*, 160:202–208.

Liu, X., Cui, S., Sun, Z., Ren, Y., Zhang, X., and Du, P. (2016). Self-supported copper oxide electrocatalyst for water oxidation at low overpotential and confirmation of its robustness by Cu K-edge X-ray absorption spectroscopy. *The Journal of Physical Chemistry C*, 120(2):831–840.

Liu, Y., Li, Z., Green, M., Just, M., Li, Y. Y., and Chen, X. (2017). Titanium dioxide nanomaterials for photocatalysis. *Journal of Physics D: Applied Physics*, 50(19):193003.

Löwdin, P.-O. (1955). Quantum theory of many-particle systems .I. physical interpretations by means of density matrices, natural spin-orbitals, and convergence problems in the method of configurational interaction. *Physical Review*, 97(6):1474.

Ma, J.-G., Zhang, C.-R., Gong, J.-J., Yang, B., Zhang, H.-M., Wang, W., Wu, Y.-Z., Chen, Y.-H., and Chen, H.-S. (2014). The adsorption of α-cyanoacrylic acid on anatase TiO_2 (101) and (001) surfaces: a density functional theory study. *The Journal of Chemical Physics*, 141(23):234705.

Ma, L.-L., Li, J.-L., Sun, H.-Z., Qiu, M.-Q., Wang, J.-B., Chen, J.-Y., and Yu, Y. (2010a). Self-assembled Cu_2O flowerlike architecture: polyol synthesis, photocatalytic activity and stability under simulated solar light. *Materials Research Bulletin*, 45(8):961–968.

Ma, Q., Liu, S., Weng, L., Liu, Y., and Liu, B. (2010b). Growth, structure and photocatalytic properties of hierarchical Cu–Ti–O nanotube arrays by anodization. *Journal of Alloys and Compounds*, 501(2):333–338.

Macounova, K. M., Klusackova, M., Nebel, R., Zukalova, M., Klementova, M., Castelli, I. E., Spo, M. D., Rossmeisl, J., Kavan, L., and Krtil, P. (2017). Synergetic surface sensitivity

of photoelectrochemical water oxidation on TiO_2 (anatase) electrodes. *The Journal of Physical Chemistry C*, 121(11):6024–6032.

Maeda, K. (2011). Photocatalytic water splitting using semiconductor particles: history and recent developments. *Journal of Photochemistry and Photobiology C: Photochemistry Reviews*, 12(4):237–268.

Man, I. C., Su, H.-Y., Calle-Vallejo, F., Hansen, H. A., Martínez, J. I., Inoglu, N. G., Kitchin, J., Jaramillo, T. F., Nørskov, J. K., and Rossmeisl, J. (2011). Universality in oxygen evolution electrocatalysis on oxide surfaces. *ChemCatChem*, 3(7):1159–1165.

Marcus, R. A. (1964). Chemical and electrochemical electron-transfer theory. *Annual Review of Physical Chemistry*, 15(1):155–196.

McQuarrie, D. and Simon, J. (1999a). Nonequilibrium thermodynamics. *Molecular Thermodynamics. University Science Books, Sausalito, CA*, pages 581–627.

McQuarrie, D. A. and Simon, J. D. (1999b). *Molecular thermodynamics*. University Science Books Sausalito, CA.

Mellan, T. A., Maenetja, K. P., Ngoepe, P. E., Woodley, S. M., Catlow, C. R. A., and Grau-Crespo, R. (2013). Lithium and oxygen adsorption at the β-MnO_2 (110) surface. *Journal of Materials Chemistry A*, 1(47):14879–14887.

Mendive, C. B., Hansmann, D., Bredow, T., and Bahnemann, D. (2011). New insights into the mechanism of TiO_2 photocatalysis: thermal processes beyond the electron–hole creation. *The Journal of Physical Chemistry C*, 115(40):19676–19685.

Meng'wa, V., Makau, N., Amolo, G., Scandolo, S., and Seriani, N. (2017). Ab-Initio simulations of copper oxide nanowires and clusters on TiO_2 (101) anatase surface. *The Journal of Physical Chemistry C*, 121(37):20359–20365.

Meng'wa, V., Amolo, G., Makau, N., Lutta, S., Okoth, M., Mwabora, J., Musembi, R., Maghanga, C., and Gateru, R. (2016). Electronic properties of catechol adsorbed on rutile TiO_2 and SnO_2 (110) surfaces: A density functional theory study. *The African Review of Physics*, 11(21):157–165.

Meng'wa, V., Makau, N., Amolo, G., Scandolo, S., and Seriani, N. (2018). Density functional theory study of water photo-oxidation at copper oxide nanostructures on the anatase (101) surface. *The Journal of Physical Chemistry C*, 122(29):16765–16771.

Meyer, B., Polity, A., Reppin, D., Becker, M., Hering, P., Klar, P., Sander, T., Reindl, C., Benz, J., Eickhoff, M., Heiliger, C., Heinemann, M., Blasing, J., Krost, A., Shokovets, S., Muller, C., and Ronning, C. (2012). Binary copper oxide semiconductors: From materials towards devices. *Physica Status Solidi (b)*, 249(8):1487–1509.

Meyer, B. K., Merita, S., and Polity, A. (2013). On the synthesis and properties of ternary copper oxide sulfides ($Cu_2O_{1-x}S_x$). *Physica Status Solidi (RRL)-Rapid Research Letters*, 7(5):360–363.

Michikazu, H., Takeshi, K., Mutsuko, K., Sigeru, I., Kiyoaki, S., Akira, T., Kondo, J., and Kazunari, D. (1998). Cu_2O as a photocatalyst for overall water splitting under visible light irradiation. *Chemical Communications*, (3):357–358.

Minami, T., Miyata, T., and Nishi, Y. (2014). Cu_2O-based heterojunction solar cells with an Al-doped ZnO/oxide semiconductor/thermally oxidized Cu_2O sheet structure. *Solar Energy*, 105:206–217.

Mishra, A. K., Roldan, A., and de Leeuw, N. H. (2016). CuO surfaces and CO_2 activation: a dispersion-corrected DFT+U study. *The Journal of Physical Chemistry C*, 120(4):2198–2214.

Mittendorfer, F., Seriani, N., Dubay, O., and Kresse, G. (2007). Morphology of mesoscopic Rh and Pd nanoparticles under oxidizing conditions. *Physical Review B*, 76(23):233413.

Mohamed, H. H., Dillert, R., and Bahnemann, D. W. (2012). Kinetic and mechanistic investigations of the light induced formation of gold nanoparticles on the surface of TiO_2. *Chemistry-A European Journal*, 18(14):4314–4321.

Mohamed, H. H., Mendive, C. B., Dillert, R., and Bahnemann, D. W. (2011). Kinetic and mechanistic investigations of multielectron transfer reactions induced by stored electrons in TiO_2 nanoparticles: a stopped flow study. *The Journal of Physical Chemistry A*, 115(11):2139–2147.

Moniz, S. J., Shevlin, S. A., Martin, D. J., Guo, Z.-X., and Tang, J. (2015). Visible-light driven heterojunction photocatalysts for water splitting-a critical review. *Energy and Environmental Science*, 8(3):731–759.

Monkhorst, H. J. and Pack, J. D. (1976). Special points for Brillouin-zone integrations. *Physical Review B*, 13(12):5188.

Montini, T., Gombac, V., Sordelli, L., Delgado, J. J., Chen, X., Adami, G., and Fornasiero, P. (2011). Nanostructured Cu/TiO_2 photocatalysts for H_2 production from ethanol and glycerol aqueous solutions. *ChemCatChem*, 3(3):574–577.

Montoya, J. F., Bahnemann, D. W., Peral, J., and Salvador, P. (2014). Catalytic role of TiO_2 terminal oxygen atoms in liquid-phase photocatalytic reactions: Oxidation of aromatic compounds in anhydrous acetonitrile. *ChemPhysChem*, 15(11):2311–2320.

Mori, K., Yamashita, H., and Anpo, M. (2012). Photocatalytic reduction of CO_2 with H_2O on various titanium oxide photocatalysts. *Rsc Advances*, 2(8):3165–3172.

Moser, J., Punchihewa, S., Infelta, P. P., and Graetzel, M. (1991). Surface complexation of colloidal semiconductors strongly enhances interfacial electron-transfer rates. *Langmuir*, 7(12):3012–3018.

Muniz-Miranda, M., Gellini, C., Simonelli, A., Tiberi, M., Giammanco, F., and Giorgetti, E. (2013). Characterization of copper nanoparticles obtained by laser ablation in liquids. *Applied Physics A*, 110(4):829–833.

Murakami, Y., Nishino, J., Mesaki, T., and Nosaka, Y. (2011). Femtosecond diffuse-reflectance spectroscopy of various commercially available TiO_2 powders. *Spectroscopy Letters*, 44(2):88–94.

Nakamura, R. and Nakato, Y. (2004). Primary intermediates of oxygen photoevolution reaction on TiO_2 (rutile) particles, revealed by in situ FTIR absorption and photoluminescence measurements. *Journal of the American Chemical Society*, 126(4):1290–1298.

Nakamura, R., Tanaka, T., and Nakato, Y. (2004). Mechanism for visible light responses in anodic photocurrents at N-doped TiO_2 film electrodes. *The Journal of Physical Chemistry B*, 108(30):10617–10620.

Nguyen, M.-T., Seriani, N., Piccinin, S., and Gebauer, R. (2014). Photo-driven oxidation of water on α-Fe_2O_3 surfaces: An ab initio study. *The Journal of Chemical Physics*, 140(6):064703.

Nolan, M. and Elliott, S. D. (2008). Tuning the electronic structure of the transparent conducting oxide Cu_2O. *Thin Solid Films*, 516(7):1468–1472.

Nolan, M., Iwaszuk, A., and Gray, K. A. (2014). Localization of photoexcited electrons and holes on low coordinated Ti and O sites in free and supported TiO_2 nanoclusters. *The Journal of Physical Chemistry C*, 118(48):27890–27900.

Nolan, M., Iwaszuk, A., Lucid, A. K., Carey, J. J., and Fronzi, M. (2016). Design of novel visible light active photocatalyst materials: surface modified TiO_2. *Advanced Materials*, 28(27):5425–5446.

Nørskov, J. K., Rossmeisl, J., Logadottir, A., Lindqvist, L., Kitchin, J. R., Bligaard, T., and Jonsson, H. (2004). Origin of the overpotential for oxygen reduction at a fuel-cell cathode. *The Journal of Physical Chemistry B*, 108(46):17886–17892.

Nozik, A. (1975). Photoelectrolysis of water using semiconducting TiO_2 crystals. *Nature*, 257(5525):383–386.

Nozik, A. J. and Memming, R. (1996). Physical chemistry of semiconductor- liquid interfaces. *The Journal of Physical Chemistry*, 100(31):13061–13078.

Ong, W.-J., Tan, L.-L., Ng, Y. H., Yong, S.-T., and Chai, S.-P. (2016). Graphitic carbon nitride (gC_3N_4)-based photocatalysts for artificial photosynthesis and environmental remediation: are we a step closer to achieving sustainability? *Chemical Reviews*, 116(12):7159–7329.

O'regan, B. and Grätzel, M. (1991). A low-cost, high-efficiency solar cell based on dye-sensitized colloidal TiO_2 films. *Nature*, 353(6346):737.

Ostlund, N. S. and Szabo, A. (1996). *Modern Quantum Chemistry: Introduction to Advanced Electronic Structure Theory*. Dover Publications Inc New edition edn.

Pagel, R. and Dohrmann, J. K. (2007). Thermochemical study of photoinduced processes at TiO_2 nanoparticles in aqueous suspension containing Br^- or Cl^-. Photodeaggregation and subsequent processes. *The Journal of Physical Chemistry C*, 111(11):4458–4464.

Pan, X., Yang, M.-Q., Fu, X., Zhang, N., and Xu, Y.-J. (2013). Defective TiO_2 with oxygen vacancies: synthesis, properties and photocatalytic applications. *Nanoscale*, 5(9):3601–3614.

Pang, C. L., Lindsay, R., and Thornton, G. (2008). Chemical reactions on rutile TiO_2 (110). *Chemical Society Reviews*, 37(10):2328–2353.

Pastoriza-Santos, I., Sánchez-Iglesias, A., Rodríguez-González, B., and Liz-Marzán, L. M. (2009). Aerobic synthesis of Cu nanoplates with intense plasmon resonances. *Small*, 5(4):440–443.

Patrick, C. E. and Giustino, F. (2014). Structure of a water monolayer on the anatase TiO_2 (101) surface. *Physical Review Applied*, 2(1):014001.

Peiró, A. M., Colombo, C., Doyle, G., Nelson, J., Mills, A., and Durrant, J. R. (2006). Photochemical reduction of oxygen adsorbed to nanocrystalline TiO_2 films: A transient absorption and oxygen scavenging study of different TiO_2 preparations. *The Journal of Physical Chemistry B*, 110(46):23255–23263.

Perdew, J., Burke, K., and Ernzerhof, M. (1998). Perdew, Burke, and Ernzerhof reply. *Physical Review Letters*, 80(4):891.

Perdew, J. P., Burke, K., and Ernzerhof, M. (1996). Generalized gradient approximation made simple. *Physical Review Letters*, 77(18):3865.

Perdew, J. P., Parr, R. G., Levy, M., and Balduz Jr, J. L. (1982). Density-functional theory for fractional particle number: derivative discontinuities of the energy. *Physical Review Letters*, 49(23):1691.

Perdew, J. P. and Zunger, A. (1981). Self-interaction correction to density-functional approximations for many-electron systems. *Physical Review B*, 23(10):5048.

Peter, M., Graeme, W., Toby, K., and Stephen, C. (1997). Atomistic simulation of the surface structure of the TiO_2 polymorphs rutile and anatase. *Journal of Materials Chemistry*, 7(3):563–568.

Poizot, P., Laruelle, S., Grugeon, S., Dupont, L., and Tarascon, J. (2000). Nano-sized transition-metal oxides as negative-electrode materials for lithium-ion batteries. *Nature*, 407(6803):496.

Prévot, M. S. and Sivula, K. (2013). Photoelectrochemical tandem cells for solar water splitting. *The Journal of Physical Chemistry C*, 117(35):17879–17893.

Proynov, E., Ruiz, E., Vela, A., and Salahub, D. (1995). Determining and extending the domain of exchange and correlation functionals. *International Journal of Quantum Chemistry*, 56(S29):61–78.

Rappe, A. M., Rabe, K. M., Kaxiras, E., and Joannopoulos, J. (1990). Optimized pseudopotentials. *Physical Review B*, 41(2):1227.

Rayner, D. M., Lian, L., Fournier, R., Mitchell, S. A., and Hackett, P. A. (1995). Thermal and photodesorption from a molecular surface: Ammonia on Ag_2. *Physical Review Letters*, 74(11):2070.

Resta, R. (2008). Physical chemistry: Charge states in transition. *Nature*, 453(7196):735.

Reuter, K. and Scheffler, M. (2001). Composition, structure, and stability of RuO_2 (110) as a function of oxygen pressure. *Physical Review B*, 65(3):035406.

Reynal, A., Lakadamyali, F., Gross, M. A., Reisner, E., and Durrant, J. R. (2013). Parameters affecting electron transfer dynamics from semiconductors to molecular catalysts for the photochemical reduction of protons. *Energy & Environmental Science*, 6(11):3291–3300.

Rossmeisl, J., Qu, Z.-W., Zhu, H., Kroes, G.-J., and Nørskov, J. K. (2007). Electrolysis of water on oxide surfaces. *Journal of Electroanalytical Chemistry*, 607(1):83–89.

Roy, S. C., Varghese, O. K., Paulose, M., and Grimes, C. A. (2010). Toward solar fuels:

photocatalytic conversion of carbon dioxide to hydrocarbons. *Acs Nano*, 4(3):1259–1278.

Salvador, P. and Gutierrez, C. (1984). The nature of surface states involved in the photo-and electroluminescence spectra of n-titanium dioxide electrodes. *The Journal of Physical Chemistry*, 88(16):3696–3698.

Saraireh, S. A. and Altarawneh, M. (2013). Density functional theory periodic slab calculations of adsorption and dissociation of H_2O on the Cu_2O (110): CuO surface. *Canadian Journal of Physics*, 91(12):1101–1106.

Scanlon, D. O., Walsh, A., Morgan, B. J., Watson, G. W., Payne, D. J., and Egdell, R. G. (2009). Effect of Cr substitution on the electronic structure of $CuAl_{1-x}Cr_x$ O_2. *Physical Review B*, 79(3):035101.

Schmidt-Whitley, R., Martinez-Clemente, M., and Revcolevschi, A. (1974). Growth and microstructural control of single crystal cuprous oxide Cu_2O. *Journal of Crystal Growth*, 23(2):113–120.

Schneider, J., Matsuoka, M., Takeuchi, M., Zhang, J., Horiuchi, Y., Anpo, M., and Bahnemann, D. W. (2014). Understanding TiO_2 photocatalysis: mechanisms and materials. *Chemical Reviews*, 114(19):9919–9986.

Schrauzer, G. and Guth, T. (1977). Photocatalytic reactions. 1. photolysis of water and photoreduction of nitrogen on titanium dioxide. *Journal of the American Chemical Society*, 99(22):7189–7193.

Senevirathna, M., Pitigala, P., and Tennakone, K. (2005). Water photoreduction with Cu_2O quantum dots on TiO_2 nano-particles. *Journal of Photochemistry and Photobiology A: Chemistry*, 171(3):257–259.

Seriani, N. (2009). Ab initio thermodynamics of lithium oxides: from bulk phases to nanoparticles. *Nanotechnology*, 20(44):445703.

Seriani, N. (2012). Sodium promoter inducing a phase change in a palladium catalyst. *The Journal of Physical Chemistry C*, 116(43):22974–22979.

Seriani, N., Jin, Z., Pompe, W., and Ciacchi, L. C. (2007). A DFT study of platinum oxides: from infinite crystals to nanoscopic particles. *Physical Review B*, 76:155421.

Seriani, N. and Mittendorfer, F. (2008). Platinum-group and noble metals under oxidizing conditions. *Journal of Physics: Condensed Matter*, 20(18):184023.

Seriani, N., Pinilla, C., and Crespo, Y. (2015). Presence of gap states at Cu/TiO_2 anatase surfaces: consequences for the photocatalytic activity. *The Journal of Physical Chemistry C*, 119(12):6696–6702.

Seriani, N., Pompe, W., and Ciacchi, L. C. (2006). Catalytic oxidation activity of Pt_3O_4 surfaces and thin films. *The Journal of Physical Chemistry B*, 110(30):14860–14869.

Serpone, N. (2006). Is the band gap of pristine TiO_2 narrowed by anion- and cation-doping of titanium dioxide in second-generation photocatalysts? *The Journal of Physical Chemistry B*, 110(48):24287–24293.

Serpone, N. and Emeline, A. (2002). Suggested terms and definitions in photocatalysis and radiocatalysis. *International Journal of Photoenergy*, 4(3):91–131.

Serpone, N., Lawless, D., and Khairutdinov, R. (1995). Size effects on the photophysical properties of colloidal anatase TiO_2 particles: size quantization versus direct transitions in this indirect semiconductor? *The Journal of Physical Chemistry*, 99(45):16646–16654.

Shankar, K., Basham, J. I., Allam, N. K., Varghese, O. K., Mor, G. K., Feng, X., Paulose, M., Seabold, J. A., Choi, K.-S., and Grimes, C. A. (2009). Recent advances in the use of TiO_2 nanotube and nanowire arrays for oxidative photoelectrochemistry. *The Journal of Physical Chemistry C*, 113(16):6327–6359.

Sharma, P. K., Cortes, M. A. L., Hamilton, J. W., Han, Y., Byrne, J. A., and Nolan, M. (2017). Surface modification of TiO_2 with copper clusters for band gap narrowing. *Catalysis Today*.

Sinatra, L., LaGrow, A. P., Peng, W., Kirmani, A. R., Amassian, A., Idriss, H., and Bakr, O. M. (2015). A $Au/Cu_2O–TiO_2$ system for photo-catalytic hydrogen production. A

pn-junction effect or a simple case of in situ reduction? *Journal of Catalysis*, 322:109–117.

Singh, D. and Nordström, L. (2006). Planewaves pseudopotentials and the LAPW method, pringer. *New York*.

Singh, M., Sinha, I., Premkumar, M., Singh, A., and Mandal, R. (2010). Structural and surface plasmon behavior of Cu nanoparticles using different stabilizers. *Colloids and Surfaces A: Physicochemical and Engineering Aspects*, 359(1-3):88–94.

Sivula, K., Le Formal, F., and Grätzel, M. (2011). Solar water splitting: progress using hematite (α-Fe_2O_3) photoelectrodes. *ChemSusChem*, 4(4):432–449.

Slamet, S., Nasution, H. W., Purnama, E., Kosela, S., Gunlazuardi, J., et al. (2005). Photocatalytic reduction of CO_2 on copper-doped titania catalysts prepared by improved-impregnation method. *Catalysis Communications*, 6(5):313–319.

Slater, J. C. (1951). A simplification of the Hartree-Fock method. *Physical Review*, 81(3):385.

Solovyev, I., Dederichs, P., and Anisimov, V. (1994). Corrected atomic limit in the local-density approximation and the electronic structure of d impurities in Rb. *Physical Review B*, 50(23):16861.

Soon, A., Söhnel, T., and Idriss, H. (2005). Plane-wave pseudopotential density functional theory periodic slab calculations of CO adsorption on Cu_2O (1 1 1) surface. *Surface Science*, 579(2-3):131–140.

Soon, A., Todorova, M., Delley, B., and Stampfl, C. (2007a). Erratum: Thermodynamic stability and structure of copper oxide surfaces: A first-principles investigation [Phys. Rev. B 75, 125420 (2007)]. *Physical Review B*, 76(12):129902.

Soon, A., Todorova, M., Delley, B., and Stampfl, C. (2007b). Thermodynamic stability and structure of copper oxide surfaces: A first-principles investigation. *Physical Review B*, 75(12):125420.

Stopper, K. and Dohrmann, J. K. (2000). Laser-induced reactions on 2.4-nm colloidal

TiO_2 particles in aqueous solution: A study by time-resolved optoacoustic calorimetry. *Zeitschrift für Physikalische Chemie*, 214(5):555.

Stull, D. R. and Prophet, H. (1971). JANAF thermochemical tables. Technical report, National Standard Reference Data System.

Sun, C., Liu, L.-M., Selloni, A., Lu, G. Q. M., and Smith, S. C. (2010). Titania-water interactions: a review of theoretical studies. *Journal of Materials Chemistry*, 20(46):10319–10334.

Szczepankiewicz, S. H., Colussi, A., and Hoffmann, M. R. (2000). Infrared spectra of photoinduced species on hydroxylated titania surfaces. *The Journal of Physical Chemistry B*, 104(42):9842–9850.

Tachikawa, T., Fujitsuka, M., and Majima, T. (2007). Mechanistic insight into the TiO_2 photocatalytic reactions: design of new photocatalysts. *The Journal of Physical Chemistry C*, 111(14):5259–5275.

Tada, H., Jin, Q., Iwaszuk, A., and Nolan, M. (2014). Molecular-scale transition metal oxide nanocluster surface-modified titanium dioxide as solar-activated environmental catalysts. *The Journal of Physical Chemistry C*, 118(23):12077–12086.

Takeuchi, K., Nakamura, I., Matsumoto, O., Sugihara, S., Ando, M., and Ihara, T. (2000). Preparation of visible-light-responsive titanium oxide photocatalysts by plasma treatment. *Chemistry Letters*, 29(12):1354–1355.

Tamaki, Y., Furube, A., Murai, M., Hara, K., Katoh, R., and Tachiya, M. (2006). Direct observation of reactive trapped holes in TiO_2 undergoing photocatalytic oxidation of adsorbed alcohols: evaluation of the reaction rates and yields. *Journal of the American Chemical Society*, 128(2):416–417.

Tamaki, Y., Furube, A., Murai, M., Hara, K., Katoh, R., and Tachiya, M. (2007). Dynamics of efficient electron–hole separation in TiO_2 nanoparticles revealed by femtosecond transient absorption spectroscopy under the weak-excitation condition. *Physical Chemistry Chemical Physics*, 9(12):1453–1460.

Tang, J., Durrant, J. R., and Klug, D. R. (2008). Mechanism of photocatalytic water splitting in TiO_2. Reaction of water with photoholes, importance of charge carrier dynamics, and evidence for four-hole chemistry. *Journal of the American Chemical Society*, 130(42):13885–13891.

Tang, W., Peterson, A. A., Varela, A. S., Jovanov, Z. P., Bech, L., Durand, W. J., Dahl, S., Nørskov, J. K., and Chorkendorff, I. (2012). The importance of surface morphology in controlling the selectivity of polycrystalline copper for CO_2 electroreduction. *Physical Chemistry Chemical Physics*, 14(1):76–81.

Teng, F., Chen, M., Li, N., Hua, X., Wang, K., and Xu, T. (2014). Effect of TiO_2 surface structure on the hydrogen production activity of the Pt@CuO/TiO_2 photocatalysts for water splitting. *ChemCatChem*, 6(3):842–847.

Thompson, T. L. and Yates, J. T. (2006). Surface science studies of the photoactivation of TiO_2 new photochemical processes. *Chemical Reviews*, 106(10):4428–4453.

Tian, H., Zhang, X. L., Scott, J., Ng, C., and Amal, R. (2014). TiO_2-supported copper nanoparticles prepared via ion exchange for photocatalytic hydrogen production. *Journal of Materials Chemistry A*, 2(18):6432–6438.

Tian, Y. and Tatsuma, T. (2005). Mechanisms and applications of plasmon-induced charge separation at TiO_2 films loaded with gold nanoparticles. *Journal of the American Chemical Society*, 127(20):7632–7637.

Tran, F. and Blaha, P. (2011). Implementation of screened hybrid functionals based on the Yukawa potential within the LAPW basis set. *Physical Review B*, 83(23):235118.

Treacy, J. P., Hussain, H., Torrelles, X., Grinter, D. C., Cabailh, G., Bikondoa, O., Nicklin, C., Selcuk, S., Selloni, A., Lindsay, R., et al. (2017). Geometric structure of anatase TiO_2 (101). *Physical Review B*, 95(7):075416.

Tseng, I.-H., Wu, J. C., and Chou, H.-Y. (2004). Effects of sol–gel procedures on the photocatalysis of Cu/TiO_2 in CO_2 photoreduction. *Journal of Catalysis*, 221(2):432–440.

Ueno, K. and Misawa, H. (2013). Surface plasmon-enhanced photochemical reactions. *Journal of Photochemistry and Photobiology C: Photochemistry Reviews*, 15:31–52.

Ulman, K., Nguyen, M.-T., Seriani, N., Piccinin, S., and Gebauer, R. (2017). A unified picture of water oxidation on bare and gallium oxide-covered hematite from density functional theory. *ACS Catalysis*, 7(3):1793–1804.

Valdes, A. and Kroes, G.-J. (2010). Cluster study of the photo-oxidation of water on rutile titanium dioxide (TiO_2). *The Journal of Physical Chemistry C*, 114(3):1701–1708.

Valdes, A., Qu, Z.-W., Kroes, G.-J., Rossmeisl, J., and Nørskov, J. K. (2008). Oxidation and photo-oxidation of water on TiO_2 surface. *The Journal of Physical Chemistry C*, 112(26):9872–9879.

Vanderbilt, D. (1990). Soft self-consistent pseudopotentials in a generalized eigenvalue formalism. *Physical Review B*, 41(11):7892.

Varghese, O. K., Paulose, M., LaTempa, T. J., and Grimes, C. A. (2009). High-rate solar photocatalytic conversion of CO_2 and water vapor to hydrocarbon fuels. *Nano letters*, 9(2):731–737.

Vittadini, A., Selloni, A., Rotzinger, F., and Grätzel, M. (1998). Structure and energetics of water adsorbed at TiO_2 anatase (101) and (001) surfaces. *Physical Review Letters*, 81(14):2954.

Vukojević, S., Trapp, O., Grunwaldt, J.-D., Kiener, C., and Schüth, F. (2005). Quasi-homogeneous methanol synthesis over highly active copper nanoparticles. *Angewandte Chemie*, 117(48):8192–8195.

Walle, L., Borg, A., Johansson, E., Plogmaker, S., Rensmo, H., Uvdal, P., and Sandell, A. (2011). Mixed dissociative and molecular water adsorption on anatase TiO_2 (101). *The Journal of Physical Chemistry C*, 115(19):9545–9550.

Wang, J., Wen, F., Zhang, Z., Zhang, X., Pan, Z., Zhang, G., Zhao, G., Kang, P., and Zhang, P. (2006). Preparation of nanometer TiO_2 doped with upconversion luminescence agent and investigation on degradation of ethyl violet using visible light. *Huan Jing ke Xue= Huanjing Kexue*, 27(6):1133–1139.

Wang, L., Ge, J., Wang, A., Deng, M., Wang, X., Bai, S., Li, R., Jiang, J., Zhang, Q., Luo, Y., et al. (2014a). Designing p-type semiconductor–metal hybrid structures for improved photocatalysis. *Angewandte Chemie*, 126(20):5207–5211.

Wang, Z., Brouri, D., Casale, S., Delannoy, L., and Louis, C. (2016). Exploration of the preparation of Cu/TiO_2 catalysts by deposition–precipitation with urea for selective hydrogenation of unsaturated hydrocarbons. *Journal of Catalysis*, 340:95–106.

Wang, Z., Liu, Y., Martin, D. J., Wang, W., Tang, J., and Huang, W. (2013). CuO_x–TiO_2 junction: what is the active component for photocatalytic H_2 production? *Physical Chemistry Chemical Physics*, 15(36):14956–14960.

Wang, Z., Teramura, K., Shishido, T., and Tanaka, T. (2014b). Characterization of Cu nanoparticles on TiO_2 photocatalysts fabricated by electroless plating method. *Topics in Catalysis*, 57(10-13):975–983.

Warman, J. M., de Haas Matthijs, P., Pierre, P., PM, K. T., van der Zouwen-Assink Etty, A., Adri, M., and Ronald, C. (1991). Electronic processes in semiconductor materials studied by nanosecond time-resolved microwave conductivity-III. Al_2O_3, MgO and TiO_2 powders. *International Journal of Radiation Applications and Instrumentation. Part C. Radiation Physics and Chemistry*, 37(3):433–442.

Wilson, R. (1980). Observation and analysis of surface states on TiO_2 electrodes in aqueous electrolytes. *Journal of The Electrochemical Society*, 127(1):228–234.

Wimmer, E., Krakauer, H., Weinert, M., and Freeman, A. (1981). Full-potential self-consistent linearized-augmented-plane-wave method for calculating the electronic structure of molecules and surfaces: O_2 molecule. *Physical Review B*, 24(2):864.

Wu, D., Zhang, Q., and Tao, M. (2006). LSDA + U study of cupric oxide: Electronic structure and native point defects. *Physical Review B*, 73(23):235206.

Wu, N.-L. and Lee, M.-S. (2004). Enhanced TiO_2 photocatalysis by Cu in hydrogen production from aqueous methanol solution. *International Journal of Hydrogen Energy*, 29(15):1601–1605.

Xin, B., Wang, P., Ding, D., Liu, J., Ren, Z., and Fu, H. (2008). Effect of surface species on Cu-TiO_2 photocatalytic activity. *Applied Surface Science*, 254(9):2569–2574.

Xiong, L., Yang, F., Yan, L., Yan, N., Yang, X., Qiu, M., and Yu, Y. (2011). Bifunctional photocatalysis of TiO_2/Cu_2O composite under visible light: Ti^{3+} in organic pollutant degradation and water splitting. *Journal of Physics and Chemistry of Solids*, 72(9):1104–1109.

Xu, S., Du, A. J., Liu, J., Ng, J., and Sun, D. D. (2011). Highly efficient CuO incorporated TiO_2 nanotube photocatalyst for hydrogen production from water. *International Journal of Hydrogen Energy*, 36(11):6560–6568.

Xu, S., Ng, J., Zhang, X., Bai, H., and Sun, D. D. (2010). Fabrication and comparison of highly efficient Cu incorporated TiO_2 photocatalyst for hydrogen generation from water. *International Journal of Hydrogen Energy*, 35(11):5254–5261.

Xu, S. and Sun, D. D. (2009). Significant improvement of photocatalytic hydrogen generation rate over TiO_2 with deposited CuO. *International Journal of Hydrogen Energy*, 34(15):6096–6104.

Yamada, Y. and Kanemitsu, Y. (2012). Determination of electron and hole lifetimes of rutile and anatase TiO_2 single crystals. *Applied Physics Letters*, 101(13):133907.

Yamaguchi, T., Kazuma, E., Sakai, N., and Tatsuma, T. (2012). Photoelectrochemical responses from polymer-coated plasmonic copper nanoparticles on TiO_2. *Chemistry Letters*, 41(10):1340–1342.

Yamashita, H., Harada, M., Misaka, J., Takeuchi, M., Ichihashi, Y., Goto, F., Ishida, M., Sasaki, T., and Anpo, M. (2001). Application of ion beam techniques for preparation of metal ion-implanted TiO_2 thin film photocatalyst available under visible light irradiation: metal ion-implantation and ionized cluster beam method. *Journal of Synchrotron Radiation*, 8(2):569–571.

Yang, F., Sun, Q., Ma, L., Jia, Y., Luo, S., Liu, J., Geng, W., Chen, J., Li, S., and Yu, Y. (2010). Magnetic properties of Cu_mO_n clusters: A first principles study. *The Journal of Physical Chemistry A*, 114(32):8417–8422.

Yasomanee, J. and Bandara, J. (2008). Multi-electron storage of photoenergy using Cu_2O–TiO_2 thin film photocatalyst. *Solar Energy Materials and Solar Cells*, 92(3):348–352.

Yoshida, T. and Kojima, K. (2015). Toyota mirai fuel cell vehicle and progress toward a future hydrogen society. *The Electrochemical Society Interface*, 24(2):45–49.

Yu, J., Hai, Y., and Jaroniec, M. (2011). Photocatalytic hydrogen production over CuO-modified titania. *Journal of Colloid and Interface Science*, 357(1):223–228.

Yu, J. and Ran, J. (2011). Facile preparation and enhanced photocatalytic H_2-production activity of $Cu(OH)_2$ cluster modified TiO_2. *Energy and Environmental Science*, 4(4):1364–1371.

Yu, Y.-H., Chen, Y.-P., and Cheng, Z. (2015). Microwave-assisted synthesis of rod-like CuO/TiO_2 for high-efficiency photocatalytic hydrogen evolution. *International Journal of Hydrogen Energy*, 40(46):15994–16000.

Zaleska, A. (2008). Doped-TiO_2: a review. *Recent Patents on Engineering*, 2(3):157–164.

Zhang, J., Zhang, R., Wang, B., and Ling, L. (2016). Insight into the adsorption and dissociation of water over different CuO (111) surfaces: The effect of surface structures. *Applied Surface Science*, 364:758–768.

Zhang, L., Jing, D., Guo, L., and Yao, X. (2014). In situ photochemical synthesis of Zn-doped Cu_2O hollow microcubes for high efficient photocatalytic H_2 production. *ACS Sustainable Chemistry and Engineering*, 2(6):1446–1452.

Zhang, R., Li, J., Wang, B., and Ling, L. (2013). Fundamental studies about the interaction of water with perfect, oxygen-vacancy and pre-covered oxygen Cu_2O (111) surfaces: Thermochemistry, barrier, product. *Applied Surface Science*, 279:260–271.

Zhang, S., Peng, B., Yang, S., Wang, H., Yu, H., Fang, Y., and Peng, F. (2015). Non-noble metal copper nanoparticles-decorated TiO_2 nanotube arrays with plasmon-enhanced photocatalytic hydrogen evolution under visible light. *International Journal of Hydrogen Energy*, 40(1):303–310.

Zhao, Y., Wang, W., Li, Y., Zhang, Y., Yan, Z., and Huo, Z. (2014). Hierarchical branched Cu_2O nanowires with enhanced photocatalytic activity and stability for H_2 production. *Nanoscale*, 6(1):195–198.

Zhao, Z., Li, Z., and Zou, Z. (2011). Understanding the interaction of water with anatase TiO_2 (101) surface from density functional theory calculations. *Physics Letters A*, 375(32):2939–2945.

Zuo, F., Wang, L., Wu, T., Zhang, Z., Borchardt, D., and Feng, P. (2010). Self-doped Ti^{3+} enhanced photocatalyst for hydrogen production under visible light. *Journal of the American Chemical Society*, 132(34):11856–11857.

Appendix A

Ab-initio simulations of copper oxide nanowires and clusters on TiO_2 (101) anatase surface

A.1 Optimized 2L Cu_2O and CuO nanowires and clusters on TiO_2 (101) anatase surface

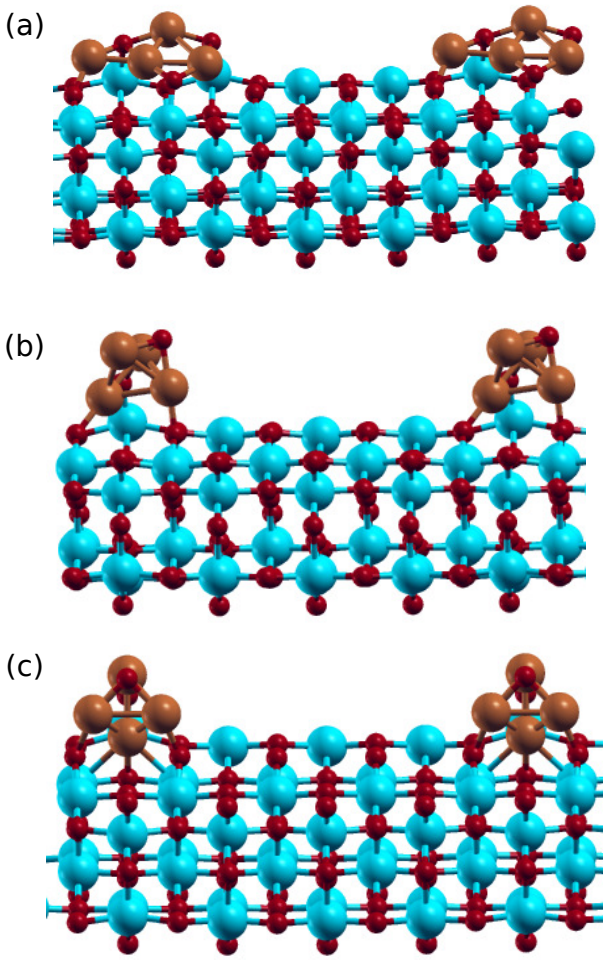

Figure A.1: 2L optimized Cu_2O clusters on TiO_2 (101) surface. The total energy differences are with respect to that of the most stable structure (a). (a) $\triangle$E=0 eV; (b) $\triangle$E=0.37 eV; (c) $\triangle$E= 0.80 eV. Blue balls; titanium, red balls; oxygen, red-brown balls; copper. The two Cu_2O clusters on TiO_2 anatase (101) surface are replicas of each other.

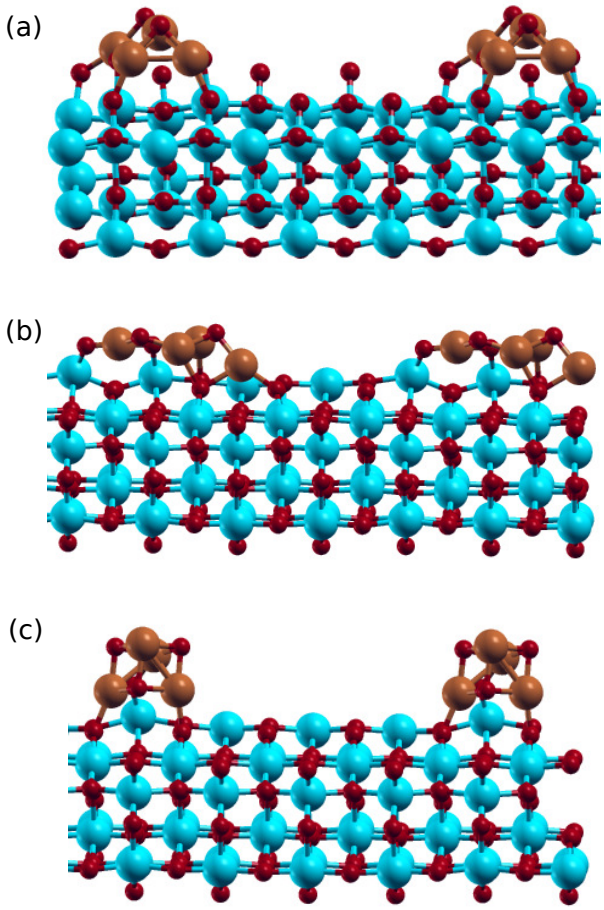

Figure A.2: 2L optimized CuO clusters on TiO_2 (101) surface with their respective total energy differences referenced to the most stable structure, (a). (a) $\triangle$E=0 eV; (b) $\triangle$E=0.94 eV; (c) $\triangle$E= 0.96 eV. Colour code as in Fig. 3. The two CuO clusters on TiO_2 anatase (101) surface are replicas of each other.

A.2 Electronic structure of 2L Cu_2O and CuO nanowires and clusters on TiO_2 (101) anatase surface

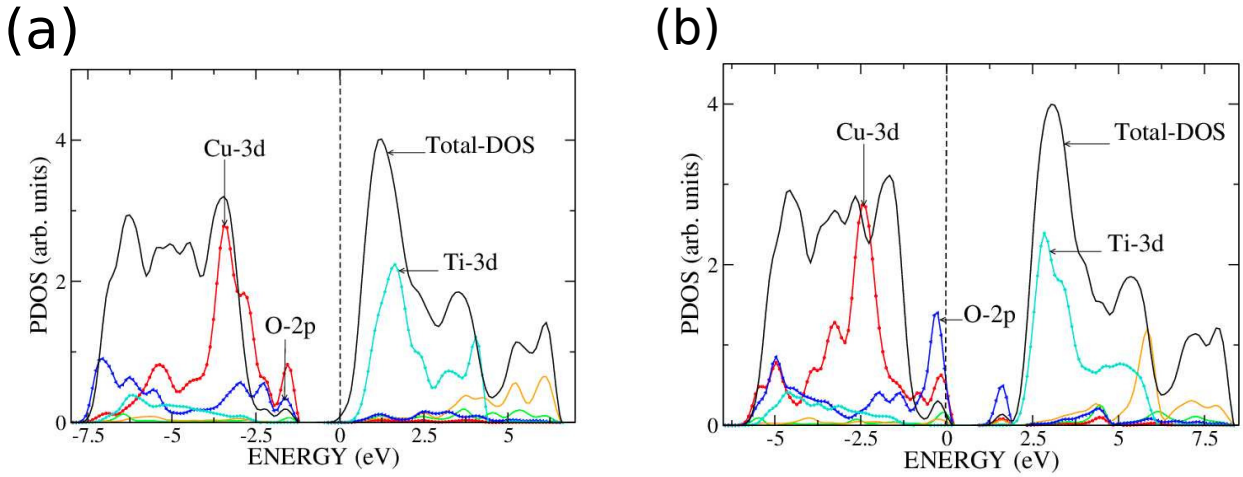

Figure A.3: TDOS and PDOS of most stable 2L Cu_2O/TiO_2 clusters; (a) Cu_2O/TiO_2 (Fig. A.1(a)) and (b) Cu_2O/TiO_2 (Fig. A.1(b))(101) anatase surface. Black solid line: total DOS; red line with circles: Cu-3d; blue line with triangles: O-2p; turquoise line with diamonds: Ti-3d. Fermi level is set at 0 eV. The Total-DOS has been scaled down to be on the same scale as the PDOS.

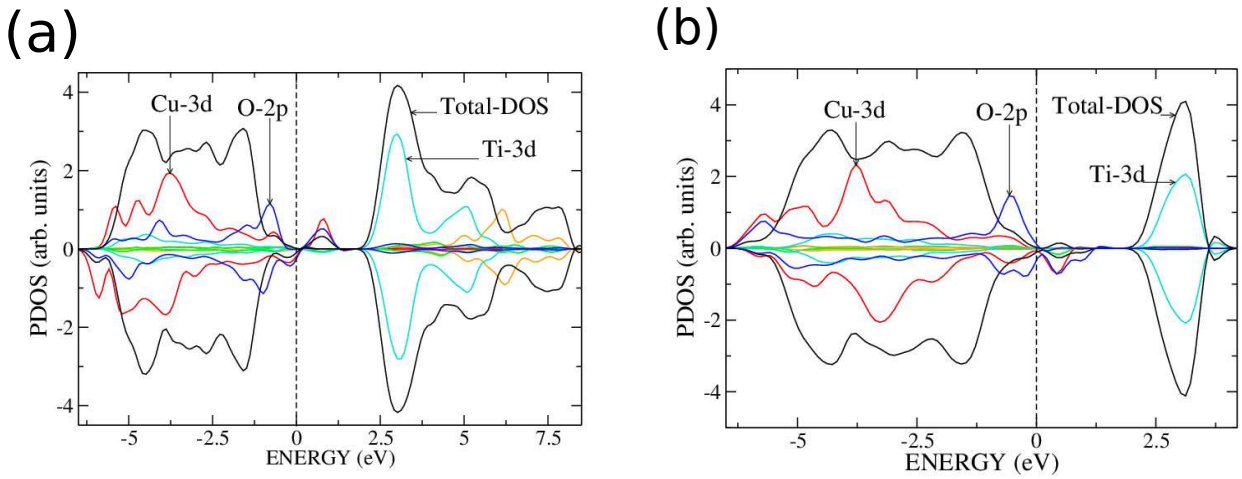

Figure A.4: TDOS and PDOS of most stable 2L CuO/TiO_2 clusters; (a) CuO/TiO_2 (Fig. A.2(a)) and (b) CuO/TiO_2 (Fig. A.2(b))(101) anatase surface. Black solid line: total DOS; red line with circles: Cu-3d; blue line with triangles: O-2p; turquoise line with diamonds: Ti-3d. Fermi level is set at 0 eV. The Total-DOS has been scaled down to be on the same scale as the PDOS.

A.3 Total Löwdin Charges (Q) and Polarization (μ)

Table A.1: Total Löwdin charge (Q) and Polarization (μ) of Cu and O atoms in bulk Cu_2O, isolated Cu_2O nanowire (NW) and Cu_2O/TiO_2 nanowire (NW) as calculated from their respective PDOS.

Atm species	Löwdin charge (|e|)			Polarization (μ_B)		
Cu/O	Cu_2O-bulk	Cu_2O-NW	Cu_2O/TiO_2-NW	Cu_2O-bulk	Cu_2O-NW	Cu_2O/TiO_2-NW
Cu	10.80	10.80	10.83	0.00	0.00	0.00
Cu	10.80	10.77	10.94	0.00	0.00	0.00
Cu	10.80	10.72	10.94	0.00	0.00	0.00
Cu	10.80	10.65	10.86	0.00	0.00	0.00
O	6.37	6.44	6.55	0.00	0.00	0.00
O	6.37	6.47	6.55	0.00	0.00	0.00

Table A.2: Total Löwdin charge (Q) and Polarization (μ) of Cu and O atoms in bulk CuO, isolated CuO nanowire (NW) and CuO/TiO_2 nanowire (NW) as calculated from their respective PDOS.

Atm species	Löwdin charge (|e|)			Polarization (μ_B)		
Cu/O	CuO-bulk	CuO-NW	CuO/TiO_2-NW	CuO-bulk	CuO-NW	CuO/TiO_2-NW
Cu	10.63	10.62	10.72	0.25	0.22	0.43
Cu	10.63	10.63	10.66	-0.25	0.20	-0.30
Cu	10.63	10.63	10.66	-0.25	0.20	0.43
Cu	10.63	10.51	10.65	0.25	0.38	0.37
O	6.36	6.48	6.38	0.00	0.36	0.39
O	6.36	6.32	6.36	0.00	0.93	0.02
O	6.36	6.33	6.55	0.00	0.91	0.25
O	6.36	6.35	6.55	0.00	0.85	0.31

A.4 TDOS and PDOS of clean TiO_2 (101) Surface

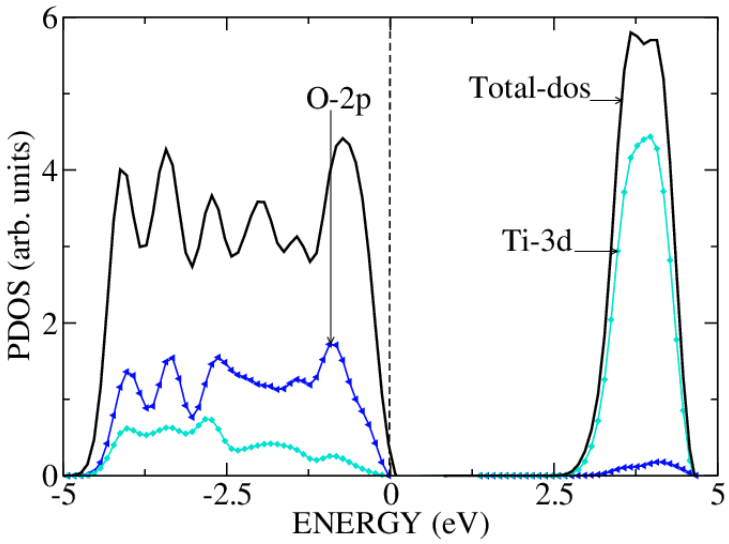

Figure A.5: TDOS and PDOS of clean TiO_2 (101) surface. Fermi level is set at 0 eV. The total DOS has been reduced by a factor of 25 to be on the same scale as the PDOS.

Appendix B

A Density Functional Theory Study of Water Photo-oxidation on Cu_2O/TiO_2 and CuO/TiO_2 anatase (101) Surfaces

B.1 Nanostructured Cu_2O/TiO_2 anatase (101) surface

B.1.1 Thermodynamic calculations of O* oxidation species ($S_2^{2(100)}$)

The Gibbs free energy of water molecule: $G_{H_2O} = E_{H_2} + ZPE - TS = -468.17eV$. The Gibbs free energy of hydrogen molecule: $G_{H_2} = E_{H_2} + ZPE - TS = -31.83eV$. The chemical potential of oxygen, μ_O is determined from equation 5.6:

$$\begin{aligned}\mu_O &= G_{H_2O} - G_{H_2} + 2eU_b, \\ &= -468.17\ eV - (-31.83\ eV) + 2eU_b, \\ &= -436.34\ eV + 2eU_b. \end{aligned} \tag{B.1}$$

The chemical potentials of the bulk TiO_2, (μ_{TiO_2}) is approximated to be equal to DFT energy per formula unit (ε_{TiO_2}): μ_{TiO_2} = -2459.30 eV. The chemical potential of titanium, μ_{Ti} is determined from equation 5.7:

$$\begin{aligned}\mu_{Ti} &= \mu_{TiO_2} - 2\mu_O, \\ &= \mu_{TiO_2} - 2G_{H_2O} + 2G_{H_2} - 4eU_b, \\ &= -2459.30\ eV + 872.68\ eV - 4eU_b, \\ &= -1586.62 - 4eU_b. \end{aligned} \tag{B.2}$$

The chemical potentials of the bulk Cu_2O, (μ_{Cu_2O} is approximated to be equal to DFT energy per formula unit: (μ_{Cu_2O})= -1867.61 eV. The chemical of potential of Cu, $\mu_{Cu}^{Cu_2O}$ is evaluated using equation 5.9:

$$\begin{aligned}\mu_{Cu}^{Cu_2O} &= \mu_{Cu_2O} - \frac{1}{2}(G_{H_2O} - G_{H_2} + 2eU_b), \\ &= -1867.61\ eV + 218.17\ eV - eU_b, \\ &= -1649.44\ eV. \end{aligned} \tag{B.3}$$

The surface free energy for Cu_2O/TiO_2 (see equation 5.13):

$$\begin{aligned}\gamma_{S_k^{m(\alpha\beta\gamma)}} =& \frac{1}{A}\{G - [n_{Ti}(\varepsilon_{TiO_2} - 2G_{H_2O} + 2G_{H_2}) \\ &+ n_{Cu}(\varepsilon_{Cu_2O} - \frac{1}{2}G_{H_2O} + \frac{1}{2}G_{H_2}) \\ &+ n_O(G_{H_2O} - G_{H_2}) + n_H\frac{1}{2}G_{H_2} \\ &+ (2n_O - 4n_{Ti} - n_H - n_{Cu})eU_b]\}.\end{aligned}$$

When calculated values from equations (B.1, B.2 and B.3) and Gibbs free energy of O* oxidation species on Cu_2O/TiO_2 ($S_2^{2(100)}$): G=$E_{DFT(total)}$ + (ZPE - TS)= -66,929.15 eV, are substituted into equation 5.13, it becomes:

$$\begin{aligned}\gamma_{S_2^{2(100)}} =& \frac{1}{A}\{G - [24(-1586.62\ eV) + 4(-1649.44\ eV) + 51(-436.34\ eV) \\ &+ (102 - 96 - 4)eU_b]\}, \\ =& \frac{1}{A}\{G - [-66,929.98\ eV + 2eU_b]\}, \\ =& \frac{1}{77.74}\{-66.929.15\ eV - [-66,929.98\ eV + 2eU_b]\}, \\ =& \frac{1}{77.74}\{0.83\ eV - 2eU_b]\}. \end{aligned} \tag{B.4}$$

The linear equation B.4 is used to plot the line labelled $S_2^{2(100)}$ in Fig. 5.16a. This computation is repeated for intermediate species (O*, HO* and HOO*) terminated on pristine TiO_2, Cu_2O/TiO_2 and CuO/TiO_2 to generate linear equations that are used to plot Figures 5.15 to 5.17. The variation of chemical potential on different atomic types and references are taken into consideration.

Appendix C

PUBLICATIONS, CONFERENCES, PRESENTATIONS AND SCHOOLS ATTENDED

C.1 Conference presentations

1. Victor Meng'wa, Nicholas Makau, George Amolo, Sandro Scandolo and Nicola Seriani, poster titled: Structural, Thermodynamic and Electronic properties of Cu_2O and CuO nanowires and clusters on TiO_2 (101) anatase surface. Poster presented during the Workshop on Spectroscopy and Dynamics of Photoinduced Electronic Excitations, ICTP, Trieste, ITALY, 8^{th} -12^{th} May, 2017

C.2 Schools and Conferences Attended

1. College on Multiscale Modeling of Materials for Energy Applications, ICTP,Trieste, ITALY, 4^{th}-15^{th} July, 2016.

2. Workshop on Spectroscopy and Dynamics of Photoinduced Electronic Excitations, ICTP, Trieste, ITALY, 8^{th} -12^{th} May, 2017.

3. School on Electron-Phonon Physics from First Principles, ICTP, Trieste, ITALY, 19^{th}-23^{rd} March, 2018.

C.3 Publications

1. V. K. Meng'wa, N. W. Makau and G. O. Amolo. Photoactive interaction of catechol adsorbed on TiO_2 rutile (110) surface for dye sensitized solar cells (DSSCs) applications: Kenya J. Sci. Tech. Inn. Vol. 4 and 5 2016, 74-84

2. Meng'wa, V., Amolo, G., Makau, N., Lutta, S., Okoth, M., Mwabora, J., ... and Gateru, R. Electronic Properties of Catechol Adsorbed on Rutile TiO_2 and SnO_2 (110) Surfaces: A Density Functional Theory Study. The African Review of Physics (2016) 11:0021

3. Meng'wa, V., Makau, N., Amolo, G., Scandolo, S., and Seriani, N. (2017). Ab Initio

Simulations of Copper Oxide Nanowires and Clusters on TiO_2 (101) Anatase Surface. The Journal of Physical Chemistry C, 121(37), 20359-20365, DOI: 10.1021/acs.jpcc.7b06681.

4. Meng'wa, V., Makau, N., Amolo, G., Scandolo, S., and Seriani, N. (2018). A Density Functional Theory Study of Water Photo-Oxidation at Copper Oxide Nanostructures on the Anatase (101) Surface. The Journal of Physical Chemistry C, 122 (29), 16765-16771, DOI: 10.1021/acs.jpcc.8b03671.